MICROSTRUCTURE AND MECHANICAL PROPERTIES OF WELDS IN PIPELINE STEEL

A Thesis Submitted to the College of

Graduate Studies and Research

In Partial Fulfillment of the Requirements

For the Degree of Master of Science

In the Department of Mechanical Engineering

University of Saskatchewan

Saskatoon

By

Omale Idokoh Joseph

PERMISSION TO USE

In presenting this thesis in partial fulfillment of the requirements for a Postgraduate degree from the University of Saskatchewan, I agree that the Libraries of this University may make it freely available for inspection. I further agree that permission for copying of this thesis in any manner, in whole or in part, for scholarly purposes may be granted by Prof. Jerzy Szpunar, the professor who supervised my thesis work or in his absence, by the Head of the Department or the Dean of the College in which my thesis work was done. It is understood that any copying or publication or use of this thesis or parts thereof for financial gain shall not be allowed without my written permission. It is also understood that due recognition shall be given to me and to the University of Saskatchewan in any scholarly use which may be made of any material in my thesis.

Requests for permission to copy or to make other uses of materials in this thesis in whole or part should be addressed to:

Head of the Department of Mechanical Engineering

University of Saskatchewan

57 Campus Drive

Saskatoon, Saskatchewan S7N

ABSTRACT

Transport of oil and gas in various service environments, presents an enormous challenge. Pipelines are used for transportation of those natural resources. The failure of the pipeline is always associated with serious environmental damage and heavy losses. Very often the failure starts at welds that are used to join different elements of pipeline steels. Microstructural parameters like composition, structure, morphology of non-metallic inclusions and residual stresses due to welding play an important role in initiating the cracking of pipeline welds.

The main objectives of this research thesis are to analyze the microstructure and mechanical properties of submerge arc weld and establish the role of microstructure in initiation and propagation of cracks in sour (HIC) environment.

In this work, the optical microscope, Electron backscattered diffraction (EBSD), X-ray diffraction and Transmission electron microscope (TEM) were used to investigate the microstructure of the X70 pipeline steel base metal, the weld bead and heat affected zone. The result obtained showed that the base metal have equiax ferrite grains while the weld bead have structure of acicular ferrite and fine bainite grains with many Al-Si-Mn-Ti oxide particles/inclusions. The heat affected zone microstructure has coarse grains with martensite and NbTi(CN) precipitate/particles. Analysis of the cross section of the weld shows that higher kernel values were observed in the weld cross section compared to the weld top surface. The kernel average misorientation (KAM) analysis at the cross section of the weld show that the amount of residual strain is higher than on the surface of the weld. The residual stress on the weld top surface was purely compressive while at the cross section mixture of tensile and compressive stress were observed. The hardness was the highest in the weld bead, a bit lower in the base metal and lowest in the heat affected zone. Higher density

of voids was observed at the top of the weld bead than in the middle. It was demonstrated that the difference in hardness can be directly correlated with the differences in the grain size.

HIC cracks were induced in the pipeline weld area using standard HIC test and electrochemical hydrogen-charging. The SEM observations clearly indicate that the cracking in the weld nucleated at inclusions. The cracks were seen to propagate by coalescence of small pits related to hydrogen charging. Energy dispersive (EDS) analyses showed that the cracks nucleation sites are most often located at Al-Si-Mn-Ti oxide. The EBSD measurements show that HIC can take place at a wide range of grain orientations. The map of the location of HIC crack shows that they can be both transgranular and intergranular.

Experiments were carried out to understand the effect of hydrogen and role of microstructure on HIC susceptibility in the steel weld under tensile load. The results show that the ductility of the steel weld became lower as charging time increased. EBSD investigation were carried out in the heat affected zone area since all the fractured specimens were fractured in this area. The results shows that large grains and dislocation density in heat affected zone is related to the high susceptibility of the steel weld to fail under tensile load.

ACKNOWLEDGMENT

I would like to express my sincere gratitude to my supervisor, Prof. Jerzy Szpunar for his fatherly guidance during my M.Sc. programme. I am immensely grateful for your kindness, patience, time and professional contributions to the success of my study. Thanks for always pushing me for more. I want to appreciate the contributions of Prof. Chris Zhang and Prof. Ike Oguocha, my advisory committee members. I am grateful for your insightful and valuable comments during my committee meeting and other times.

My appreciations also go to Prof. Akindele Odeshi for his consistent spiritual direction during my study. To Curt McDougall and Carol Scott, your constant support and accommodation are deeply valued.

Dr. Salman Razavi is greatly appreciated. Your contribution to this research is deeply appreciated. Your gentle yet professional guidance made it possible for this project to come to a successful end. To Dr. Ritwik Basu, Dr. Ming song, Dr. Dr. Mohammad Mohtadi-Bonab, Ryan Ouellette, Mostafijur Rahman, Linu malakkal and all of members of the advance material and renewable energy research group at the University of Saskatchewan thank you.

All of the parents who has supported me throughout my study, late Emeritus Prof. and Chief (Mrs.) Adeajayi, Squadron Ld. (Rtd) and Mrs. Badiru, Prof. and Dr. (Mrs.) Adegoke, Dr. and Dr. (Mrs.) Ogbole.

My gratitude also goes to late Rev. J. O Ejembi, the best father anyone could ask for and my late mother Maria Okpe. Thank you for laying the right foundation in my early childhood. I will always live to make you proud.

DEDICATION

To the Almighty, eternal father, the giver of life, the One who was, who is and is to come. The one through whom my life received a fresh start. The restorer of Hope, “Pantokrator”, YHWH, all sufficient God, I AM THAT I AM.

TABLE OF CONTENTS **Page**

LIST OF TABLES **Page**

LIST OF FIGURES **Page**

LIST OF ABBREVIATIONS

ABBREVIATIONS

HIC	Hydrogen induced cracking
XRD	X-Ray diffraction
EBSD	Electron backscattered diffraction
TEM	Transmission electron microscope
EDS	Energy dispersive spectroscopy
SEM	Scanning electron microscopy
HSS	High strength steel
HSLA	High-strength low alloy
API	American petroleum institute
SAW	Submerge arc welding
SMAW	Shielded metal arc welding
WM	Weld metal
BM	Base metal
HAZ	Heat affected zone
CGHAZ	Coarse grain heat affected zone
FGHAZ	Fine grain heat affected zone
AF	Acicular ferrite
KAM	Kernel average misorientation
IPF	Inverse pole figure
LAGB	Low-angle grain boundary
HAGB	High-angle grain boundary

CHAPTER ONE

INTRODUCTION

1.1 Overview

There is an ever increasing demand to transport oil and gas products in a safe and secured mode. Pipeline system are one of the most economic forms of transportation when developing hydrocarbon fields in the sea within the offshore zones [1]. According to the global industry analyst (GIA) report, Global market for spiral welded pipes and tubes is projected to reach 24.6 million tons by 2018, driven by level of activity in the energy sector, and intensifying pipeline construction activity [2].

Manufacturing of high strength line-pipe steels to transport different natural resources in a variety of service environments presents an enormous challenge. Weld failure has often contributed failure of line pipes. The quality of the weld plays an important role in prevention of weld cracking during service use. About 60% of oil pipeline failures and 51% of natural gas pipeline failures are the result of corrosion or weld failures and hence, weld defects are considered the main stress raisers in a pipeline [3].

Two factors that were identified to be a major contributor to pipeline failure are weld failure in response to mechanical stress and corrosion of pipeline steel according to the report on pipeline performance in Alberta, 1990–2012 in 2013 [4]. The role of corrosion or sour service environment in pipeline failure have been well studied. However, it is difficult to clearly understand the mechanism by which this failure occurs especially with the complex nature of welding [4]. For all type of linepipes such as spiral welded or straight seam welded pipe, the welding plays an important role in joining of pipeline steels for a long distant transport of crude oil and gas for

refining or distribution purposes. Welding is a complex process involving control of the liquid-solid transformation and structural changes of steel structure, nevertheless its application in joining has gained wide acceptance as it produces a continuous strong joints.

The successful application of welding in joining of pipeline steels makes it possible to produce long line pipes for oil and gas transport both offshore and onshore. However, the welding is not devoid of challenges related to the high temperature involved in the welding process. Linepipe fracture often related to weld failure can lead to environmental catastrophe and significant economic losses. Considering the fact that line pipes are designed to serve in rigorous environments for several decades, failure risk must be mitigated. Susceptibility of steels to hydrogen induced cracking (HIC), sulphide stress cracking (SSC), and stress corrosion cracking (SCC) has been reported to be responsible for the majority of catastrophic linepipe failures [5, 6]. It has been reported that the mechanisms for these cracking phenomena in steels and welds depend on microstructural parameters like composition, structure and morphology of non-metallic inclusions as well as mechanical and environmental parameters, such as applied stress, type of liquid or gas being transported, groundwater chemistry, among many others [7-9]**.** Several research projects have been conducted to improve the quality of welds by alloying of filler metals and varying the welding parameters in order to produce a microstructure that is more resistant to cracking as well as allow to reduce the amount of residual stresses. It is vital to know how the structure of steel welds can be improved and to understand the role that microstructure plays in failure mechanism in linepipe welds.

1.2 Motivation

In the last few years, the oil and gas industry has experience major challenges related transportation of crude oil from production rigs to the. The use of linepipe is a rather safe and cheap method of oil and gas transport. Line pipe failure is however associated with huge economic loss, It is therefore necessary that line pipes have a combination of toughness and strength required to function in variety of service environment. Although line pipe weld cracks have been investigated in the past, there is a need to generate microstructural and mechanical data in order to help understand the effect of service environment in linepipe weld failure. In this work, effort will be made to understand changes that occur in the microstructure of X70 steels after welding and also how the microstructure of the welded area affect the mechanical properties. A study of the role of sour environment will be conducted and will primarily be focused on effects of hydrogen charging on microstructure and mechanical properties.

1.3 Research objectives

The role of a submerge arc welding process on microstructure of an X70 steel and it mechanical properties will be investigated. The microstructure developed during the welding process will be investigated and analyzed in relation to failure of the pipe under mechanical load and different service environment. The specific objectives include the following:

1. To relate the mechanism of pipeline weld failure to its microstructure.
2. To determine microstructural factors that contribute to the weld failure in corrosive and hydrogen environments.
3. To recommend a microstructure that is more resistant to HIC cracking.

1.4 Methodology

The pipeline steels used in this study is an X70 which is widely used to carry oil and natural gas over long distances. All of the welded samples are received as plates and pipes. In order to achieve the above mentioned objectives, specimens were machined from the as received pipes for characterization. Some of the samples were hydrided using the electrolytic or cathodic charging method. Mechanical test such as micro hardness test, tensile test were conducted on the as received specimen and hydrogen charged specimen. X-Ray diffraction equipment was employed to evaluate the residual stress on the as received welded specimen. Microstructural characterization was done using the optical and scanning microscopes. The microstructure, local misorientation and crystallographic orientation data was acquired using the Electron backscattered diffraction (EBSD) and Transmission electron microscope (TEM) technique. Elemental analysis of the weld and inclusions was carried out using the energy dispersive x-ray spectroscopy (EDS) technique.

1.5 Thesis arrangement

The thesis is divided into five chapters. Chapter 1 presents an overview of the study, the challenges, motivation and main objectives of this research. A comprehensive literature review of previous research pertinent to this study is presented in Chapter two. The detailed information about the materials and experimental methods used in the study are presented in chapter three. Chapter 4 presents the result and discussion. A summary of the conclusions drawn from this work and suggestions for future work are outlined in Chapter 5.

CHAPTER TWO

LITERATURE REVIEW

2.1 Composition of X70 pipeline steel

The American Petroleum Institute (API) 5L X70 is in the class of high strength steels (HSS) developed to tackle the demand for sufficient toughness and ductility required to operate in harsh environment in offshore application. It possess refined grain and high cleanliness. It is characterized by the low sulphur content and reduced amount of detrimental second phases such as oxides, inclusions and pearlite.

The typical chemical composition of HSS steels may vary for different thickness o meet particular mechanical property requirement. Usually, they have a manganese (Mn) content up to 2.0 wt% in combination with very low carbon content (< 0.10 wt% C). Minor additions of alloying elements such as vanadium (V), molybdenum (Mo), titanium (Ti), niobium (Nb), and boron (B). Each of this alloying elements helps in the strengthening of ferrite through grain refinement, solid solution and precipitation hardening mechanism. For example carbon provide strengthening to the metal matrix by precipitation while manganese and molybdenum (Mo) delays the austenite decomposition during accelerated cooling, provide strengthening effect and Improves hardenability respectively [10-11]. Both elements also play a major role in obtaining a fine grained lower bainite microstructure. On the other hand, vanadium (V) Leads to precipitation

strengthening during the tempering treatment and act as a strong ferrite strengthener. Titanium (Ti) and niobium (Nb) improves strength through grain refinement by suppressing the coarsening of austenite grains (TiN formation) and niobium (Nb) retards recrystallization.

2.2 Submerge arc welding (SAW)

The submerged arc welding (SAW) technique is a fusion welding process in which the molten steel is produced by an electric arc submerged under a granular flux bed. During welding, granular flux is melted using heat generated by arc and forms cover of molten flux layer which in turn avoids spatter tendency and prevents accessibility of atmospheric gases to the arc zone and the weld pool. A schematic diagram of a single-pass wire SAW setup is shown in (Fig. 2.1)

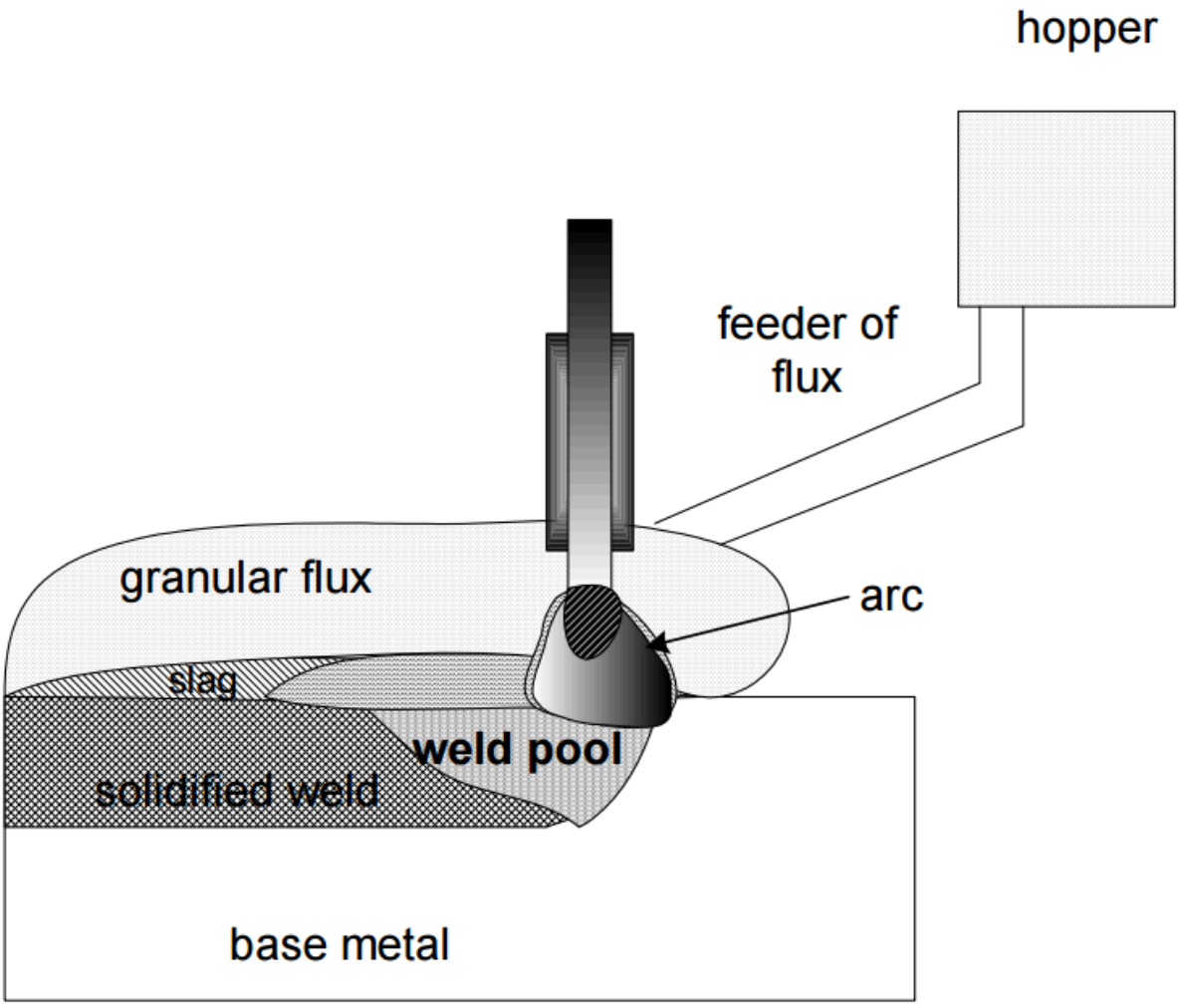

Fig. 2.1. Schematic of submerge arc welding system (adapted from [12]).

The flux is fed by gravity from a hopper above, in the path of the moving electrode. Due to high welding currents (300 A to 1600 A) and high travel speeds which result in increased heat input and deposition rate [13], this technique has been widely used in joining structural members in ships, manufacture of pressure vessels, bridge beams, massive water pipes, thin sheet shells e.t.c. During welding, molten flux reacts with the impurities in the molten weld metal to form slag which floats over the surface of the weld metal. The layer of slag over the molten weld metal is capable of preventing atmospheric gas contamination and so improves properties of the weld joint. It influences the cooling rate of weld metal (WM) and heat affected zone (HAZ) due to shielding of

the weld pool by molten flux and solidified slag leading to a smoother weld bead and reduced the cracking tendency of hardenable steel. The slag and flux cover over the weld in the SAW process provides a higher thermal efficiency (ratio of energy output to the energy input) compared to other welding process such as plasma arc welding (PAW), gas tungsten arc welding (GTAW) and gas metal arc welding (GMAW) found to be 47%, 67% and 85% respectively [14]. During welding, contamination of the weld is possible due to atmospheric interaction. Hence, SAW is generally performed indoors in fabrication shops because it always carries the risk of undesirable level of moisture finding its way into the joint or flux and resulting in porosity in the weld. For example, elements such as nitrogen and hydrogen are capable of entering the weld pool from the atmosphere and moisture in the flux. Nitrogen causes large precipitate of nitrides on cooling while trapped hydrogen within metal matrix is capable of causing embrittlement of the metal and heat affected zone cracking [15]. Therefore, It is necessary that the SAW process be carried out in a closed atmosphere to minimize damaging effect of contaminant from the atmosphere. Fluxes influence the weld metal composition appreciably in the form of addition or loss of alloying elements through gas metal and slag metal reactions. It covers the molten metal and prevents weld spatter, electric sparks and conduct current from the electrode to the work piece [16]. Flux composition is an important aspect since the flux plays a very crucial role in achieving quality weld. Therefore flux compositions are optimised to ensure that necessary alloying elements are present in the filler wire and the flux. Generally, the composition of the flux include halides and oxides such as MnO, SiO_2, CaO, MgO, Al_2O_3, TiO_2, FeO, and CaF_2 and sodium/potassium silicate [17]. Based on this composition, the flux is said to be either basic (donors of oxygen) or acidic (acceptors of oxygen). Depending upon relative amount of these acidic and basic fluxes, the basicity index of flux is decided. The basicity index of flux is ratio of sum of the (wt. %) of all basic oxides to all non-basic

oxides [18]. Different authors have investigated the influence of flux basicity index on weld composition, microstructure and mechanical properties [19-21]. Conclusion shared these authors is that increasing the basicity index (BI) reduces weld metal oxygen content and produces clean weld metals with regard to oxide inclusions.

2.3 Effect of submerged arc welding on steels

When metals are joined together by welding, the base metal is heated above it melting temperature, depending on the geometry of the joints, the base metal cools down rapidly under the conditions of restraints. The original microstructure of the region close to the weld region is altered due to the severe thermal cycle from the welding heat. This change in microstructure also alters the mechanical properties of the metal. The microstructures that develop in welded joints are influenced by factors such as base metal chemistry, filler wire, flux and cooling rate. In general three different distinct metallurgical zone in a welded joint has been identified [22-23]. They are the unaffected base metal (BM), the heat affected zone (HAZ) and the weld metal (WM) or fusion zone (FZ). The typical microstructure of an API X70 pipeline steel contain a mixture of different product such as acicular ferrite (AF), widmanstatten ferrite (WF), bainite (B), grain boundary ferrite (GBF), ferrite with martensite/austenite (M-A)micro constituent.[24-25].

2.3.1 The heat affected zone

The heat affected zone (HAZ) experiences peak temperature below the solidus temperature while high enough that can change the microstructure and mechanical property of the area compare to

that of the base metal. It is the area between the base metal and the weld metal. The microstructure at the heat affected zone varied as you move from the fusion zone to the base metal. This is attributed to the different temperature experienced by the material. The region closest to the molten weld zone experiences the highest temperature as a result the microstructure in this region is coarser than other areas. The degree of change in microstructure in HAZ is a function of the amount of heat input, peak temperature reached, time at the elevated temperature, and the rate of cooling. Usually, this zone remains the weakest section in a weldment. Conventional zones of the HAZ are illustrated by Fig. 2.2

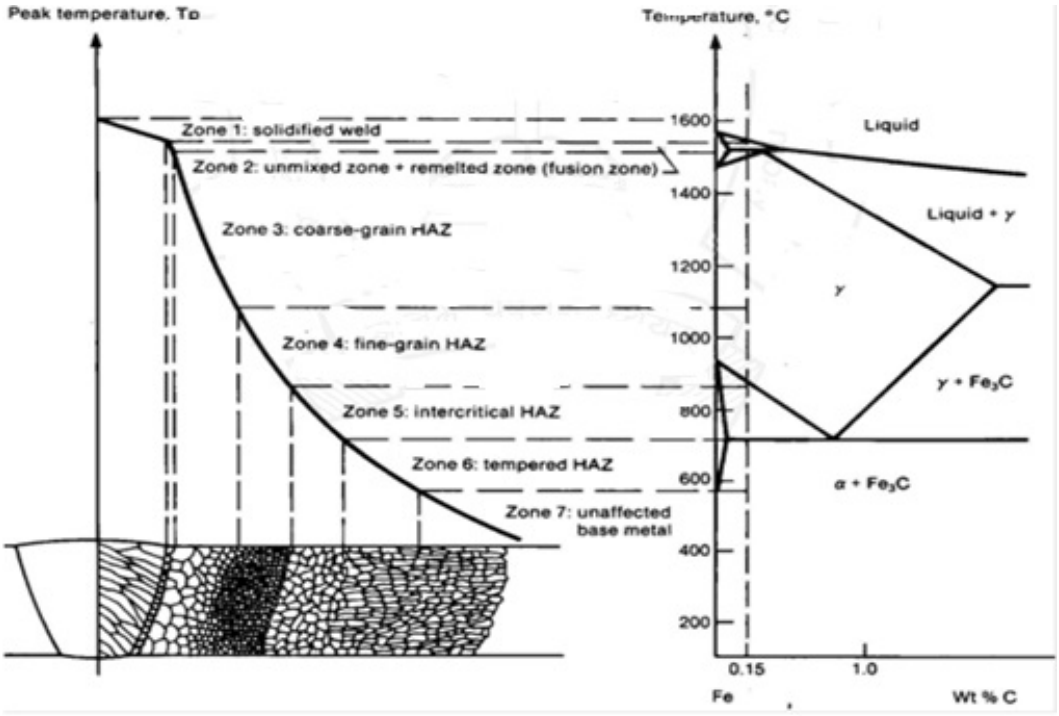

Figure 2.2. Schematic diagram of the heat-affected zone of a 0.15 wt. % C steel indicated on the Fe-Fe_3C phase diagram [adapted from [25]].

As illustrated in Fig. 2.2, the HAZ is divided into four regions, namely: coarse grained (CGHAZ), fine grained (FGHAZ) inter-critical (ICHAZ) and tempered zones. It is expected that the peak temperature experienced by the base metal decreases with increasing distance away from the fusion zone and as a result the grain growth decreases with increasing distance away from the fusion line [26].

It is well known that the grain size in the heat affected zone is usually coarse. The high heat input produce low cooling rate, and produces coarser grains because of the increased length of time spent at this high temperature. The fine grained heat affected zone (FGHAZ) consists of fine ferrite grains. This is because this region only experience high temperatures enough to form austenite during the welding process. However, the peak temperature attained is not high enough to completely dissolve the precipitates (carbides and nitrides) in the (FGHAZ) as in the CGHAZ. As a result, fine ferrite grains are formed and austenite grain growth is also suppressed. The grains in the inter-critical HAZ (ICHAZ), does not transform completely to austenite on heating and as a result the grains are refined whereas the austenite may transform to pearlite, martensite or be retained as martensite-austenite (M-A) microconstituent. Following the inter-critical HAZ (ICHAZ) is the tempered HAZ and base metal. The grain size is not affected because no transformation of austenite occurs. Thus, the austenite grain size within the HAZ is regulated by the high temperature and the weld thermal cycles that were encountered [26-27]. The mechanical properties of the HAZ is also affected due to the change in the grain size in this region. For

example, it was observed that the hardness of a welded joint in X65 pipe line steel varied as one move across the coarse grained (CGHAZ), fine grained (FGHAZ) inter-critical (ICHAZ) and tempered zones [28].

2.3.2 The weld metal

The weld metal is characterized by mixture of completely molten base metal and filler metal from consumable electrodes used during the welding process. This zone on cooling fills the gap between the base metal plates and bonds them. It is a mixture of the filler wire, flux and base metal that has melted during the welding process. The evolution of this microstructure in the weld metal is described to be an epitaxial solidification when the grains at the base metal act as the substrate for nucleation of crystals during solidification of the fusion zone. Thus, new crystals or grains are formed by arranging the atoms from the base metal grains without altering their crystallographic orientations [24]. Non-epitaxial solidification occurs when fusion welding is done with a filler material or with two different metals and the new grains start forming on heterogeneous sites at the fusion boundary. The microstructure at the weld is greatly affected by the welding parameters such as welding voltage, speed, current and the presence of oxide inclusions.[23, 29- 30].

2.4 Influence of welding parameters on microstructure

In order to understand the developing microstructure in a weld metal it is important to consider the welding parameters applied. It has been well researched that the microstructure that develops in

the weld joint is influenced by the chemical composition of the base metal, the filler wire, the flux and the actual cooling rate experienced by the weldment during transformation of austenite to ferrite [31-33]. These factors includes the heat input (H), alloy chemistry and weld pool geometry all of which affect the actual cooling rate (CR) experienced by the weld joint and, consequently, its microstructure and mechanical properties.

2.4.1 Effect of heat input

Heat input is a relative measure of the energy transferred per unit length of weld. It is an important characteristic because, like preheat and interpass temperature, it influences the cooling rate, which may affect the mechanical properties and metallurgical structure of the weld and the HAZ [34].

It is calculated from equation (2.1)

$$H = \frac{60EI}{1000S} \qquad 2.1$$

H = heat input (kJ/inch or kJ/mm), E = arc voltage in (Volts), I = current (Amps) and

S = travel speed (inch/min or mm/min)

The effect of heat input on microstructure have been extensively investigated by researchers. For example, Subodh Kumar et al. [35] studied the influence of heat input on the microstructure and mechanical properties of gas tungsten arc welded 304 stainless steel (SS) joints. Three heat input combinations designated as low heat (2.563 kJ/ mm), medium heat (2.784 kJ/mm) and high heat (3.017 kJ/mm) were selected from the operating window of the gas tungsten arc welding process

(GTAW). The results of the investigation indicate that significant grain coarsening was observed in the heat affected zone (HAZ) of all the joints and it was found that the extent of grain coarsening in the heat affected zone increased with increase in the heat input. The average dendrite length and inter-dendritic spacing in the weld zone was found to increase with increase in the heat.

Weld penetration is also affected by heat input. Agilam et al. [36] studied the effect of electron beam welding heat input on the microstructure and mechanical properties of Inconel 718. They concluded that for five different heat inputs the geometry of the weld (width to depth ratio) was changed. This change in heat input also altered the microstructure of the fusion zone (FZ) and the heat affected zone. It is therefore expected that increase in heat input is accompanied by an increase in the width of penetration and that of HAZ [37].

Welding is a dynamic process in which the heat source is in a state of constant motion, leading to temperature gradient variations across different area of the material, this temperature gradient also play great role in the developing microstructure. Another effect of heat input on weld microstructure is the microstructural product from the weld process. Sadeghian et al. [38] investigated effect of heat input on microstructure and mechanical properties of dissimilar joints between super duplex stainless steel and high strength low alloy steel, the result showed that an increase in heat input led to a decrease in ferrite percentage, and that detrimental phases were not present. They also observed that bainite and ferrite phases were created in heat affected zone of HSLA base metal in low heat input,; but in high heat input, perlite and ferrite phases were created.

Don et al. [39] showed that increasing the welding heat input could suppress the formation of martensite which is commonly observed at low welding heat input.

Extensive investigations have been conducted on the influence of welding heat input on the microstructure and mechanical properties of HSLA steel joints. Nath et al. [40] investigated the relationship between the heat input and the austenite grain size, and observed that the prior austenite grain size was controlled by the peak temperature (Tp) in the welding thermal cycle which was related to the welding heat input. The impact of heat input on hardness and toughness was studied by Wan et al [41]. The results of the mechanical investigation indicated that the joints made by using low heat input exhibit higher hardness and impact toughness value than those welded with medium and high heat input. It can be concluded that higher heat input can cause the expansion towards the microstructure's grain size, but will lead to lower hardness and affect the toughness value. Apurv et al. [42] also showed that tensile strength decreases with increase in heat input. The micro hardness data values was observed to increases with increase in heat input in weld pool and decreases in HAZ zone

2.4.2 Effect of cooling rate (CR)

The cooling rate of weldments depends on the heat input by the welding arc. Heat input is controlled by three variables, namely: current, voltage and travel speed. It is generally believed that travel speed affects heat input and heat input affects the cooling rate. With higher heat input,

the cooling rate is faster and vice versa. During welding, a large amount of heat is applied. Solidification of the weld pool takes place followed by cooling to room temperature. The heat applied is transferred during and after welding by conduction from the molten pool to the base metal and creates the heat affected zone (HAZ) [43-46]. The cooling rate is a primary factor that determines the final metallurgical structure of the weld and HAZ. There are many models developed for understanding the concept of cooling rate in a welded joint. Among these models are the Carslaw and Jaeger's, thick plate and Adams 2D correlation model [47-48]. Dutta and Narendranath [49] did a study on rate of cooling based on the "thick plate model" and "Adams 2D correlation". The results showed a significant cooling rate near the HAZ. It was found that the major influential property in connection with cooling rate, is heat loss. It is well established that microstructure and micro-hardness depend on the cooling rate. Increasing cooling rate generally will lower the austenite to ferrite transformation start temperatures [50]. The effect of cooling rate on residual ferrite content and composition was evaluated by Vitek et al. [51]. They showed that as the cooling rate increased, the amount of retained ferrite increased, the ferrite's chromium content decreased, and its nickel content increased. The effect of cooling rate on the evolution microstructural product such as allotriomorphic ferrite and pearlite was studied by Madariaga et al. [52]. They concluded that lower cooling rates cause the development of other phases such as allotriomorphic ferrite or pearlite but a high volume fraction of acicular ferrite can be achieved using two stage continuous cooling cycles. The role of cooling rate in a welding process is critical

in obtaining improved toughness, ductility and minimal residual stresses in the weld. It is also necessary to understand the stability of ferrite under multiple-pass welding conditions or during elevated-temperature applications by utilising cooling rate information.

2.5 Role of alloying element on weld microstructure

The mechanical properties of submerge arc weld metals are strongly dependent on the microstructure developed during solidification and cooling of the weld pool, and also depend on the weld chemical composition and cooling rate. The chemical composition is determined by base metal and electrode wire composition, dilution, and any chemical reactions in the weld arc from the flux. Two major approaches have been pursued to improve the toughness of the WM. One is to use different types of fluxes [53-54]; the other is to alter WM composition either through the use of newer filler metals [55] or by metal power additions in the WM [56-58]. Most alloying elements such as carbon, manganese and silicon increase hardenability through solid solutions strengthening, precipitation and substitutional strengthening effect by dissolving either interstitially or substitutionally in the weld metals. Small atoms such as carbon and nitrogen occupy the interstitial sites while large atoms such as silicon and magnesium dissolve substitutionally. The contribution to strengthening for each element varies. Figure below illustrate the strengthening effect of some alloying elements. As shown, increase in strength of ferrite iron by interstitial carbon or nitrogen is much greater than any substitutional alloying element.

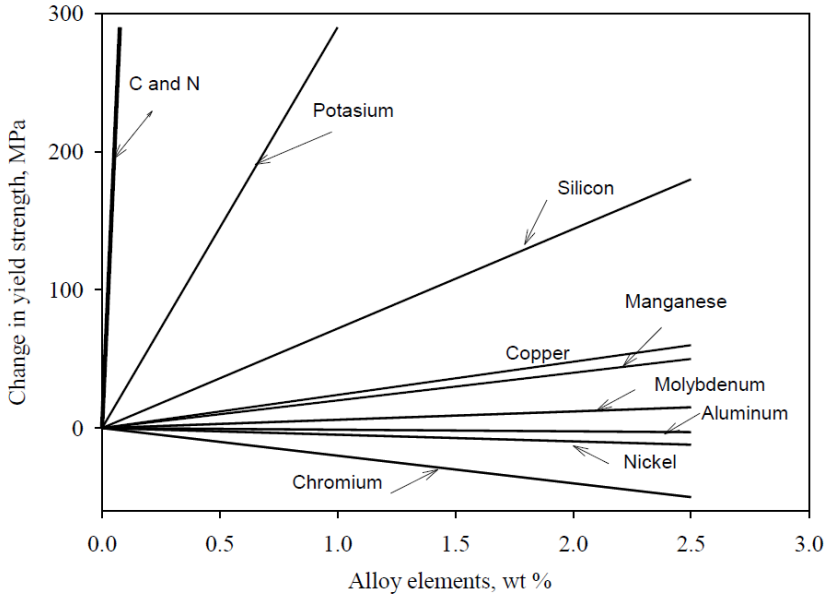

Figure 2.3. Effect of alloy addition on solid solution strengthening of ferrite [59].

The effect of these alloying elements on the development of the microstructure is discussed in the following sections.

2.5.1 Nitrogen

Nitrogen addition to weld metal as an alloying element has been a subject of discussion by many researchers. This is because unlike many elements, it is not a deliberate alloying element as it occurs universally in steels and can be picked up from the interaction between base metal, flux and the atmosphere during welding process. Most of the effect of nitrogen as seen to be detrimental, often associated with embrittlement [60]. Excess nitrogen causes porosity, and as a result, many investigators has suggested that it concentration be kept low typically less than 200 ppm [61]. The possibility of using nitrogen as an alloying element has been investigated in the past as well, for example, Evans [62] observed that nitrogen interacted with titanium and boron and, by a combination of solute and microstructural changes, affected mechanical properties in either a positive or a negative manner. However, he observed that the toughness of previously optimized composition (400 ppm Ti, 40 ppm B) was particularly degraded by nitrogen. Many authors

concluded that nitrogen be considered as a deliberate alloying element as it is seems to be beneficial under some circumstance. In most cases, the beneficial effects of nitrogen are the result of it interaction with alloying elements present [63-65].

2.5.2 Carbon

Carbon is known to provide matrix strengthening (by precipitation) in pipe line steels. It is known to be an effective element in controlling microstructure in steel. Carbon forms carbide and provides grain refinement and strong hardening effect in steel. The refining nature of carbon on the microstructure has studied by Den Ouden et al. [66] and concluded that the solidification substructure is essentially influenced by carbon content. In another research by Evans [67], it was found that carbon promoted acicular ferrite, at the expense of grain boundary polygonal ferrite, and caused grain refinement of the reheated regions. The strengthening of steel weld due to carbon is caused by the carbides and the number of carbide form is influenced by carbon concentration. For example Chang et al. [68], investigated the effect of carbon content on microstructural characteristics of the hypereutectic Fe–Cr–C claddings and observed that the proeutectic carbides in the hypereutectic Fe–Cr–C claddings underwent several microstructural changes in response to higher carbon content in the cladding. In another study by same author [69], they concluded that the amounts of primary $(Cr,Fe)_7C_3$ carbides increased from 33.81% to 86.14% when carbon content increased from 3.73 wt% to 4.85 wt%. However, different authors have suggested that a high level of carbides in weld metal is detrimental to the microstructure. They reported that increasing carbon content from 0.1% to 0.2%, increases the carbides formation while the impact toughness is decreased by over 60%. Therefore, the carbon levels recommended in weld metals is about 0.05 to 0.15 wt. % in order to control the amount of carbides formed. [70-71].

2.5.3 Aluminium

Aluminum is known to be a strong oxide and nitride former in the weld metal, however, the role of aluminium seems to be the most complex compare to other alloying elements. For example Bailey et al. [72] in his work suggested the complex interaction between Ti-A1 and oxygen. This work suggested that aluminium is capable of reducing titanium from either the flux and hence limit the amount of titanium oxide formation needed for the nucleation of acicular ferrite. Researchers have investigated the influence of aluminium content on weld microstructure. [73-74]]. A general conclusion shared by these authors is that as the oxygen level is raised through changes in the flux, the formation of acicular ferrite is also increased. This suggest that the effect of aluminium on microstructure can be altered by changing the flux type and the acicular ferrite formed is associated with an optimum level of aluminium. The work of Grong and Matlock [23] showed that there exist a critical ratio of oxygen and aluminium interaction in which maximum acicular ferrite is obtained. These authors found that the maximum acicular ferrite content was obtained when the ratio [% Al] to $[\%O]^2$ was ~ 28. Above this level, acicular ferrite formation was substantially reduced due to an increase in the inclusion size and a decrease in the number of suitable nucleation sites.

2.5.4 Chromium and molybdenum

Chromium and molybdenum are considered as strong hardening agents as alloying elements in weld metals. However, Mo has an effect of reducing the size of martensite packets. It Improves hardenability and thereby promotes the formation of the desired lower bainite microstructure. Bhole et al. [75] observed that increase of Mo content up to 0.881 wt. % in the WM created a-predominantly acicular ferrite weld metal microstructure with impressively improved impact toughness at −45 °C. On the other hand, chromium is a ferrite stabilizer, and it slows down austenite-to-ferrite transformation rate. It has been found to impair impact toughness, although it

promotes an increase in the percentage of acicular ferrite (AF) [76]. In another study done by Surian et al. [77], they observed that Chromium was found to be deleterious to toughness but produced a higher proportion of acicular ferrite and a general refinement of the microstructure. The effect of molybdenum and it iteration with other alloying elements on weld microstructure has also been investigated in the past. Surian et al. [78] observed that though the addition of Mo increase the hardness, yield, and tensile strengths of a ferritic high strength SMAW weld metal, Mo was found to be deleterious for toughness for 1% Mn, but yielded a maximum toughness at 0.25% Mo for 1.5%Mn. The combined presence of Ni and Mo in the WM of a submerged arc welded HSLA line-pipe steel was also studied by [75]. They observed that it decreased the volume fractions of grain-boundary ferrite (GBF) and promoted formation of high toughness of AF.

2.5.5 Manganese

The effect of manganese on the microstructure and mechanical properties of arc welds has been the subject of many investigations. Manganese is an important alloying element for solid solution strengthening. The detrimental effect of sulphur is minimized since it's able to combine with manganese to form MnS and reduces the susceptibility of a steel to hot shortness [79]. Transformation temperatures are displaced to lower values as the manganese content increases for a fixed cooling rate. Widgery [80] correlated weld microstructure with transformation temperature. He observed that a weld containing 88% acicular ferrite transformed over the approximate range 630˚ to 450˚ C, while a weld having 8% acicular ferrite transformed between 710˚ and 545˚C. Studies undertaken by Evans [81] showed that manganese increasingly refined the microstructure and promoted the formation of acicular ferrite. Both tensile strength and yield strength increased by approximately 10 N/mm2 per 0.1% Mn addition to the deposit and optimal impact is attained with approximately 1.5% Mn. Chaveriat et al. [82] observed similar phenomenon. They concluded

that Manganese refines the grain size, increases hardenability, and promotes acicular ferrite (low temperature ferrites product) by displacing the transformation temperatures to lower values. On the other hand, the increase in Mn content develops sensitivity to temper embrittlement as a result of a segregation of manganese. Svensson et al. [83] concluded that Manganese tends to segregate in the weld metal on cooling. With excessive alloying, the segregation pattern of microphases caused decreasing toughness, hence its level has to be limited to prevent manganese segregation [84]. It has been studied that reduced Mn content in steels decreases the center line microstructural banding [85]

2.5.6 Nickel

Nickel is considered to be a weak alloying element and can be added in large quantities. The addition of nickel is generally considered to improve the properties of low-carbon steels without impairing field weldability and low temperature toughness. Unlike Mg and Mo, Ni tends to form less hardened microstructural constituents detrimental to low temperature toughness in the plate (increases fracture toughness) [86]. It has a solid solution hardening effect on the microstructure. Nickel addition has been reported to have refinement influence on the microstructure. For example Taylor and Evans [87] reported that as the level of nickel was increased the amount of grain-boundary ferrite decreased and the acicular ferrite became progressively refined. This observation was equally shared by Bhole et al. [75] who concluded that the combined presence of Ni and Mo in the WM decreased the volume fractions of grain-boundary ferrite (GBF) and promoted formation of high toughness of AF. Nickel addition depresses the austenite-ferrite transformation temperature throughout the weld metal cooling range and as a result, the amount of grain-boundary ferrite decreases and the acicular ferrite formation is progressively favored [88].

2.5.7 Oxygen

Oxygen is apparently a factor of primary significance in determining the weld metal transformation behavior. Oxygen in a weld metal pool may come primarily from the flux and the atmosphere in a submerge arc welding. However, the most likely source of oxygen is the flux used in the welding process since the oxygen from the atmosphere can be reasonably controlled. The oxygen absorbed in the weld pool will combine with deoxidizing elements to form oxides, part of which are entrapped and will remain as non-metallic inclusions in the weld metal since the solubility of oxygen in weld metal is extremely low [89]. Several studies have been made on SAW fluxes and the reactions of these fluxes with the molten metal during welding [90-92]. Dallam et al. [93] observed that at high oxygen content, a higher percentage of grain boundary ferrite (ferrite veining) was observed. By reducing the oxygen in the weld metal, the amount of acicular ferrite was increased. With further reduction of weld metal oxygen, the main microstructural feature, instead of acicular ferrite, became bainite. Previous investigations [94-96] indicate that oxygen affects the weld metal microstructure and the mechanical properties in the form of inclusions. Oxygen exists in the weld in the form of finely dispersed oxygen-rich inclusions. These inclusions may be a product of the deoxidation process or result from some solid state transformation (97). It has been well researched that oxygen content in a weld metal pool play significant role in the formation of sufficient amount of non-metallic oxide inclusions. Increasing weld metal oxygen content have a direct effect on the microstructure of the weld metal. Chaveriat et al. [82] investigated the role of oxygen and manganese in a low carbon steel weld metal microstructures of a submerged-arc welds. They observed an increase in acicular ferrite as the oxygen level is reduced from 1400 to 400 ppm. However, below an oxygen level of 250 ppm, further reductions in the oxygen content reduce the amount of acicular ferrite as bainite formation increases. This result is also very consistent with

that of Francis et al. [98]. The volume fraction of acicular ferrite is definitely influenced by the oxygen and carbon dioxide content in the argon cover gas.

2.5.8 Silicon

Strong oxidizing elements such as Si are added to suppress the formation of cementite and thereby stabilize the austenite by enriching it with carbon. However, due to its strong affinity for oxygen, Si readily forms oxides. Researchers have investigated the role of silicon on the weld microstructure and mechanical properties. Sun et al. [99] observed that the mechanical properties of austempered ductile iron (ADI) weld increased with increasing Si content, but an excess of Si (3.79%) resulted in decreasing the austemperability owing to decreased carbon content of the matrix austenite. However, different authors have observed contradictory behaviour concerning the exact role of silicon in weld metal microstructure. Dorschu and Stout [100] reported that silicon in the range 0.35 to 0.8wt% has no effect on microstructure on the other hand, it was reported that by increasing silicon content from 0.2 to 0.4 wt %, the structure was changed from side plate to acicular structure [101]. Opinion shared by another researcher is that increase in silicon level encourages the formation of acicular ferrite at manganese levels below 1 wt. %. However, at higher manganese levels the influence of silicon is less marked. [81]

2.5.9 Titanium, niobium and boron.

Titanium and niobium is known to be strong former of carbide and nitride. Fine carbide or nitride particles are able to hinder the movement of grain boundaries, thus reducing the grain size by making grain growth more difficult. The reduction in grain size increases their strength and toughness at the same time through precipitation hardening. Oxide inclusions of Ti(C, N, O) are formed in the weld metal when titanium react with oxygen. These oxide inclusions serves as nucleating sites for the formation of acicular ferrites microstructure. Inclusions containing Ti and

Nb have been reported as good nucleating sites for AF. However, trindade et al. [102] reported that high Nb content reduces the AF amount in the weld metal while GBF and WF is increased resulting in decreased weld toughness. Few research has indicated the role of titanium on the weld microstructure. Beidokhti et al. [103] investigated the influences of titanium and manganese on high strength low alloy SAW weld metal properties and observed that addition of titanium in the range of 0.02–0.08% increased acicular ferrite in the microstructure as well as the impact toughness of the weld metal was improved by addition of titanium, but beyond the optimal titanium percentage, a quasi-cleavage fracture mode appeared in the specimens. Boron on the other hand enhances strength and toughness in the weld metal because it suppresses the formation of GBF. Lee et al. [104] investigated the effect of boron contents on weldability in high strength steel and observed that the volume fraction of acicular ferrite and the absorbed energy decreased with increasing boron contents of about 32 to 60 ppm but significantly decreased with increasing boron contents from 60 ppm to 103 ppm while upper bainite instead of acicular ferrite were seen to form in the 103 ppm boron weld metal. This result was found to be consistent with that of Oh et al. [105] who observed that the largest volume percent of acicular ferrite was obtained in a weld containing 42 ppm of weld metal boron and 420 ppm of weld metal titanium.

2.6 Effect of inclusions on weld metal microstructure.

The development of ferritic microstructures in steels has been extensively studied [106-109]. It is generally believed that the formation of acicular ferrite improves the mechanical properties of steels and weld metals especially the impact toughness due to the interwoven nature of fine ferrite plates. This microstructure significantly prevents the initiation and propagation of cracks. [109,110]. several authors have studied the role of inclusions in the development of the acicular microstructure [111-113]. For example, most authors concluded that oxide and nitride inclusions

are necessary for nucleating of acicular ferrites [106, 114-115]. The absence of inclusions in weld metals may result in the formation of other microstructures such as bainite which is considered detrimental to weld toughness and offers little resistance to crack propagation.

These inclusions are primarily from the reaction between dissolved Al, Ti, Si and Mn with dissolved O, S and N. Wan et al. [116] observed that acicular ferrite laths or plates were formed by multiple nucleation on inclusions and sympathetic nucleation or repeated nucleation on the pre-formed ferrite grains. These inclusions mainly consisted of Ti, Al, Si, Mn and O elements in weld metals. Inclusions restrict the growth of austenite grains but at the same time also provide nucleation sites for AF. Fattahi et al. [117] concluded that the percentage of acicular ferrite was increased due to the uniform dispersion of inclusions containing Ti and the pinning force of oxide nanoparticles against the growth of allotriomorphic ferrite and Widmanstätten ferrite from the austenite grain boundaries. It has been found that the flux chemistry affects the chemistry and morphology of inclusions. In order to properly control the microstructure of a weld metal and encourage the growth of acicular ferrite, it is important to ensure the correct concentration of flux chemistry since it has been determined to have a direct correlation with the total oxygen content in the weld [82].

2.7 Hydrogen induced cracking in pipeline steels

There are many studies that relate the occurrence of hydrogen induced cracking (HIC) in carbon steel pipeline [118-120]. It has been widely researched that hydrogen-induced blistering and internal cracking can develop in steels without application of external load, when they are exposed to an environment with a high hydrogen content. This is very typical of pipeline steels and pressure vessels in contact with environment containing wet hydrogen sulphide or hydrocarbons. It is believe that hydrogen diffuses in the form of protons inside the structure of the pipe by a means of

superficial surface corrosion of the steel [121-122]. And as a results several theories have been considered useful in explaining the concept of hydrogen embrittlement. One of the most acceptable theory is the internal pressure theory proposed by Zappfe and Tetelman [123-124]. This theory claims that the hydrogen atoms are absorbed into the bulk material where they are accumulated at different structural defects sites, further aggregation of hydrogen at this site results in a big internal pressure, resulting in blister formation and or crack. Hydrogen can be introduced into steel in mostly two ways; during manufacturing or repair process and during service conditions. Absorption during manufacturing may be during steel making, hot working, heat treatment, welding, electroplating and from hydrogenous atmosphere. In the case of linepipe, welding provides an excellent means of joining pipelines. However, steels can absorb small concentration of hydrogen during welding or due to exposure to sour environment. Hydrogen can be introduced into linepipe steel during service conditions by exposure to hydrogenated liquid or gases., therefore care must be taken to ensure that hydrogen uptake during welding is completely reduced to possible minimum.

2.7.1 Role of microstructure in hydrogen induced cracking

During welding, it has been well researched that certain microstructures such as acicular ferrites are preferable since it improves the toughness and hardenability of the weld structure and provide maximum resistance to crack propagation by cleavage [29, 125]. During hydrogen permeation, hydrogen concentration may exceed a critical level, leading to hydrogen induced cracking. It has been studied that cracking in H_2S environment is facilitated by the presence of non-metallic inclusions such as MnS and a banded structure [126]. The mechanisms for these cracking phenomena in steel welds is greatly depended on microstructural parameters like composition, structure, and morphology of non-metallic inclusions as well as mechanical and environmental

parameters, such as applied stress, type of liquid or gas being transported, and groundwater chemistry, among many others. [127-129]. Several authors have researched the role of non-metallic inclusion, carbides, grain boundaries, dislocations and regions with high stress concentrations as potential reversible trapping sites for hydrogen. Traps are generally classified as reversible and irreversible. This classification is considered to be based on the strength of their bond with the hydrogen atoms. Reversible traps have low trap binding energies while irreversible traps are those that trap hydrogen permanently and are associated with high binding energies at temperatures close to ambient. Micro voids, dislocations and grain boundaries are considered to be reversible traps as they have the capacity to affect the diffusion of hydrogen. For example grain boundaries can either increase the diffusion of hydrogen or reduce the mobility of hydrogen by providing faster paths for diffusion or act as reversible hydrogen trapping sites at nodes and junction points [130-134]. On the other hand, non-metallic inclusions and precipitates are considered irreversible traps. Inclusions, complex or double oxide and mixed compound such as Al_2O_3, (Fe, Mn)S, $FeO.Al_2O_3$, and Al-Mg-Ca-O have been identified in linepipe steels. However, MnS inclusions have been identified by researchers to be strong irreversible trapping sites for hydrogen [135-137]. Ren et al. [138] has proposed that internal cavities can occur due to the aggregation of hydrogen atoms and vacancies at trapping sites in the microstructure and that the internal hydrogen-filled cavity can initiate cracking at the edges of the cavity due to the internal hydrogen pressure on reaching a critical size. It is a well acceptable fact that microstructure of the steel, grain size, precipitates, the nature of grain boundary and the formation of second phase particle plays strong role in HIC nucleation and propagation [120,139]. Nanninga et al. [140] investigated the role of microstructure, composition and hardness in resisting hydrogen embrittlement of fastener grade steels and concluded that the overriding factor contributing to

susceptibility of the steel was strength. They also observed that the degree of susceptibility of the microstructures to hydrogen embrittlement ranked in increasing order of fine pearlite, bainite, and tempered martensite. The role of ferrite in hydrogen embrittlement induced has also been investigated in the past by authors [141-142]. A general conclusion shared by these authors was that susceptibility to hydrogen embrittlement increases as the ferrites content increases. However Ohnishi et al. [143] pointed out that the effect of delta ferrite content up to 12% on the hydrogen absorption of this type of weld metal is not so clear. Attempts have been made to obtain quantitative crystallographic data that is useful in interpreting the relationships that exist between the crystallographic characteristics and HIC behaviour in linepipe steels using the EBSD technique [144-145], however not enough study has been done that clearly provides crystallographic explanation to the mechanism of crack initiation and propagation in acicular ferrite microstructure in linepipe weld due to hydrogen embrittlement. Indeed, the relationship between microstructures and HIC susceptibility of linepipe weld needs to be studied in order to understand the cracking problems induced by hydrogen in the welded region of linepipe used for sour service. Many authors have applied the EBSD tool to provide some important cues for understanding the crystallographic orientation of grains as well as the orientation surrounding the crack initiation sites [121,146], but to date, not much studies have been done on the occurrence of HIC in welds using this tool, as most research has been on the effects of inclusions and processing parameters of the steels. It is therefore important to understand the kinetics of crack initiation and how it relates to the microstructure of the linepipe weld.

2.7.2 Hydrogen charging

Different method has been used to induce HIC in linepipe weld in the past. Among this methods are the gaseous charging and cathodic or electrolytic charging method. The most commonly used

is the electrochemical charging method. This method has been applied by many researchers because it provides a more severe environment for charging compared with the gaseous charging method. [147-148]. Although it is recommended that gaseous charging method be used as it provides a reduced concentration gradient and represent the likely conditions in which pipeline materials will encounter during service [147]. In electrolytic charging, electrolyte is employed. During charging, hydrogen exist in the electrolyte as positive protons, and can be absorbed into the metal surface. This atom is either combined with another atom or migrate into the bulk of the material [149]. In addition to the electrolyte, poison or inhibitors such as arsenic, ammonium thiocyanate, and sulphur are added to promote hydrogen ion absorption and inhibit molecular hydrogen formation. For example, different authors have employed AS_2O_3, ammonium thiocyanate (NH_4SCN) during hydrogen charging in sulfuric acid solution. [146, 150]. In gaseous hydrogen charging, diffusion is the main method of transport. Hydrogen diffusion is driven by the temperature of the system and the chemical potential gradient in the system [151-152]. Generally, it is difficult for molecular gaseous hydrogen to penetrate into the steel. In order for this to happen, the hydrogen molecule must dissociate itself into hydrogen atoms through reactions of metal hydrides or electrochemical reactions [153]. This dissociation process requires energy and this was estimated by [154] to be 434.2kJ/mol. However, this energy requirement may be boosted at the surface of specimen because atomic lattice diffusion and dislocation movement may facilitate the transport of atomic hydrogen.

2.8 linepipe weld microstructure and failure

Microstructural variations across a weld joint has been reported to pose problems to pipeline steels because the material properties are strong functions of microstructure [155]. Alloy systems in which phase transformations take place in the solid state when cooled from high temperatures

(carbon steel/alloy steel) are reported to have more variation of microstructure and as a result mechanical properties are affected. For alloys systems such as stainless steels where there is no phase transformation in the solid state, it poses problems of hot cracking in austenitic stainless steel and lamellar tearing in the steel weld joint due to segregation of elements such as carbon, phosphorus, sulphur e.t.c. [155, 156].

The development of microstructure in a weld joint has been widely studied in the past [22, 23]. For example, Smith et al. [24] characterized the microstructure of a submerged arc welded HSLA 80 steel using an optical microscope and identified the formation of acicular ferrite (AF), grain boundary ferrite (GBF), ferrite with second phase, aligned FS(A) and nonaligned FS(N) and polygonal ferrite (PF). Other authors have reported the presence of other microstructures such as Widmasttaten ferrite (WF), bainite (B) and martensite. They have attributed these structures to certain welding conditions and parameters [24].

Attempts have been made to relate the mechanical properties of a weld to its microstructure. For example certain microstructure such as acicular ferrite has been found to be preferable when it comes to improving the toughness and hardenability of a weld structure which is said to provide maximum resistance to crack propagation by cleavage [29,125].

Several authors have studied the development of acicular ferrite. Chaveriat et al. [82], studied the role of oxygen and manganese in a low carbon steel weld metal microstructure and concluded that the content of both elements in the weld metal definitely influence the weld microstructure, stating

that high oxygen levels decrease hardenability by promoting nucleation sites for the formation of high temperature ferrite while manganese refines the grain size, increases hardenability and promotes acicular ferrite by displacing the transformation temperatures to lower values. Other authors have analyzed the role of inclusion and sizes of inclusion in promoting such a microstructure, suggesting that the promotion of acicular ferrite are reduced if the size and number of inclusions decreases since they acts as nucleation sites for the formation of acicular ferrite, hence allowing direct transformation of austenite at temperatures where bainite and martensite are stable [96].

In order to clearly understand the developing microstructure in a weld, several parameters such as welding speed, heat input etc. need to be considered. For example Bayraktar et al. [157], studied the role of the direction of heat flow by observing in interstitial free steels in which welded joints are characterized by the presence of very large grains near the fusion line and these grains are oriented along the directions of the large heat flow. Boumerzoug et al. [158] also showed that for an industrial low carbon steel, the structure is strongly “oriented” and is in some aspects very similar to certain solidification microstructure, whose morphology depends also on heat flow. On the other hand, it has been found that solidification theory can be applied to welding [157-158].

Apart from microstructure, another important issue in welding is residual stress. These are stresses that remained in a material in the absence of external load. Several methods such as neutron

diffraction, X-ray diffraction, hole drilling, impact indentation etc. have been developed for measuring residual stresses that are developed after welding [159-164]. It is generally believed that welding produces tensile residual stress, and therefore require stress relief after the weld process [165-166]. However, different authors have observed the presence of both tensile as well as compressive stresses at the weld. For example, Hong Tae Kang et al. [167] investigated the effects of residual stress and heat treatment on fatigue strength of weldments specimens using both X-ray diffraction and hole drilling method. They stated that compressive residual stresses on the surface were obtained from the as-welded specimens, while zero or very low tensile residual stresses were obtained from the heat-treated specimens explaining that the compressive residual stresses on the specimens tested could have been developed due to the difference of cooling rate at surface and sub-surface of weldment. The surface was cooled earlier than the sub-surface and the hard surface constrained thermal shrinkage of the sub-surface, which resulted in compressive residual stresses on the surface of the welded toe area.

Residual stress has been reported to be influenced by many factors including manufacturing processes, chemical compositions, thermal constraint and material properties of the base metals. The distribution of residual stress around the weld is also determined by factors such as welding procedures, geometry of the parts been joined as well as welding fixtures [168].

On the role of residual stress to weld failure, more than the absolute values of the residual stress, it is the stress gradient that is important for any failure and in order to reduce the stress gradients, post weld heat treatment is carried out so that not only the stresses are reduced but the stress gradients are brought down as well. [155]. It must be stated that failure of weld is not solely due to residual stress alone, rather a combination of several factors such as inclusions and mechanical stresses during service, for example, Lin et al.[169] reported a catastrophic failure of an API 5L X52 spiral welded pipe along the weld line. By close examination of the microstructure of the failed pipe, they showed that the pipe failed as a results of the presence of inclusions aligned along the fiber rolling texture in the base metal. They also concluded that the combination of welding residual stresses and stress concentration played a great deal in the easy propagation and growth of crack along the weld line and the subsequent failure of the pipe.

Amidst other factors, thermal constraint has been reported to be a major factor in raising the residual stresses during welding in offshore installation of linepipe. Zeinoddini et al. [170] analyzed the effect of after weld repair on the residual stress distribution. They develop an experimental investigation of the welding and repair process operated in offshore pipelines during fabrication to remove inspected defects and measured the residual stresses due to repair welding by means of hole drilling and sectioning methods. They showed that the residual stresses are quite large, compared to the original welded pipe.

Many work has been done in order to minimize the amount of residual stress after a welding operation. For example, Dewan et al. [171] studied the effect of post-weld-heat-treatment (PWHT) on the residual stresses, grain size, micro-hardness and tensile properties of AA-6061-T651 aluminum alloys (Al-Mg-Si). They observed that lower residual stresses are obtained in the post-weld heat treated specimens and concluded that the post-weld heat treatment enhanced tensile properties for the redistribution of microstructures and residual stresses. On the influence of microstructure and residual stress, Kang et al. [172] compared the fatigue life of two weldment, they observed that cracks initiated and propagated in the weaker welded material and not in the stronger HSLA eye bar and concluded that the effect of residual stresses overwhelmed that of microstructure on fatigue strength of welded.

Understanding pipeline failure requires a broad approach that must take into account several factors involved in the manufacturing process. In the past, failure in pipeline weld has also been attributed to manufacturing defect. Bernasovsky [173] carried out a report of cases of failed spiral welded pipes. In this case (spirally welded pipe OD 720 x 8 mm) 1.8 m long crack was running along the spiral weld. The initiation point was in the place where the spiral weld meets the tie strip weld. He stated that the spiral weld exhibits very high misalignment of both linear and opposite runs and concluded that the crack was initiated by liquid metal embrittlement (LME) of remelted copper which came from abrading of Cu electric contact rods applied during manufacturing.

CHAPTER THREE

MATERIALS AND METHODOLOGY

3.1 Materials

API X70 pipeline steel was used as the base metal. The line pipe was welded with a double V-shaped weld pool by the submerge arc welding (SAW) technique. Two welding passes were applied to complete the joint. The chemical composition of the X70 base metal and the welding parameters used are summarized in Table 3.1 and Table 3.2, respectively. The current and voltage used in the welding are represented by "I" in amperes and "V" in volts, respectively, and the heat input is represented by "HI" in kJ/mm. The lead and trail are the different electrodes used in the weld process.

Table 3.1. Chemical composition of base metal.

Element	C	Mn	P	S	Si	Cu	Ni	Cr	V	Nb	Ti	Al	N	Ca	Sn	C.E
Wt. (%)	0.06	1.59	0.014	0.002	0.2	0.24	0.13	0.09	0.003	0.079	0.012	0.03	0.004	0.0038	0.003	0.24

Table 3.2. Welding parameters used.

Diameter (Inches)	**Travel Speed** (IPM)	**Inner Weld**						**Outer Weld**					
		Lead			**Trail**			**Lead**			**Trail**		
19	42	**I** (A)	**V** (Volts)	**HI(**KJ/mm)	**I** (A)	**V** (Volts)	**HI(**KJ/mm)	**I** (A)	**V** (Volts)	**HI(**KJ/mm)	**I** (A)	**V** (Volts)	**HI(**KJ/mm)
		750	30	1.34	540	34	1.03	1000	32	1.80	600	36	1.8
Electrode		LA-81			LA-90			LA-81			LA-90		
Flux		OK 10.77			Ok 10.77			Ok 10.77			OK 10.77		

3.2 Hardness test

The micro hardness tests were conducted using a Mitutoyo [MVK-H1] micro Vickers hardness testing machine located in room ENG2C25. The specimen was subjected to a load of 200 gf for 10 seconds. Five hardness measurements were obtained for each point and the averages are reported. The hardness profile map measurement was conducted using a Durascan-70 Automatic Hardness testing machine equipped with ecos-workflow software for generating the hardness map using an interval of 1 mm between test points.

3.3 X-Ray Diffraction

The residual stress measurements was done using a Bruker AXS with an area detector system and Cr K_α radiation to collect the X-ray diffraction patterns. The shift in the position of diffraction peaks was used to estimate the strain in the samples. During post processing of the acquired data, these strains were analytically converted into stresses. The interplanar spacing for (hkl) pole is expressed as Eq. 3.1 [174]:

$$d_{hkl}(\psi\varphi) = d_0 \left[1+s_1(\sigma_{11}+ \sigma_{22})+1/2s_2\sigma_{\varphi} \sin^2(\psi)\right] \quad (3.1)$$

where ψ is the angle between the specimen normal (z-axis) and the direction of strain measurement, φ is the rotation angle that the goniometer has undergone at any instant of the measurement, d_0 is the interplanar spacing of the unstrained material, s_1 and s_2 are the X-ray elastic constants, σ_{11} and σ_{22} are the stresses expressed in the sample reference frame, and σ_{φ} is the residual stress of the material. The ψ angles used for the ferritic steel were 0, 10, 20, 30,40,50,60 and 70º. The {200} planes with a peak at the 2θ value of 106.6º were considered for the measurements. All the data were corrected for the errors caused by the effect of background and absorption.

3.4 Electrochemical hydrogen charging.

An electrochemical charging method was used to induce HIC in the specimens. In this work, a charging set up described in the previous work by Mohtadi-Bonab et al. [146] was used to induce HIC in the test plates containing the welds. In this method, 0.2 M sulfuric acid solution was used for charging and 3 g/l ammonium thiocyanate (NH4SCN) was added to the solution as a recombination poison to prevent formation of hydrogen bubbles on the surface of the specimen and as a result increase the amount of hydrogen entering the steel. Two specimens from the as-received weld plate were cut with dimension 25 mm x 19 mm x 4.2 mm. All specimens were ground with 120, 220, 500 and 600 SiC emery paper to remove the rough weld surface and degreased using acetone ultrasonically for 15 minutes. The specimens were then separately placed in a glass test vessel and the vessel was filled with 2 L of charging solution. The current was supplied by an Instek DC power supply with a constant current of 20 mA/cm^2. The steels were then electrochemically charged for 4 hours and 24 hours. In order to prevent the decrease in pH of the charging solution through evaporation, the glass vessel was firmly covered with a para film. For the tensile specimen, each specimen was charged for 5, 10, 15 and 30 minutes, while another batch was charged for 2 and 10 hours.

3.5 Microstructural evaluation

In this work, convectional metallographic preparation procedure were used. The specimens were hot mounted and ground with 120, 220, 500, 600 and 800 SiC emery paper to remove the rough weld surface. This was preceded with 2000 and 4000 SiC emery paper. In order to produce a shining and mirror-like surface finish, 9 µm MD-Largo cloth with 9 µm MD-Largo suspension were used. Diamond polishing was done using 3 µm MD-Mol with 3 µm MD-Mol suspension and 1 µm MD-Nap cloths with 1 µm MD-Nap suspension. For optical microscopy (OM) examination,

the surface of the steel was etched using a 2% nital solution. The optimum etching time for each steel used in this study was 10 s. The optical microscopy evaluation was carried out using Nikon MA100 inverted microscope with a Pax-it! Image analysis software.

3.6 Scanning electron microscopy observations and electron backscattered diffraction measurements

For SEM and EBSD microstructural characterization, specimen were machined, samples were firstly polished using conventional metallographic polishing techniques above and followed by colloidal silica polishing using a vibrometry device for 8 hours. SEM, and EBSD studies were conducted using a field emission scanning electron microscope (Hitachi SU 6600) equipped with an Oxford Instruments NordlysNano EBSD detector that acquired diffraction patterns using AZTEC 2.0 data acquisition software (compatible with the detector) with a binning of 8 × 8 pixels. The microscope was operated with primary electron energy at 30 keV and a step size of scans (0.145 μm) was maintained for all the measurements. When EBSD measurements were completed, the EBSD raw data was analyzed using Oxford Instruments Channel 5 post processing software. Initial post processing of the raw data consisted of removing mis-indexes and wild spikes. This software allows the identification of the grains and grain boundaries. Grain boundaries (GB) are defined as continuous regions of misorientation (misorientation angle >5º) between grains. GBs with a misorientation angle below 10º were considered as low angle GB (LAGB). Average misorientation is also calculated within the grain at each measurement point with respect to all eight neighbor sites (in a square grid) provided that any of this misorientation not exceeds 5º [175].

3.7 Void Size Statistics

In order to measure size and distribution of voids in the sample, at list five SEM micrographs were acquired in two magnifications of X500 and X1000 for different areas in the weld. The micrographs were then imported to visual basic (VB) software for calibration. The voids were then counted and averaged over each area.

3.8 Transmission electron microscopy (TEM)

TEM was used to analyze the WM microstructure and inclusions more closely to help understand the features associated with AF development. TEM study was done using FEI's Tecnai Osiris in Canmet MATERIALS Laboratory, Hamilton. The TEM is equipped with X-FEG gun operating at 200 keV. The samples were prepared using precision ion polishing system (PIPS). Conventional bright field, dark field imaging, selected-area diffraction (SAD), convergent beam electron diffraction (CBED) techniques were used for phase identification and crystallography. The STEM mode using bright field (BF) and high angle annular dark field (HAADF) detectors were used in combination with EDS. The EDS mapping was done using ESPRIT software, and deconvolution of overlapping peaks was applied.

3.9 Tensile test

In order to understand the role of tensile stress on HIC susceptibility in pipeline steels the experimental setup shown in Fig.3.1 (a) was used to conduct tensile test experiments. The setup can be also used for the stress corrosion-cracking (SCC) test, hence it is named the environmentally assisted stress-cracking system (EASCS). Fig.3 (b) shows the specimen configuration in inches used for the tensile test. The specimens used are categorized as received and charged. The strain rate for the tensile experiment was 0.000787/s.

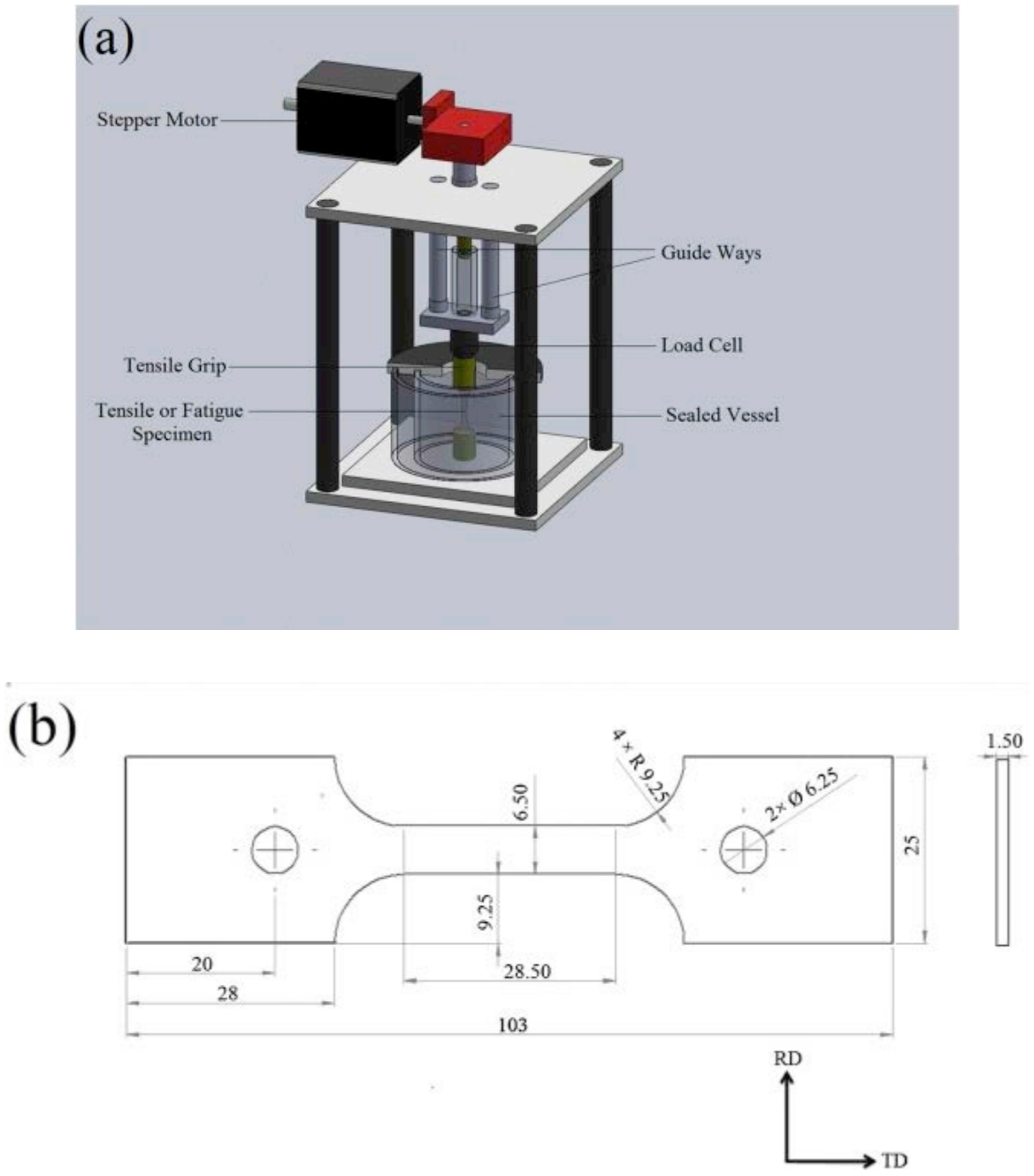

Figure 3.1 (a) EASCS setup used for tensile test and (b) tensile test specimen.

CHAPTER FOUR

RESULTS AND DISCUSSION

This chapter begins with characterization of the X70 steel, the WM and HAZ. Additional data on grain size, kernel misorientation and grain boundary statistics are provided. In-depth discussion on the nature of acicular ferrite and inclusions in the different zones of the weld using TEM would be carry out. In this chapter, detail discussion will be done on the nature of residual stresses developed in the welding process using X-ray diffraction, the hardness distribution around the weld and recrystallization phenomena that resulted from thermal cycles.

The chapter ends with the discussion on the effect of hydrogen on crack initiation, propagation and the role of microstructure in HIC.

4.1. Microstructure characterization of X70 pipeline welds

The microstructural characterization was carried out in different regions of the welded joint as indicated by arrows in Fig. 4.1 in order to assess the impact of welding on the steel microstructure.

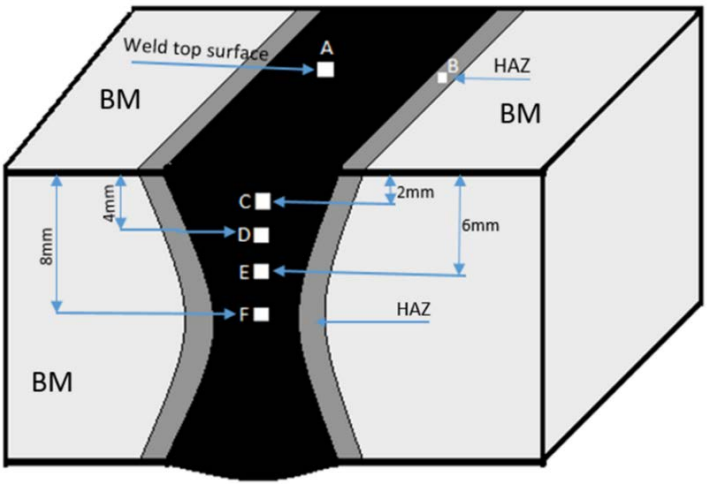

Fig. 4.1. Schematic of the weldment indicating different positions used for EBSD and optical microscopy investigation.

Fig. 4.2 show the microstructure of the base metal in X70 steel. Fig. 4.2(a) and 4.2(b) show the inverse pole figure (IPF) map and band contrast images obtained from the EBSD pattern imposed with grain boundaries respectively. It can be clearly seen that the microstructure has equiaxed ferrite grains. Grain boundaries are displayed in different colors according to the defined grain boundary misorientation. Grain boundaries having misorientations less than 5º are regarded as low-angle grain boundaries (LAGB) and are represented by red lines while the blue lines represent those with misorientations of 5 to 10º. The black lines represent high-angle boundaries (HAGBs) with misorientation of 15º or higher. Fig. 4.2(b) shows a distribution of all the grain boundaries typical of hot rolled steels and may be attributed to the manufacturing process. Fig. 4.2(c) shows the optical microstructure of the base metal that was etched in 2% natal solution. It can be seen that the microstructure is typically an equiaxed ferrite/pearlite microstructure and this is in agreement with results obtained from EBSD in Fig. 4.2(a).

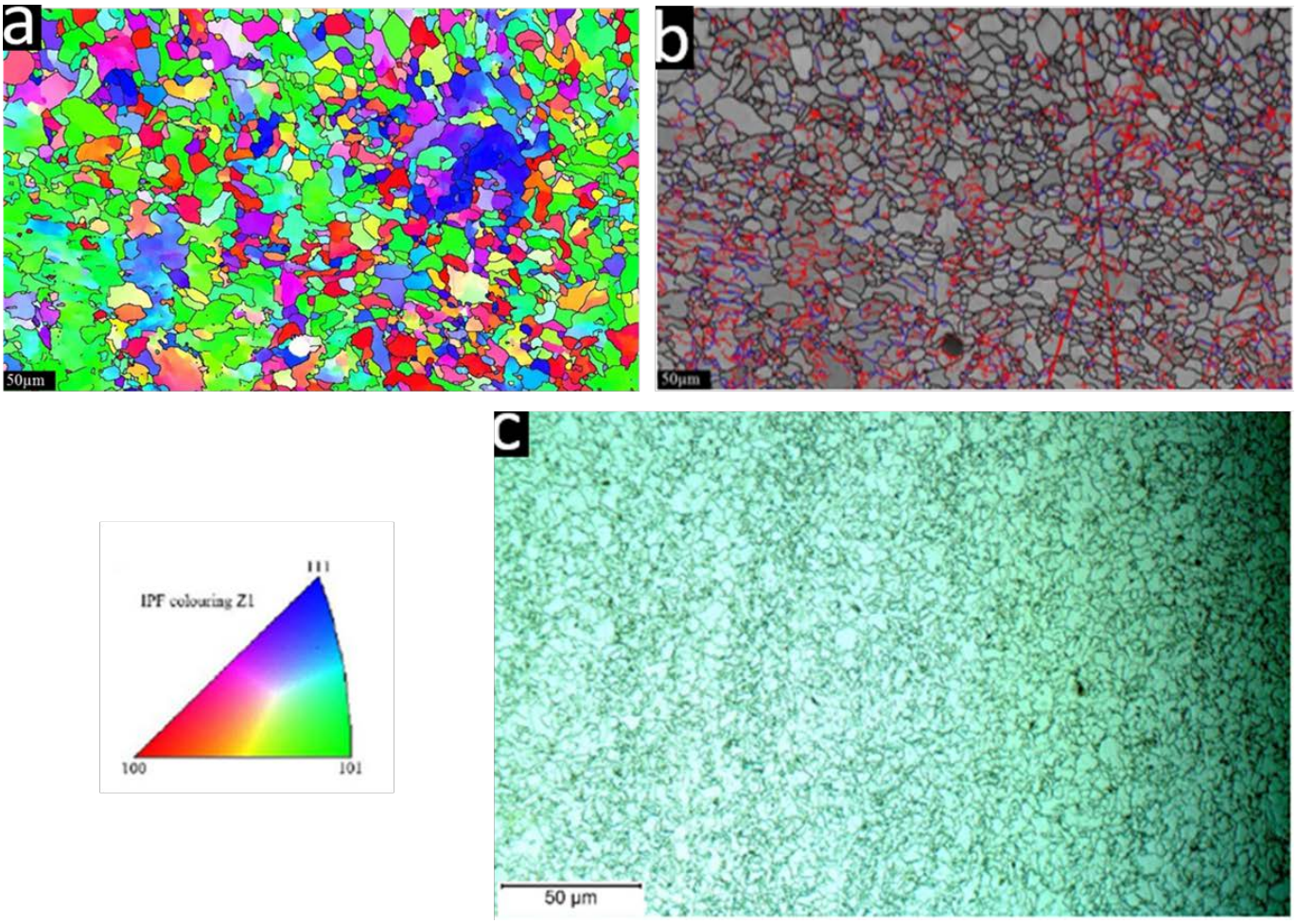

Fig. 4.2. (a) EBSD scan map (b) image quality with imposed grain boundaries and (c) optical micrograph of the base metal.

Fig. 4.3(a) is an EBSD scan of the WM corresponding to point A in Fig. 4.1. The weld microstructure shows a colony of grains which are of certain crystallographic orientation but contain submicron grains which are predominantly acicular ferrite grains. Fig. 4.3(b) is a scan of each packet or colony shown in Fig. 4.3(a). It shows the acicular ferrite and it inter-locking features. The AF plate microstructure represents an intragranular ferrite grains with an aspect ratio of 4:1 derived from non-metallic inclusions [176]. The characteristic microstructure of AF has been defined by other authors [176,177] to be fine grain size, irregular-shape and align in arbitrary directions. Such microstructure can be grouped into packets having the same orientation between

neighboring laths, it is regarded as an excellent microstructure with good strength and toughness. Fig. 4.3(c) represent the band contrast with imposed grain boundaries, it can be seen that most of the grain boundaries between the acicular ferrite microstructure are HAGBs. Such boundaries can create obstacles to cleavage crack propagation because of the frequent change of the crack propagation path [178]. Fig. 4.3(d) is the optical microscope image of the WM. This area is typically comprised of acicular ferrites and this observation is consistent with that data obtained from EBSD in Fig. 4.3(a) and Fig. 4.3(b).

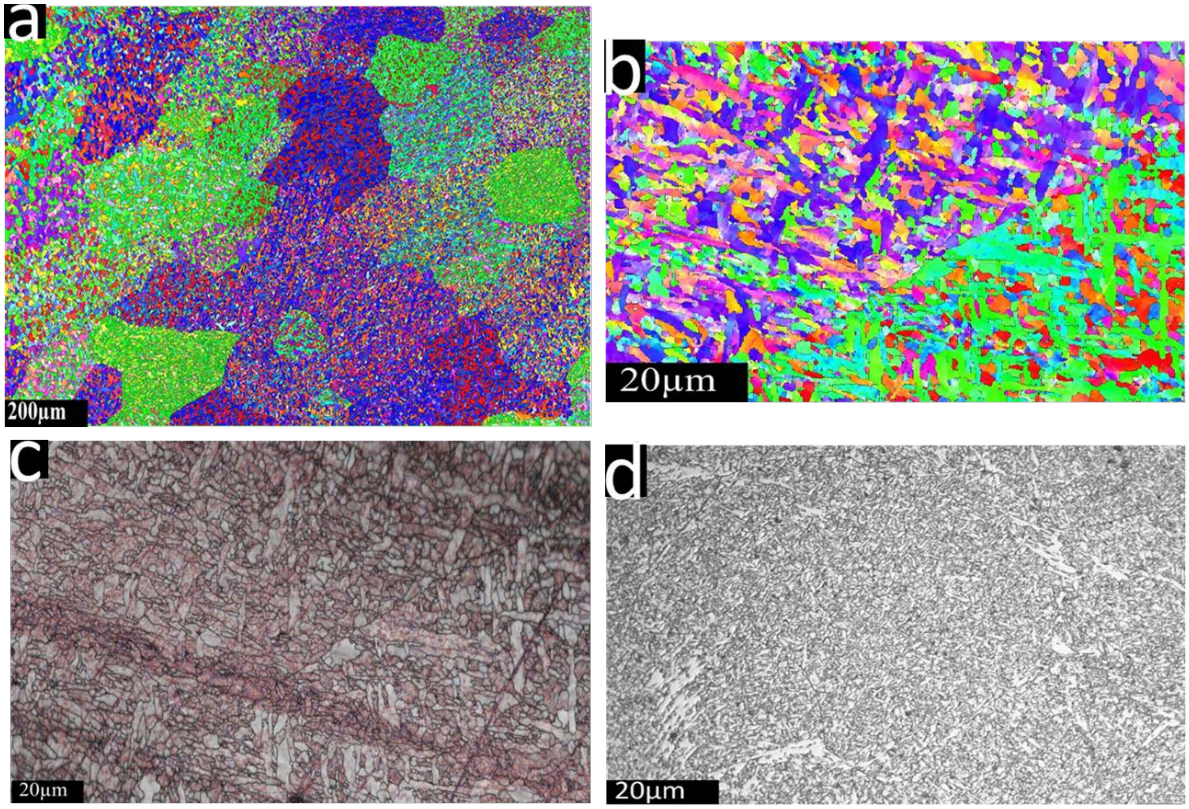

Fig. 4.3. (a) EBSD scan map of the weld metal (b) high resolution EBSD scan of weld metal (c) image quality (IQ) map with imposed grain boundaries and (d) optical micrograph of weld metal.

Fig. 4.4 shows the EBSD map and the image quality of the HAZ corresponding to point B (Fig. 4.1) with imposed grain boundary. Fig. 4.4(a) illustrates the coarse-grained and fine grained HAZ microstructure. These zones consist of bainite, martensite and ferrite. It can be seen that the grain size of the HAZ changes gradually when moving from the fusion zone. Since the CGHAZ is the zone that is closest to the fusion zone, the grains in this zone tend to grow and become coarse. The coarsening of the microstructure is due to high heat input during the weld process. It is well known that during welding, the HAZ does not experience melting but, a microstructure is changed due to phase transformation; the region closest to the weld experiences the highest temperature and as a result appears to have largest grains compared heat affected zone that is farther away from the weld [179,180].

Fig. 4.4(b) show different subzones of the HAZ. One can see that there is variation of the grain boundary structures with distance from the CGHAZ to the FGHAZ. The volume fraction of low angle grain boundaries with misorientation less than 5° is observed farther away from the CGHAZ. The distribution of HAGBs is also observed to be less in the CGHAZ compare to FGHAZ. HAGBs has been reported to be good for maintaining good toughness in the HAZ since its able to arrest crack propagation [181,182]. It should be noticed that in all subzones, although the densities of low angle boundary are different, most of the low angle boundaries (blue line and red line) and appear to be found within the prior austenite grains. This indicates that the grain coarsening mechanism in the prior austenite grain may have played a great role in this phenomenon. It is therefore of interest to investigate the overall distribution of grain boundaries that may exist within the austenite grain. Fig. 4.4(c) is an optical image showing prior austenite boundaries. The microstructure is a ferrite matrix with lath bainite and M/A constituent.

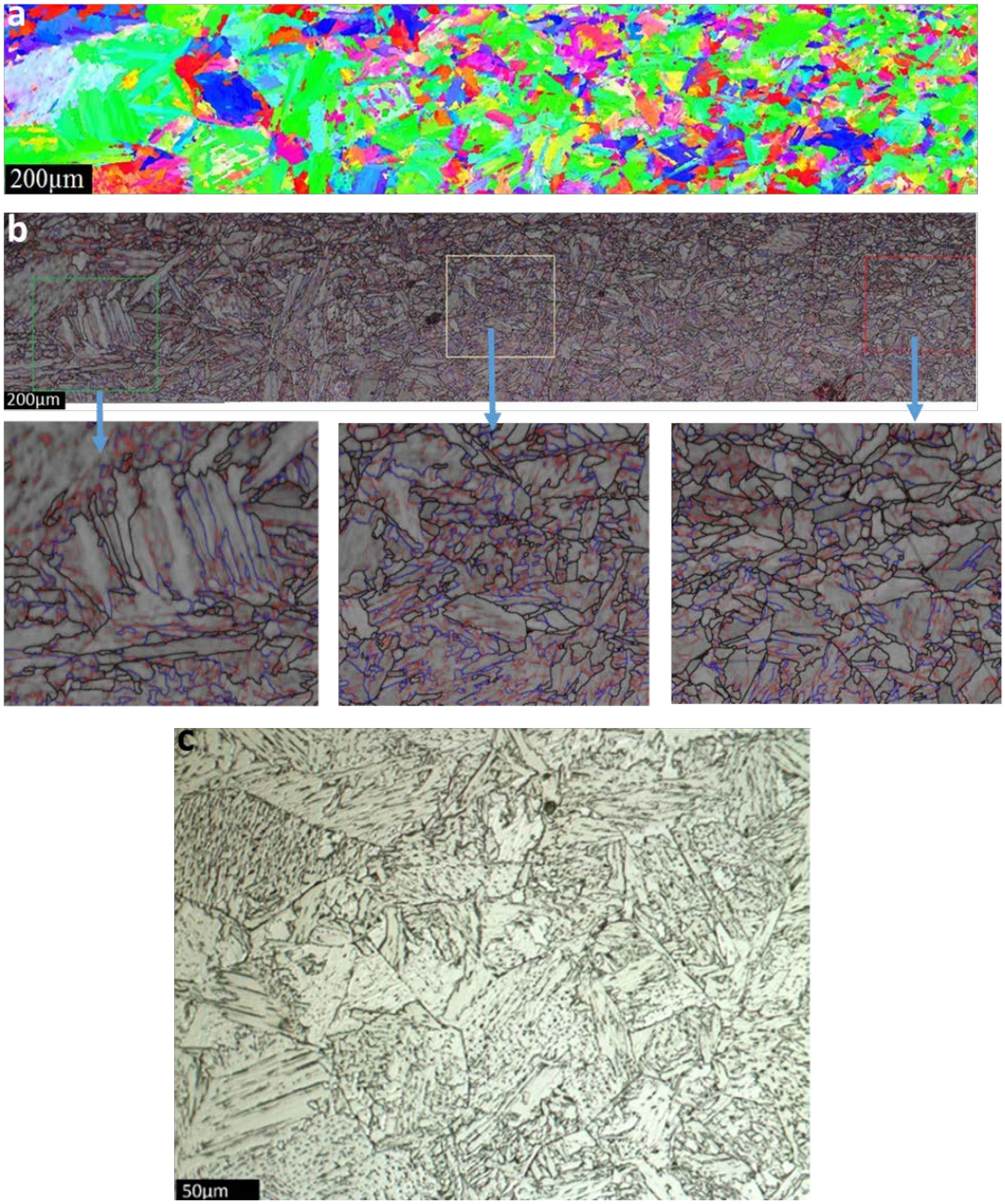

Fig. 4.4. (a) EBSD map (b) image quality with imposed grain boundaries showing the subzones and (c) optical micrograph of the HAZ.

Fig. 4.5 shows the EBSD map, image quality and OM image at the interface of the WM and HAZ (Fig. 4.1). Fig. 4.5(a) shows the microstructural changes that occur as a result of the welding process in the various regions. The morphology of the grains in different regions is clearly observed in the image (Fig. 4.5(a)). It can be seen that the grain size increased when compared to

the initial base metal grain size. (Fig. 4.2(a)). The figure showed that the grain size gradually varied with distance from WM to HAZ. Fig. 4.5(b) shows the band contrast images imposed with grain boundaries. The density of high angle boundaries appears to be higher in the weld bead compare to the HAZ. Fig. 4.5(c) shows coarse directionally solidified grains entering into the weld bead. It shows the presence of allitriomorphs ferrite grains. This particular morphology may be attributed to a rapid solidification rate and is a result of the lower ambient temperature of the base metal at the initial states of welding process. This observation suggest that the heat inputs during welding and water jet dilution after welding have a synergistic effect on the grain size and morphology. Thus, we observe such contrasting microstructural features.

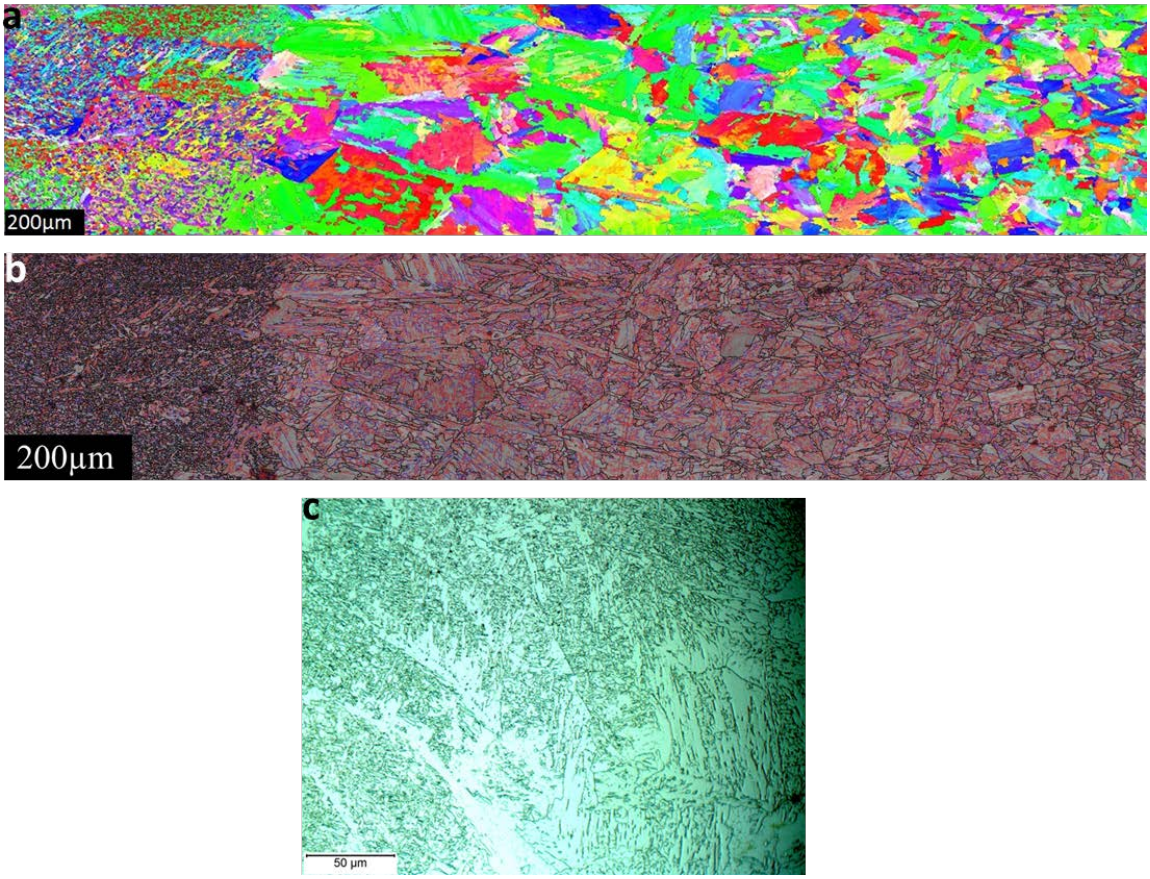

Fig. 4.5. (a) EBSD scan map (b) image quality with imposed grain boundaries and (c) optical micrograph showing weld metal/HAZ interface.

4.1.1. Microstructural changes across weld depth

Fig. 4.6 (a-d) demonstrates the microstructure of different points corresponding to point C, D, E and F (see Fig. 4.1) within the cross section of the weldment. One can see that Fig. 4.6(a) comprises mainly of fine acicular ferrite and there is no evidence of grain boundary phases. Fig. 4.6(b) comprises of mainly acicular ferrites and shows the presence of grain boundary phase such as proeutectoid. The microstructure in fig. 4.6(c) indicates an increase in the grain boundary ferrite phase. Fig. 4.6(d) is consist of mainly acicular ferrite grain boundary phase (i.e. proeutectoid and widmanstattten ferrites). The volume fraction of the ferrite phase appear to be higher compare to the other points (C, D and D (Fig. 4.1)) in the weld depth. The structure observed at the points C, D, E and F corresponding to Fig. 4.6(a-d) could be ascribed to the slower cooling rate of the weld at the centre compared to that on the surface. The slower cooling rate allow grain coalescence and grain growth that ultimately can coarsen the microstructure.

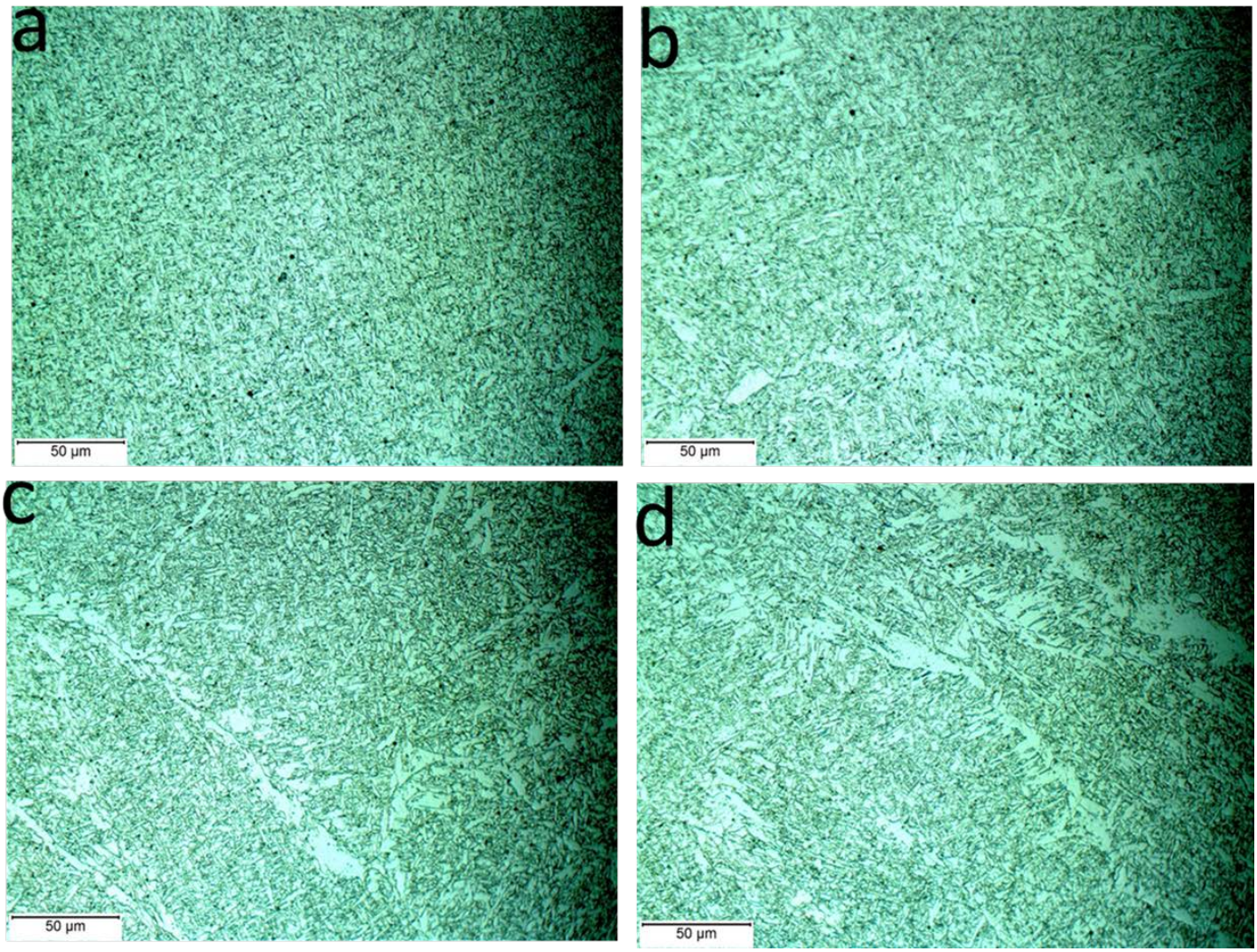

Fig. 4.6. Optical micrographs showing variation in microstructure in the weld cross section at (a) 2 mm (b) 4 mm (c) 6 mm (d) 8 mm from weld top surface.

Fig. 4.7 show the EBSD map and image quality images of the cross section of the weld corresponding to point D, E and F (see Fig. 4.1). One observes that the microstructure is finer at the surface of the weld compared to the points towards the center. Fig.4.7 (a), (b) and (c) show the EBSD orientations maps of the weld. One can see that the larger grains formed at the mid-weld are similar in orientation to the surrounding microstructure, and are located next to the original austenite grain boundaries. This similarity in the orientation indicates that after the austenite to ferrite transition and formation of the acicular ferrite microstructure, the larger grains may have

been formed by coalescence of smaller ones followed by grain growth during the slow cooling of the mid-weld microstructure. The cooling rate was fast for the microstructure next to the surface, thus there was not enough time for grain coarsening. In comparison, the intensity of the interlocking features increases with depth of weld. Throughout the weld, each ferrites packets are predominantly of certain crystallographic orientation. From the observation, we can see that the top exhibited a seemingly more equiaxed microstructure with less chaotic arrangement of the plates compare to the other areas located at some depth in the depth of the weld. This may be related to the cooling gradient in the solidification process as well as the role of inclusions in ferrites nucleation. It is generally expected that the cooling rate is higher at the top surface compared to the middle of the weld, and thus could have resulted in the microstructural variation between these points (D, E and F) [82, 96]. Fig.4.7 (d), (e) and (f) show the image quality map with grain boundaries of the weld. As seen, the weld cross section is composed predominantly of high angle grain boundaries. Possible reason for this development will be explained in the following section. However, it is well known that high angle grain boundaries provide resistance to crack propagation.

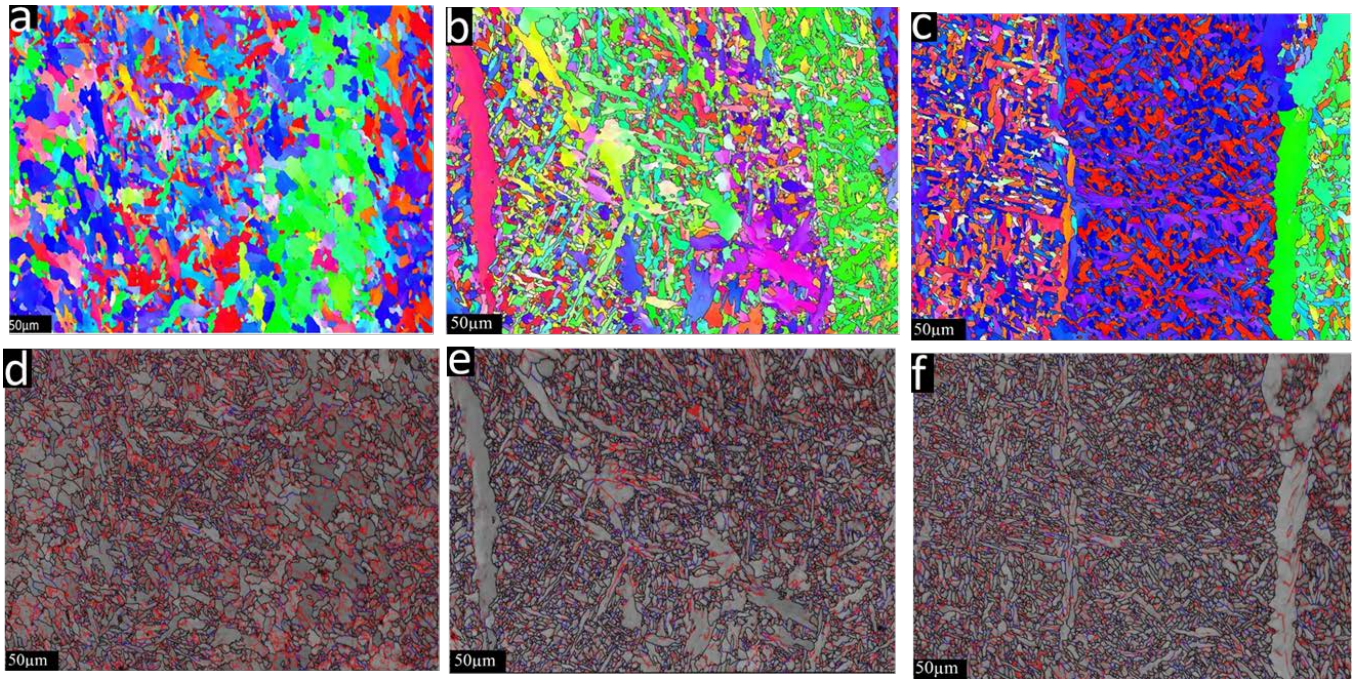

Fig. 4.7. EBSD scan maps and image quality with imposed grain boundaries of weld metal cross section at 4 mm (a and c), 6 mm (b and e) and 8 mm (c and f).

4.1.2. Grain boundary statistics

In order to examine the crystallographic features of AF shown in the Fig. 4.8(a) and 4.8(b), grain boundary statistics was evaluated. Figure 4.8 shows the schematic of the weld indicating the different areas where measurement was taken and grain boundary distribution obtained from EBSD analysis at these three different areas. Figure 4.8(b) shows a homogenous distribution of both low and high angle boundary. This observation is consistent with the microstructure observed in Fig. 4.2 and may be related to some thermomechanically controlled processing (TMCP) used during steel manufacturing. Fig. 4.8(c) represent the grain boundary misorientation of the top surface of the weld. We can see a complete absence of misorientation boundaries in the range of 20 to 47 º. This typical crystallographic characteristics of acicular ferrites has been found to be related to the character of the austenite-to-AF transformation having the Kurdjumov-Sachs (K-S) and Nishiyama-Wasserman (N-W) orientation relationships [176, 183, 184]. This observation

further reinforces the assertion that the acicular microstructure shown in Figure 3(a) represents a packet structure containing submicron grains. Figure 4.8(d) describes the distribution of grain boundaries in the weld metal cross section. It can be clearly seen that the cross section also exhibit absence of misorientation across boundaries in the range of 20 to 47 º. From the grain boundary character distribution on the top surface and on the cross section (points B and C Fig. 4.8), it may be concluded that the grain boundary distribution in the weld is bimodal and boundaries of the acicular ferrites are mostly high-angle boundaries with misorientations greater than 47 º.

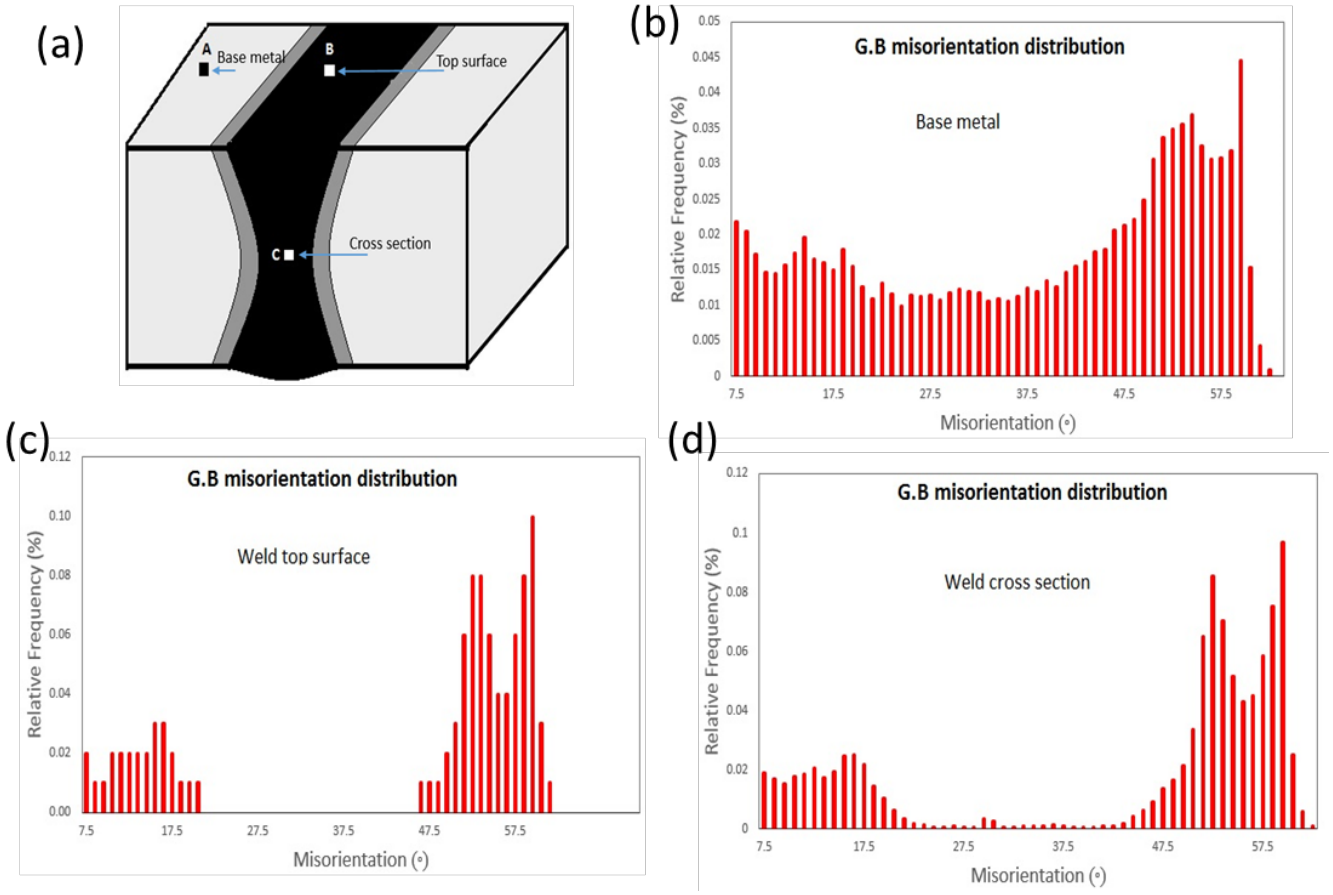

Fig. 4.8. Grain boundary distribution at (a) base metal (b) top weld surface and (c) weld metal cross section.

4.1.3. Kernel misorientation

The average kernel misorientation (KAM) represent the average misorientation of each measurement point with respect to all eight (as in a square grid) neighbors (kernel) within a grain, provided any of these misorientations did not exceed 5°. It is considered as a measure of dislocation density and used is to correlate plastic deformation to misorientation within microstructure [185]. Figure 4.9 shows the kernel misorientation distribution obtained from the EBSD analysis at three different areas (Fig. 4.8(a)). Figure 4.9(a) represent the misorientation distribution for the base metal (points A Fig. 4.8(a)). The misorientation in the base metal is maximum at 0.2°. Figure 4.9(b) shows the misorientation distribution obtained from the top surface of the weld. It shows that misorientation is maximum at 0.5°. Figure 4.9(c) clearly shows a significant difference in the misorientation distribution in the weld metal cross section. It is maximum at 1° and reaches almost up to 4°. Generally deformed grains have higher dislocation densities and higher local misorientations within grains; as a result, the internal grain structure has uniform distribution of dislocation with the building up of a dislocation microstructure (186, 187). Thus, analyses of KAM in the three region shows that the amount of residual strain is higher within the WM cross section. Therefore, it can be concluded that dislocation density is higher in this region compared to the base metal.

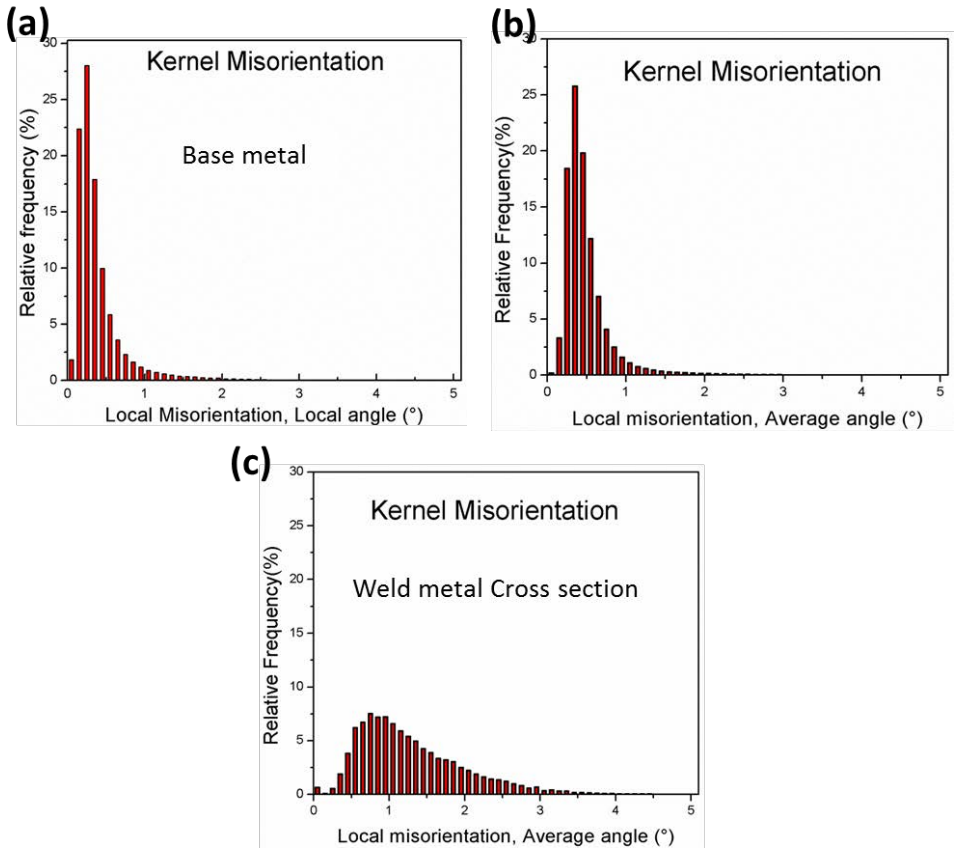

Fig. 4.9. Average kernel misorientation distribution at (a) base metal (b) top weld surface and (c) weld metal cross section.

4.1.4. Recrystallization fraction

The effect of welding on recrystallization is shown in figure 4.10. Figure 4.10(a), 4.10(b) and 4.10(c) shows the recrystallization fraction obtained from the EBSD analysis from the base metal, top surface of the weld and WM cross section respectively (Fig. 4.8(a)). The red and yellow marks level of stored energy due to accumulation of dislocation. Therefore difference in stored energy in materials are related to different fractions of recrystallization. Figure 4.10(a) shows that both recrystallization and recovery was predominant in most of the ferrite grains within the base metal This may be due to the thermomechanical processing (TCMP) of the base metal followed by annealing process which allows release of stored energy thereby higher fraction of recrystallization grains. A retention of some deformation structure can also be seen in Figure 4.10(a). The map

illustrate that some of these grains were deformed during hot rolling and full recrystallization was not possible [188]. Figure 4.10(b) shows some fraction of recrystallized material, however, it also shows that recovery took place during the process. The recrystallization experienced here may have happened due to remelting and solidification of the weld pool followed by the annealing process that was carried out to reduce the impact of the welding residual stress. It is therefore necessary to investigate the nature of residual stress developed in the top surface of the weld as well as at the cross section in other to fully understand the synergistic effect of welding and post weld heat treatment on the microstructure. Figure 4.10(c) indicates that deformed structure is found mostly in the mid weld cross section compare to the top surface of the WM and BM. This is an indication that the mid weld cross section has the largest stored energy and highest dislocation density. This observation can be related to cooling gradient and the impact of welding residual stresses between the different areas in the WM.

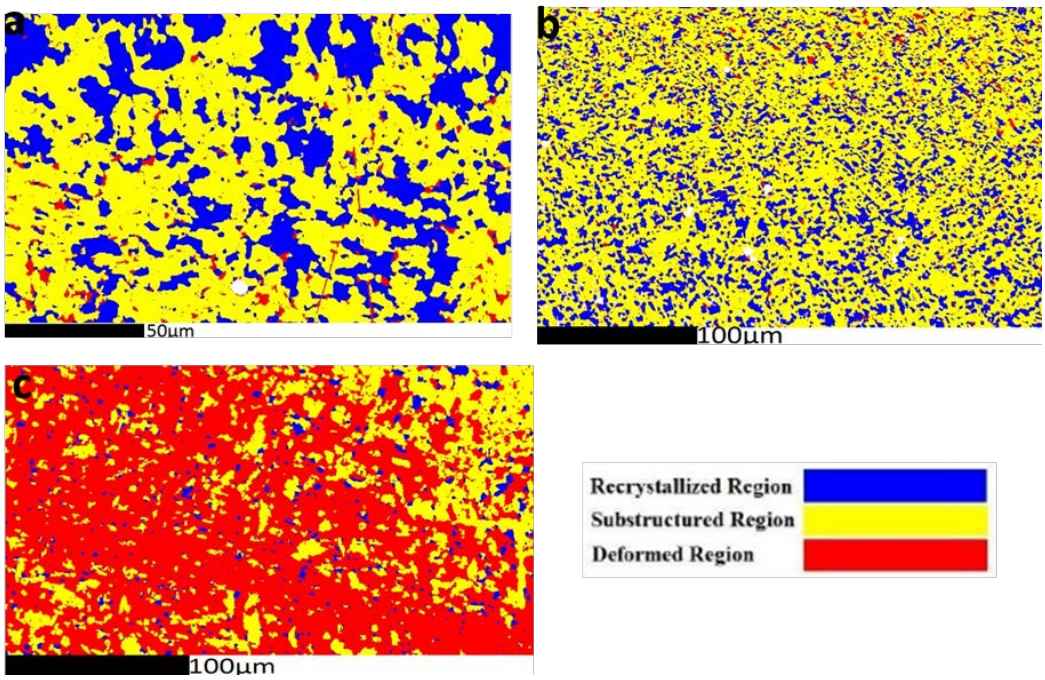

Fig. 4.10. EBSD recrystallization fraction map at the (a) Base metal (b) weld top surface and (c) weld center cross sections.

4.1.5. Void distribution

It is well known that the welding procedure used has an impact on density of porosity developed within the weld. And this porosity affect the mechanical property of the weld since they are able to act as crack initiation sites. Fig. 4.11 (a-b) shows the porosity distribution measured at 2mm interval within the weld metal cross section (Fig. 4.1). The voids are categorised into fine and coarse. Fig. 4.11(a) represent the fine void distribution. We can see that the density of fine voids is higher at the top surface and decreases with depth of the weld metal. Fig. 4.11(b) represent the coarse void distribution. It can be seen that the density of coarse void observed also decreases with depth of the weld metal. In comparison, the average volume fraction of fine void at each point is significantly higher compared to the coarse void. This implies that following solidification of the weld bead, significant volume fraction of small voids is developed which cannot be observed at a magnification of X500. This observation is in good agreement with the work of Pessoa [189] who observed that in multipass wet welds, the porosity distribution reduced along the weld depth when the individual weld beads were laid in the some direction. This changes in porosity distribution along the weld has been closely linked to the type of welding consumables used and the presence of hydrogen gas bubbles that become trapped during solidification of the weld metal [189, 190]. From observation, it may be concluded that the volume fraction of fine voids observed were higher compared to the coarse voids.

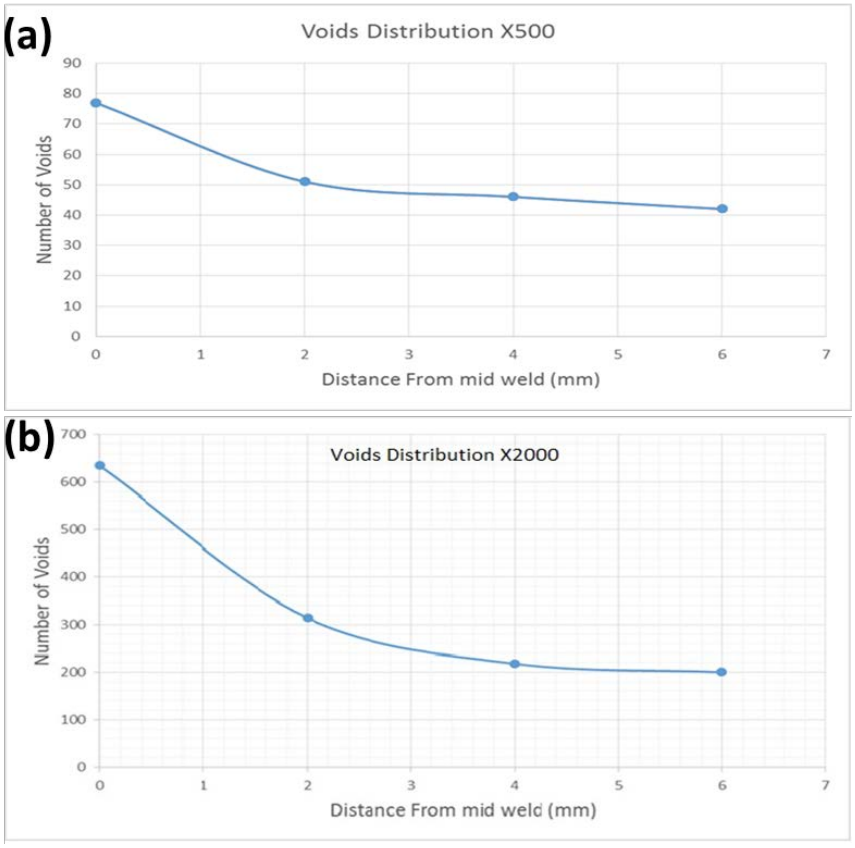

Fig. 4.11. Void distribution at (a) X500 magnification and (b) X2000 magnification weld cross section.

4.2. TEM analysis

TEM was used to investigate AF development in two different areas of the steel as shown in Fig. 4.12. In order to understand the effect of welding heat on the microstructure of the HAZ region, TEM analysis was also carried out at this region. All our observations relate to the AF microstructure, inclusion characteristics and the HAZ.

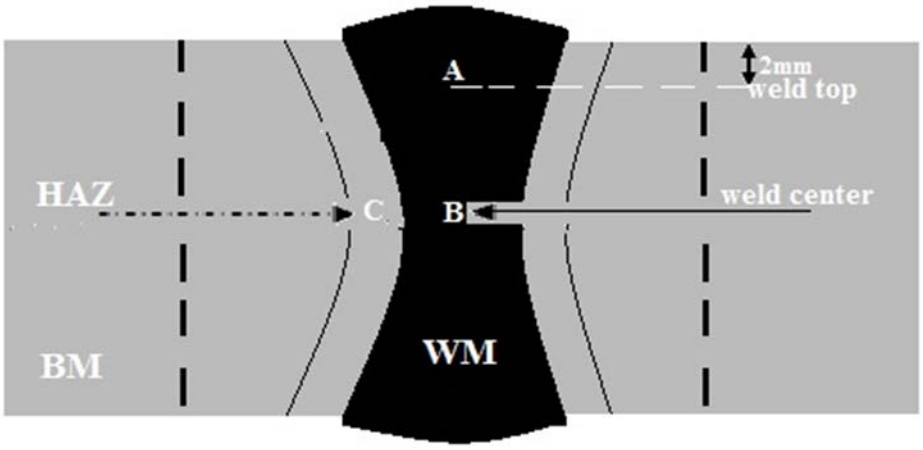

Fig. 4.12. Schematic of the weldment cross-section indicating three subzones used for TEM investigation.

4.2.1. Analysis of weld top

A typical microstructure of acicular ferrite observed under TEM is shown in Fig. 4.13. Fig. 4.13(a-b) is the bright and dark film image of the weld top indicated as A (Fig. 4.12). As shown in this figure, the characteristic Inter-locking features of the acicular ferrite can be confirmed. Microstructure consists of ferrites lath or plates irregular in it shape and aligned in arbitrary directions. A close examination of the individual lath in the micrograph, shows that the individual lath contains a relatively high density of dislocations and fine precipitate at the boundaries.

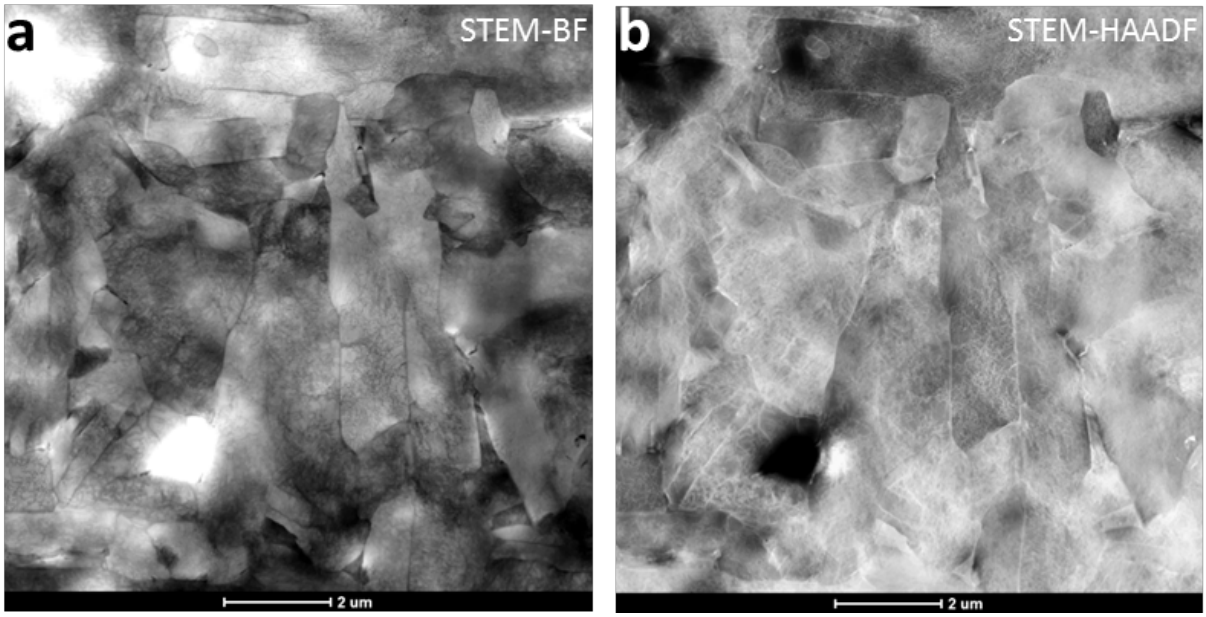

Fig. 4.13. (a) bright and (b)dark film TEM micrograph of acicular ferrite microstructure in the top weld metal.

It is well known that acicular ferrite is nucleated at inclusions. Fig. 4.14(a-b) shows the presence of inclusion within the weld microstructure. The figures show ferrite nucleating from inclusions. Although not all of the inclusions appear to be related to ferrite nucleation. However, as it was concluded by Lee et al [191] that as the width of ferrite grains increases during ferrite growth, it can sweep through other inclusions on the path of growth, thus such inclusions are consider non-nucleant. Therefore, we may conclude that “sympathetic nucleation” played a dominant role in the development of the interlocking acicular ferrite network observed at the weld top in our present study. And this result is closely in agreement with the works of Ricks [111]. In general, the weld top is predominantly composed of acicular ferrite and fine bainite.

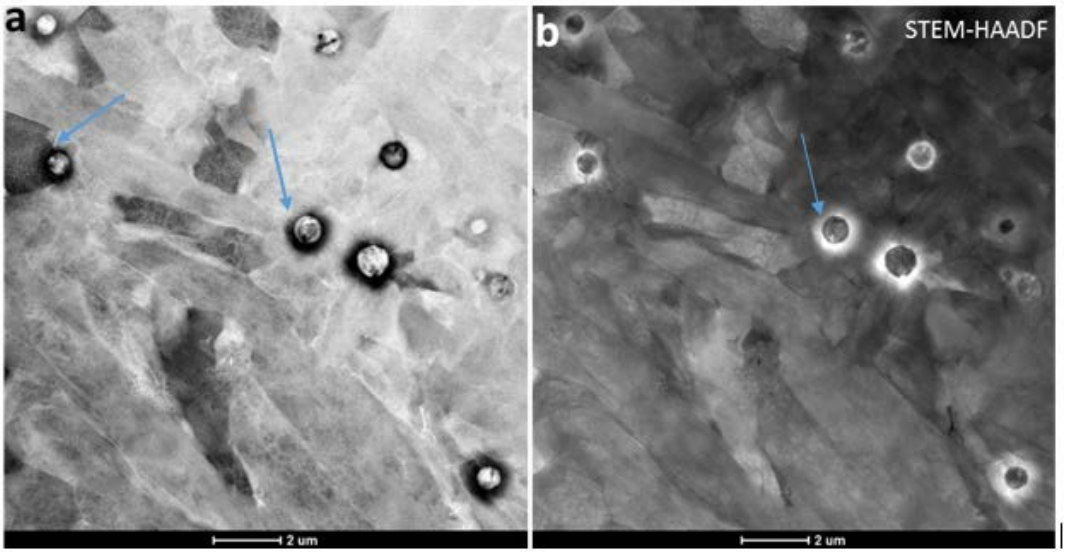

Fig. 4.14. (a) Bright and (b) dark field TEM micrograph showing nucleation of acicular ferrite from inclusion.

4.2.1.1. Inclusion analysis

To understand the type and morphology of the different types of inclusions, TEM images were taken. The inclusion particles were subsequently analyzed using EDS to understand their chemical compositions. Fig. 4.15 show TEM micrograph and the corresponding EDS analysis of inclusion observed in the WM. The size and morphology of an inclusion determines to a great extent its ability to be a ferrite nucleant [96]. The EDS map shows that the major elements present are A1, Si, O, Ti and Mn. This suggests that the present inclusion is a mixture of SiO_2–MnO–Al_2O_3 oxides containing a small amount of titanium [191].

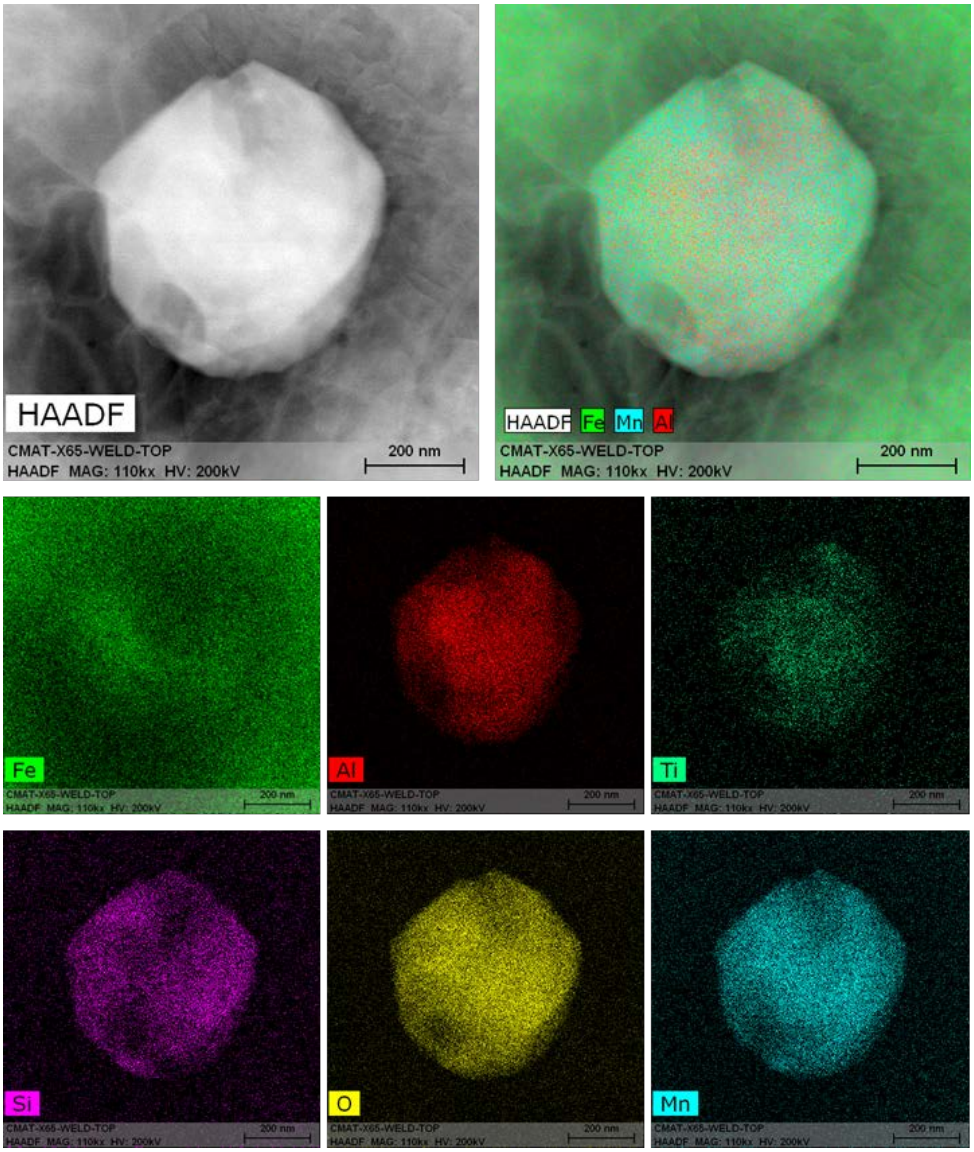

Fig. 4.15. EDS X-ray maps of one of the inclusions in the weld top showing the elemental composition to be Al, Si, Mn, Ti and oxygen.

Fig. 4.16 shows TEM micrograph and the corresponding EDS analysis of the inclusions. Almost all of the inclusions observed were spherical in shape, with a size up to about 2µm. The figure shows that some of the ferrite laths appeared to be fanned outwards from the inclusions, these lath may be considered to be nucleated from these inclusions. The EDS map of the area show that the inclusions varied in sizes and are rich in A1, Si, O, Ti and Mn elements. The figure showed that the relative proportion of the major elements in each inclusion varied slightly but elements are

quite uniformly distributed throughout the inclusions regardless of the size. Therefore, it may be concluded that the major metallic elements combined with oxygen to give single phase oxide like the $MnO–SiO_2–Al_2O_3$. This result is also consistent with the results of other authors [191].

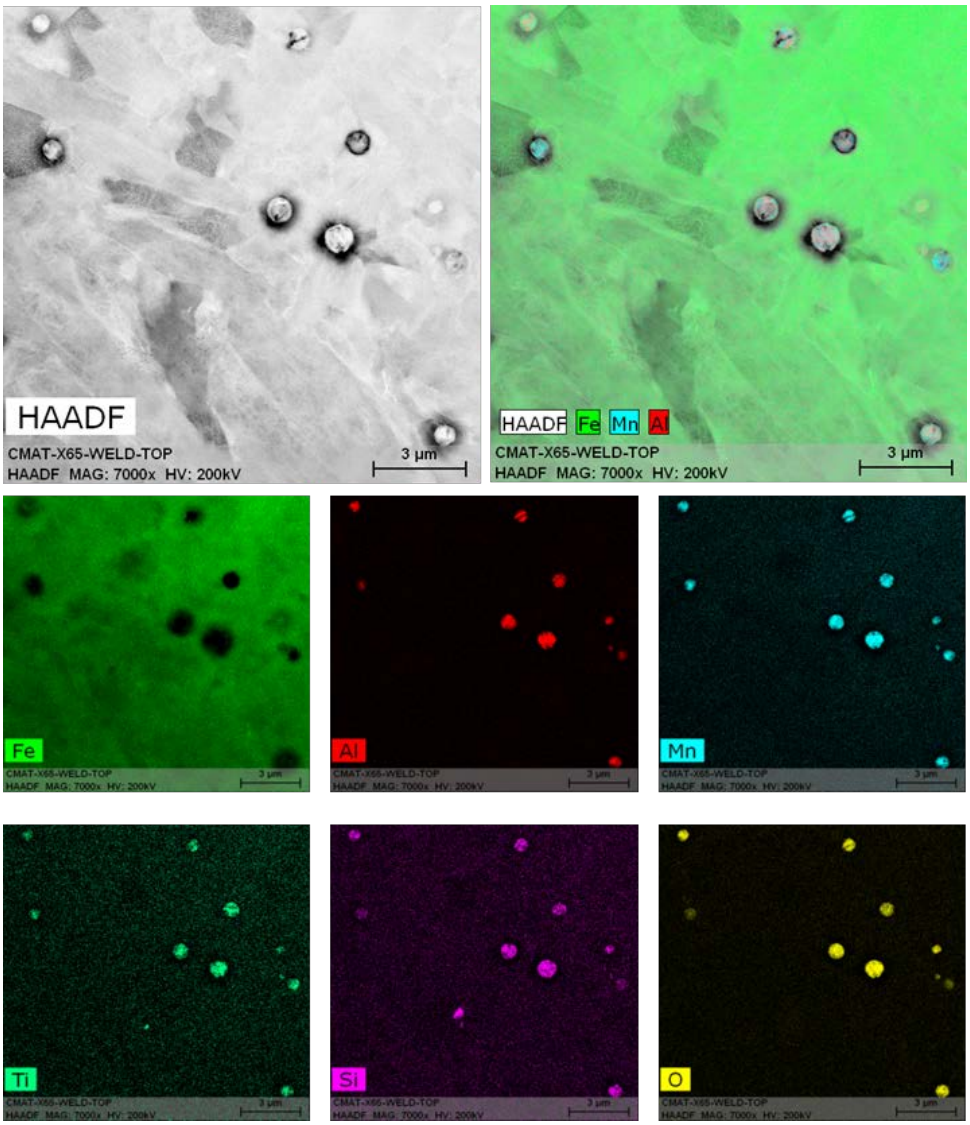

Fig. 4.16. EDS X-ray maps of inclusions/particles showing that the type of inclusion was Al-Si-Mn-Ti oxide particles.

EDS analysis was carried out on two regions marked as 1 and 2 as shown in Fig. 4.17. From the figure, The EDS obtained from the WM marked region 2 shows that iron is the predominant element in this region reaching up to approximately 97% W/w. Manganese is also seen in small proportion of about 2%. There is a complete absence of oxygen. The EDS quant obtained from the

inclusion in the region marked 2 shows the presence of Al, O, Si, Ti and Mn. We can see that oxygen is predominant up to 45% in weight percentage while manganese is 21%. Aluminium, silicon and titanium are also found in the inclusions. It has been reported that the chemical composition of inclusions is a primary factor controlling their efficiency as nucleants of acicular ferrite. For example, the inclusions rich in aluminium have been observed to be more favorable in ferrite nucleation than those rich in manganese. However, this seems controversial as other researchers were unable to find any correlation between the amount of acicular ferrite and composition of inclusions [192, 193].

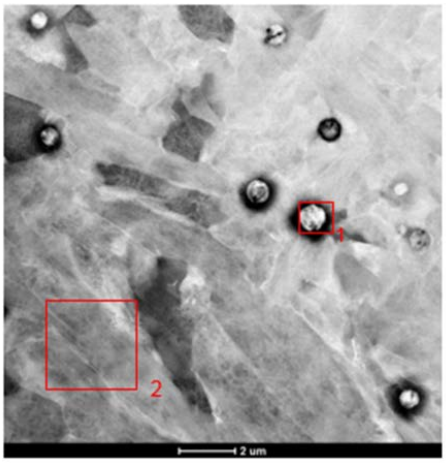

	Element	Weight %	Atomic %
1	O(K)	45.39	67.22
	Mg(K)	0.32	0.31
	Al(K)	14.87	13.06
	Si(K)	4.58	3.87
	S(K)	0.27	0.2
	Cl(K)	0.39	0.26
	Ti(K)	6.92	3.42
	Mn(K)	21.46	9.25
	Fe(K)	5.3	2.25
	Zr(K)	0.45	0.11

	Element	Weight %	Atomic %
2	Si(K)	0.25	0.51
	Mn(K)	2.02	2.04
	Fe(K)	97.19	96.98
	Cu(K)	0.52	0.45

Fig. 4.17. EDS Quantitative analysis of weld metal and inclusion.

4.2.2. Analysis of weld center

A typical microstructure of acicular ferrite observed under TEM in the weld center (point B Fig. 4.12) is shown in Fig. 4.18(a-b). It can be seen that the acicular ferrite laths or plates are shorter in length and more chaotic in it arrangement. They are also marked by the presence of high density of dislocations, which was noted to be significantly higher than at the weld top (Fig. 4.13(a-b). In this micrograph, one can see three inclusions surrounded by a number of ferrite laths emanating from the inclusions. It appears that there are more inclusions available for ferrite nucleation in the weld center compare to the weld top. Hence, we can conclude that higher number of inclusions is

partly responsible for the short and chaotic arrangement of the ferrite lath observed in the weld center compare to the weld top.

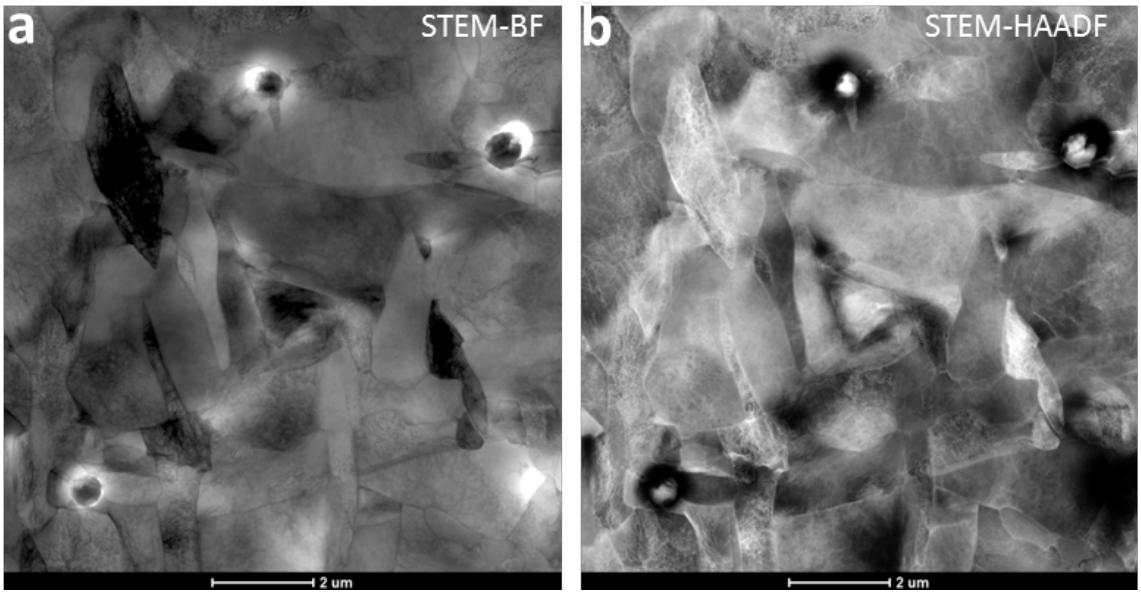

Fig. 4.18. (a) Bright and (b) dark film TEM micrograph of acicular ferrite structure in weld center showing high dislocation density.

4.2.2.1. Weld center inclusions

Inclusions within the weld center also varied in size. Fig. 4.19 shows the EDS map of the inclusions. The inclusions in this region are similar in composition and sizes to that observed at the top weld. From the map, we can see that Al, O, Si, Ti and Mn are the major elements in the inclusion. (Forming a single phase oxide within the $MnO–SiO_2–Al_2O_3$ system).

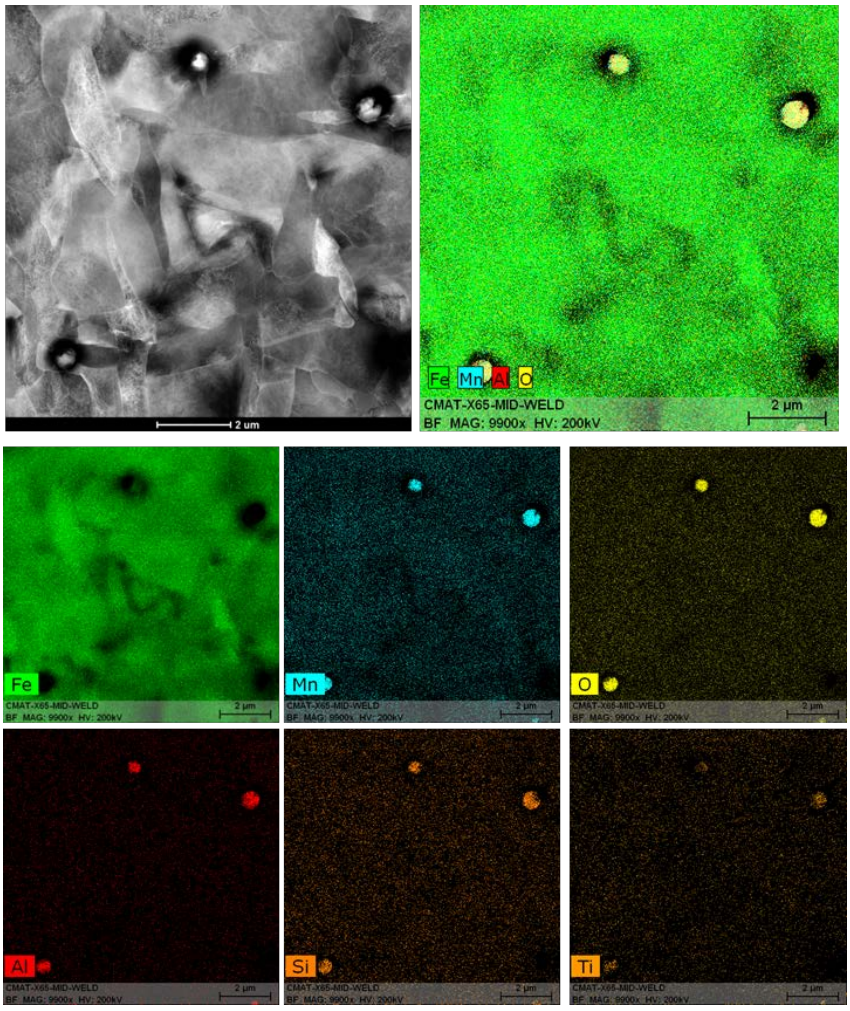

Fig. 4.19 EDS X-ray maps of different inclusions at weld center showing that the type of inclusion was Al-Si-Mn-Ti oxide particles.

4.2.3 Heat affected zone (HAZ)

Bright and dark film TEM micrographs of HAZ are presented in Fig. 4.20(a)-(d). Fig. (a) and (b) show the morphology of ferrites in the HAZ. The microstructure around the HAZ region show that grain have different sizes and morphology depending on their distance from the fusion zone.

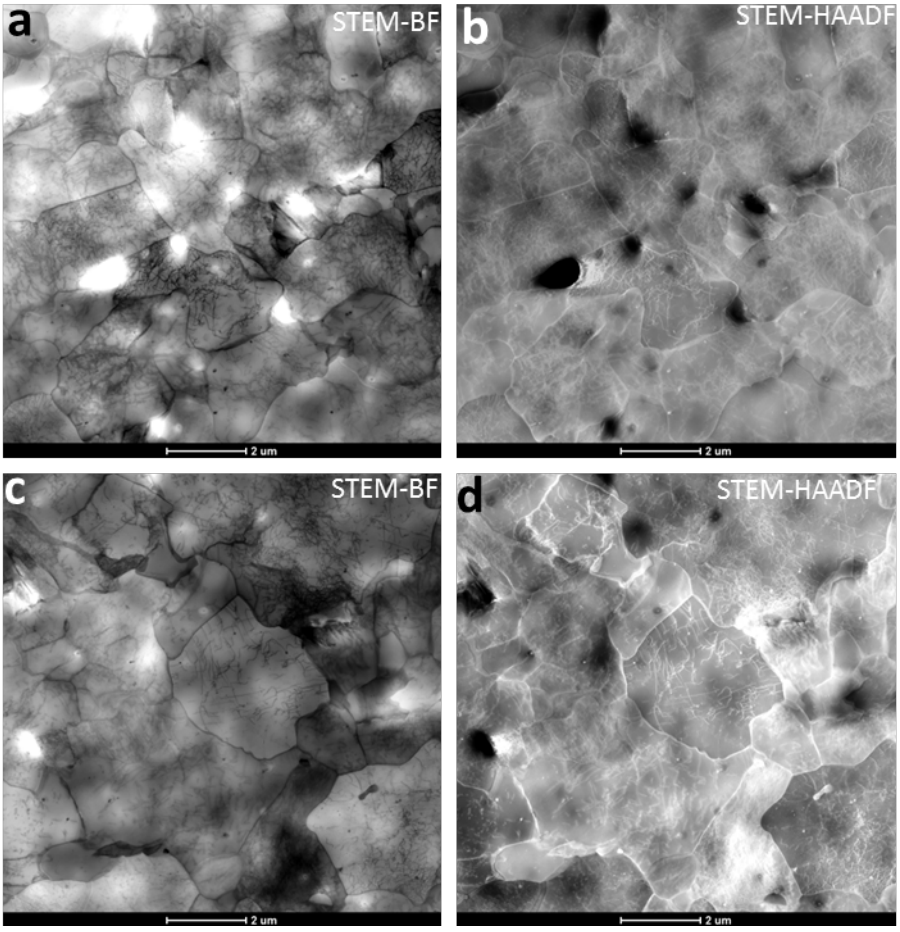

Fig. 4.20. (a), (c) bright and (b), (d) dark film TEM micrograph of different points in the heat affected zone showing general grain.

Figure 4:21(a-b) represents the bright and dark field image of the HAZ. It shows that the ferrite microstructure in the HAZ is coarse-grained ferrite with small M/A and contain high density of dislocations. Figure 4.22(a-b) shows a close examination of the individual ferrite. It can be seen that the individual ferrite contains a relatively high density of dislocations and contain some martensite at the inter ferrite lath boundaries, observed as a darker phase.

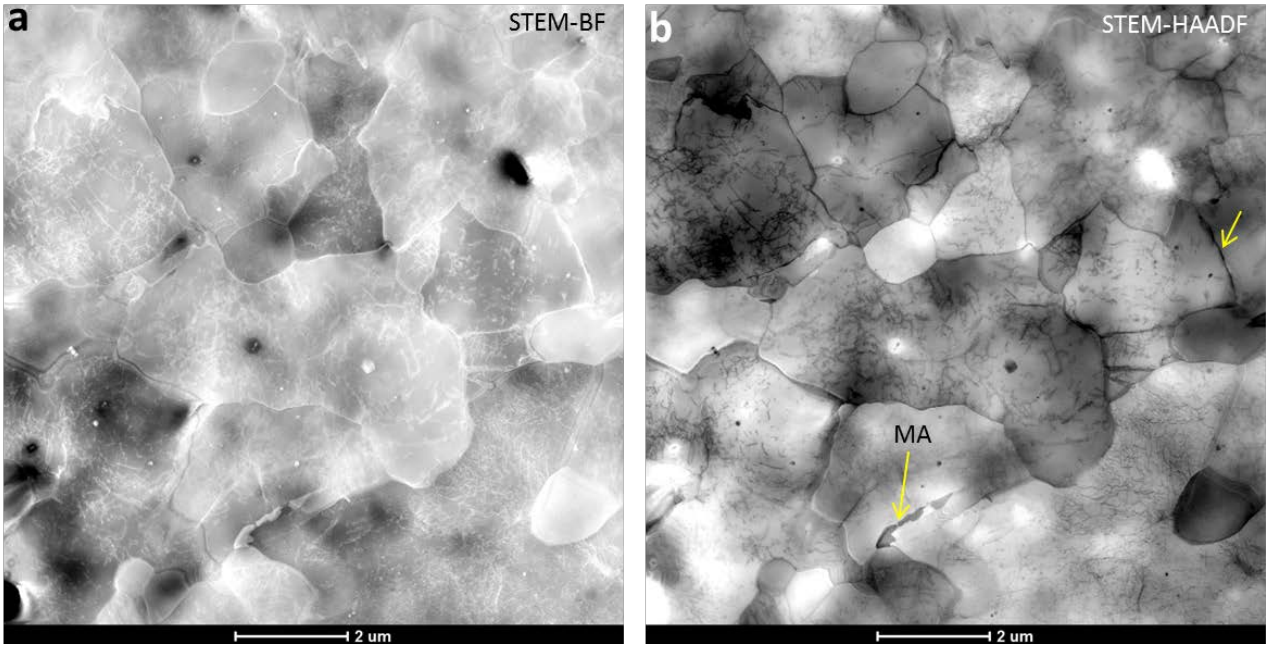

Fig. 4.21. (a) Bright and (b) dark film TEM micrographs of HAZ showing coarse ferrite grains with M/A constituent (indicated by arrows) and high density of dislocations.

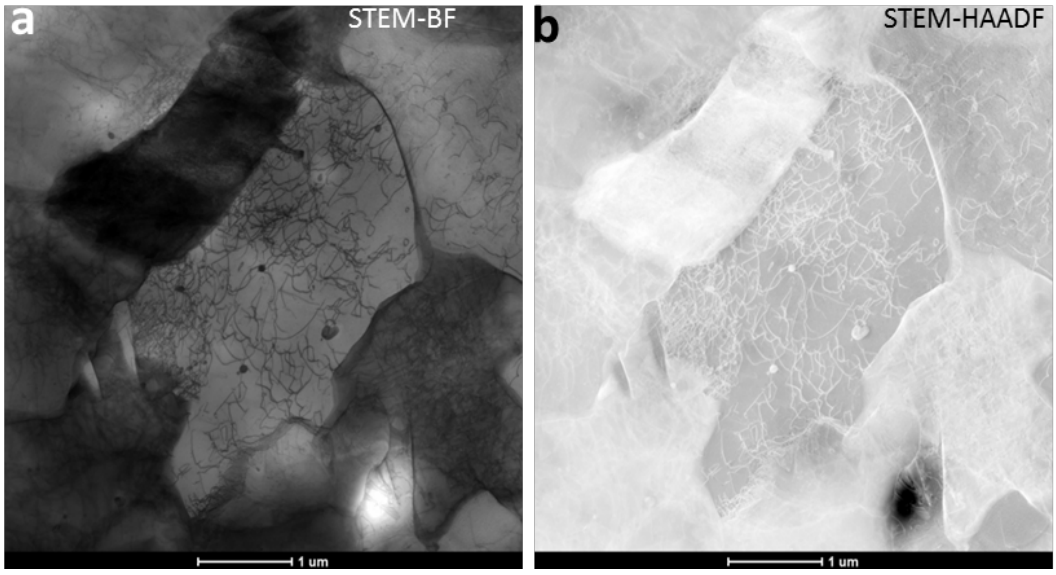

Fig. 4.22. (a) Bright and (b) dark film TEM micrographs of individual ferrite showing martensite at the inter ferrite lath boundaries and dislocation arrangement.

4.2.3.1. Analysis of HAZ inclusions

Figure 4.23 Show TEM-EDS analysis of the inclusion/particles observed in the HAZ region corresponding to point C in figure 4.12. The figure also show the presence of high dislocation density. The EDS chemical analysis of the precipitates, shows that most of the particles are of

mixed composition containing Ti, Nb, C, N elements. In terms of particle size and density, the precipitate in the HAZ region appears to be smaller in size and fewer in number compare to that observed in WM region. Researchers have reported that Ti-Nb carbonitrides particles or oxide inclusions play a key role in grain growth control by pinning the austenite grain boundaries in the HAZ. Partial or complete dissolution of the Ti(Nb)N precipitates could occur during welding at temperature >1200ºC and cause the enrichment of Ti and Nb in the solid solution. However during cooling, the carbonitrides can also reprecipitate at the region adjacent to the fusion line in the ferrite phase which is capable of affecting the toughness of the HAZ microstructure [194, 195].

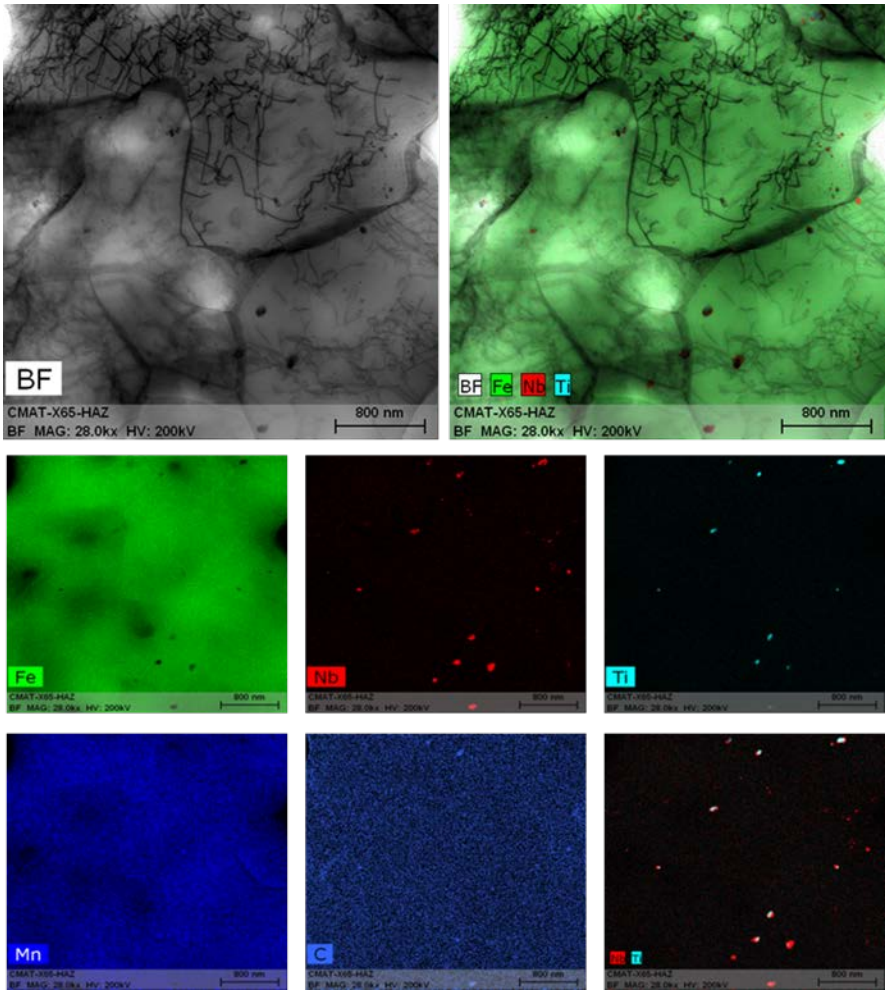

Fig. 4.23. EDS X-ray maps of the inclusions at HAZ showing that the type of inclusion was (Ti,Nb)(C,N).

4.3 Residual stress

Fig. 4.24 (a) and (b) shows the distribution of residual stresses across the top surface of the weld and the cross section of the WM respectively. Fig. 4.24(a) shows that the residual stress distribution on the surface of the weld metal was compressive. It reached about 800 MPa and showed a drastic decrease as one moves from the weld to the base metal. Fig. 4.24(b) shows that the residual stresses at the cross section of the weld were a mixture of compressive and tensile residual stresses such that compressive stresses were observed near the top surfaces, while tensile stresses were observed within the subsurface of the weld cross section. It is generally believed that welding produces tensile residual stress, and therefore require stress relief after the weld process [159, 165, 166] however, the presence of both tensile and compressive stresses have been observed in the past [167, 196]. In this study, compressive residual stresses were observed across the top surface of the weld while a mixture of compressive and tensile stresses were observed within the depth of the weld cross section. This could be due to the difference in cooling rate both at surface and subsurface of the weldment. Since the weld surface cools faster than the subsurface, the hard surface may constrain thermal shrinkage of the surface which could then result in compressive residual stresses on the surface of weld as well as tensile residual stresses at the subsurface of the weld cross section [172].

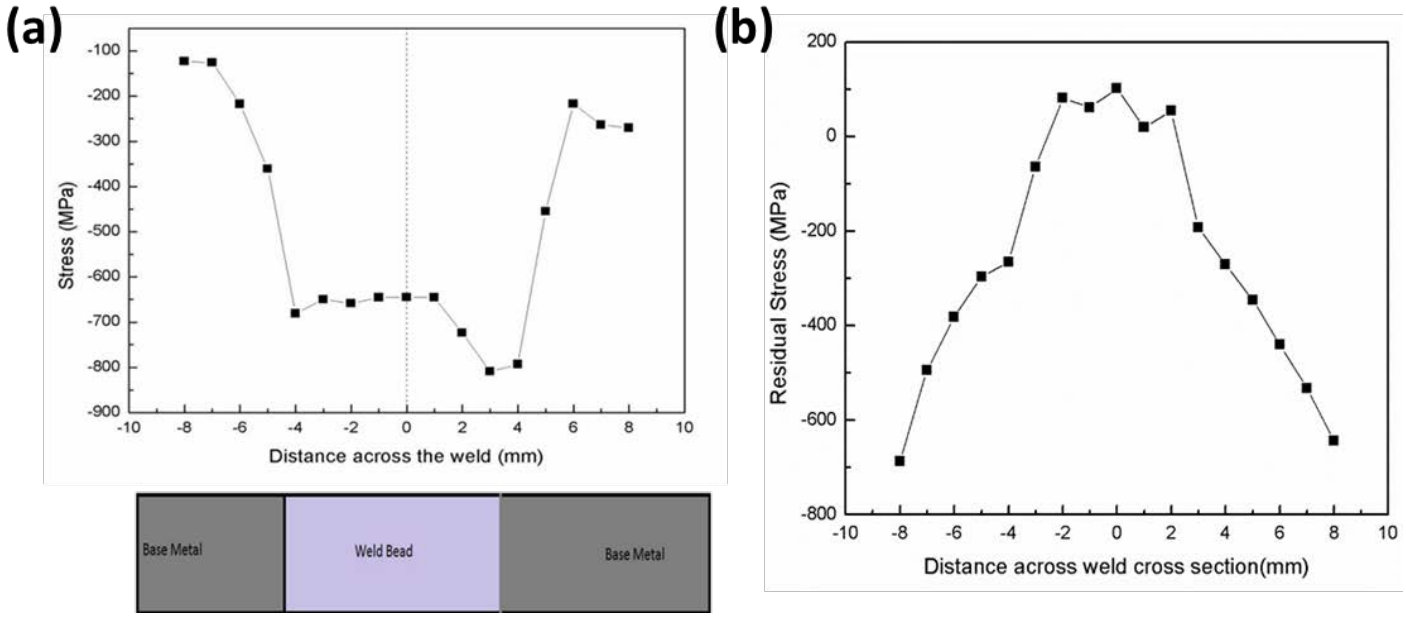

Fig. 4.24. (a) Residual stress distribution at weld top surface (b) residual stress distribution at weld metal cross section.

4.4 Mechanical properties of weld

4.4.1 Hardness

Fig. 4.25 shows the hardness profile across the weld top surface. From the figure, the WM has a higher hardness value reaching 209Hv compare to HAZ which has an average value of 173HV as well as the base metal with an average value of 187Hv, the variation in the stress across the weld may be attributed to several factors such as residual stresses developed just after welding. From the microstructural point of view, the high hardness in the weld may be attributed to the fine grain size, and the interlocking nature of the ferrite grains [179]. The relationship between hardness and grain size is given in equation (4.2)

$$H = Ho + \frac{K}{\sqrt{d}} \qquad (4.2)$$

H is the hardness, H_O is a material constant, K is the strengthening coefficient and d is the grain size.

From equation (4.2), the hardness changes can be explained. One of the factors contributing to lower hardness in the HAZ zone is high heat input below it melting point and hence retention of heat in this region. The lower hardness in the HAZ might be explained by the intense grain growth in this region resulting from high heat input below it melting point [180, 197]. The results obtained are therefore consistent with the observed microstructure.

There are few studies that reports the relationship of hardness with residual stress. However there are differences in the explanations depending on the materials and the stress states considered [198]. Although there are different parameters that affect hardness such as microstructure and phase composition, it is usually expected that the maxima in hardness should correspond to the maxima of compressive residual stress, since the hardness of the material is also a measure of dislocation density [198]. Therefore the observed hardness profile in the present weld samples do show a direct correlation with the residual stress.

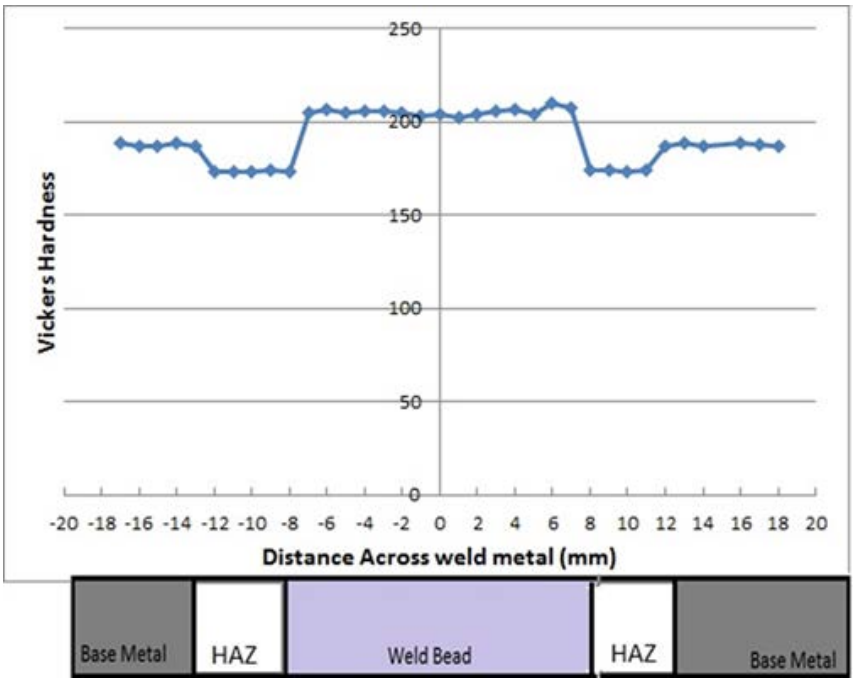

Fig. 4.25. Micro-hardness VHN as a function distance from the center of weld bead.

4.4.2 Hardness map and microstructure

The map provide powerful data that will help understand the variation of hardness across different part of the weld due to microstructural variation caused by welding. Fig. 4.26(a) shows the map macrograph. Fig. 4.26(b) and Fig. 4.26(c) shows the 2D harness map and 3D map respectively. Fig. 4.26(b-c) show significant differences in hardness value across the weld specimen. From the maps, the weld metal shows the highest hardness level. The hardness value of the base metal lies between 200-215 HV. Such high value can be attributed to fine grained microstructure. The hardness level of HAZ ranges between 180 -195HV. It shows a slight difference compared to that of the range for the BM, and is noticeably lower than that of the WM. It is well known that during welding, the HAZ does not experience melting rather, a changed of microstructure due to phase transformation at high temperature transformation of δ-Fe to γ-Fe is followed later by the γ-Fe to α-Fe. From the microstructural variation, it is therefore possible to conclude that this lower hardness level of HAZ compared to the BM hardness is as a result of slight HAZ softening phenomenon [199, 200].

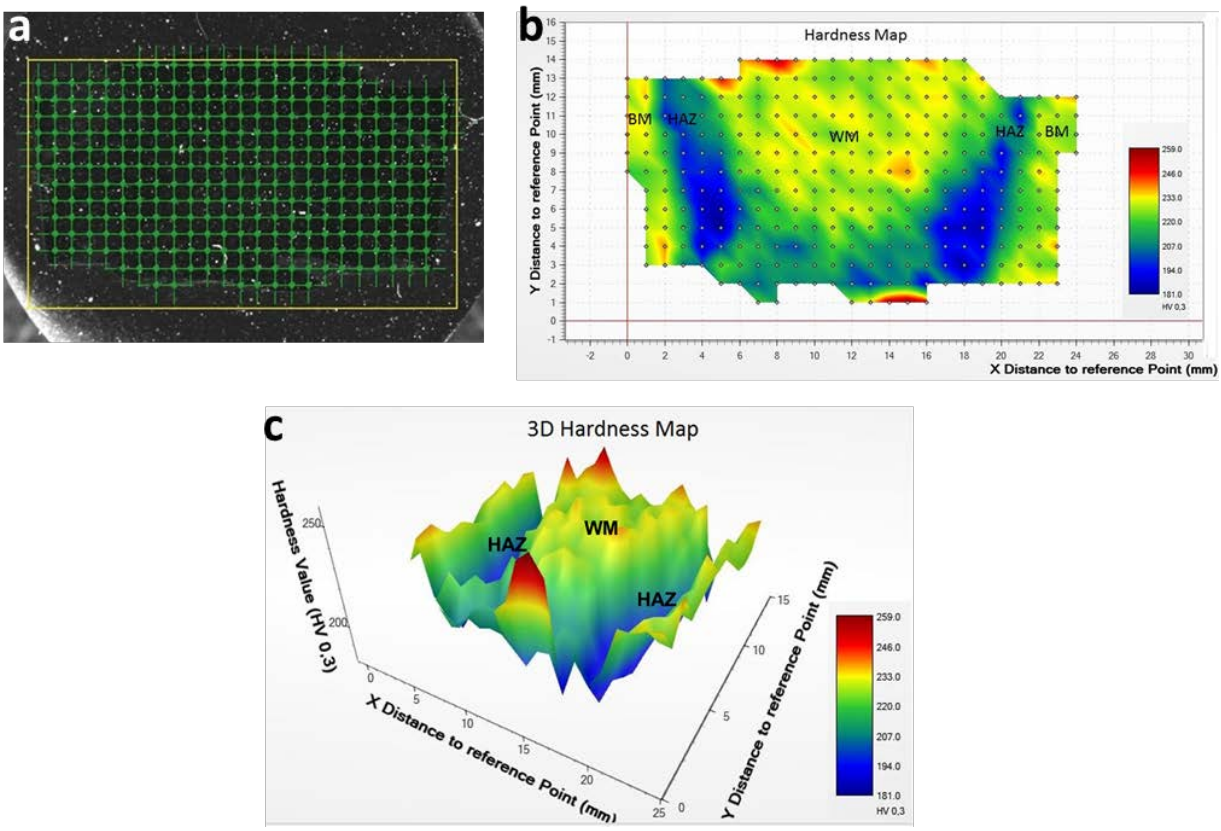

Fig. 4.26. (a) The map macrograph (b) 2D hardness map and (c) 3D hardness map across weld surface.

4.5 X-70 Pipeline weld in hydrogen environment

4.5.1. Characteristics of crack initiation and propagation

4.5.1.1 SEM analysis

Fig. 4.27(a-b) shows clustering of blister and the formation of pitting in the hydrogen tested specimen. The appearance of blisters and pitting on the cross section of the samples and small internal cracks were observed after different charging times. One can see that the pitting appears to be very aligned along weld region close to the heat affected zone. The sizes of the pitting increased with charging time as observed in the interval of 2hr to 24 hour charged specimen. Small

internal cracks were located within the sample around the pit with smaller cracks extending upwards towards the edges of the pits, providing pathways for cracks to connect.

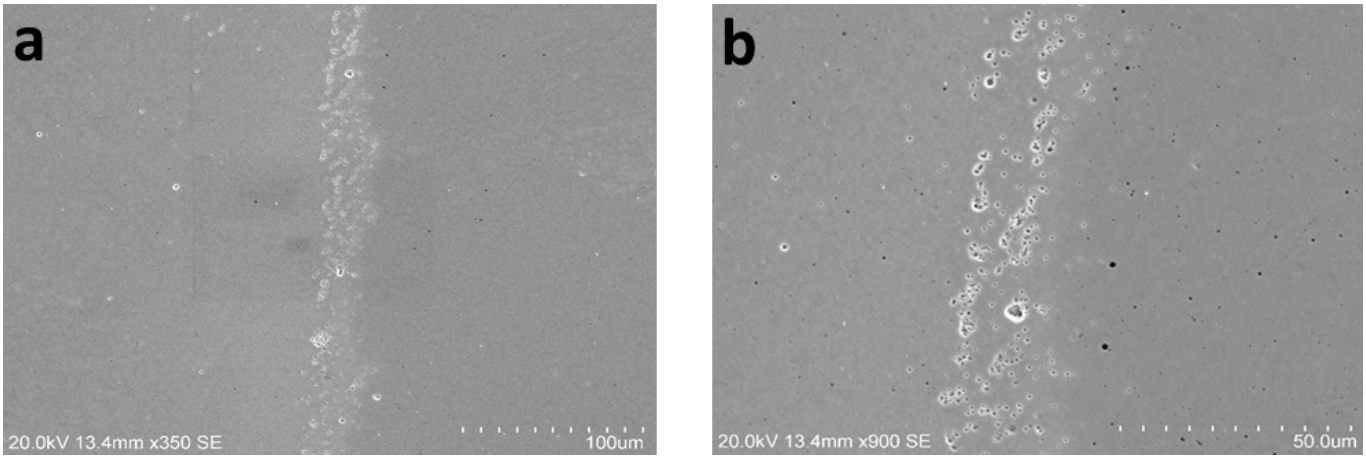

Fig. 4.27. (a) and (b) SEM images showing well aligned localised pitting.

Figure 4.28 show the SEM image of pit initiation from inclusion. Figure 4.28(a) shows the development of three independent pits originating from inclusion. One can see that the initiation and propagation of cracks formed from the pits. These pits coalesce to form small crack that is able to propagate by further coalescence with other neighbouring pit. Figure 4.28(b) shows the coalescence of several pits to form a small continuous crack. It has been well studied that Cracks in HIC can initiate at sites that are related to non-metallic inclusions [126, 201, 202]. Non-metallic inclusions and some forms of surface discontinuity or surface defects are able to accumulate hydrogen which is able to exert significant influence on pits and micro crack initiation. However, the crack propagation has been found to be greatly affected by the overall spatial distribution of the small cracks [203]. Such that spacing between individual neighbouring cracks affects crack interaction and coalescence. The process of crack initiation and the eventual linking of small crack have been proposed in order to provide possible explanation to the mechanism of initiation, coalescence and growth of the cracks [204, 205].

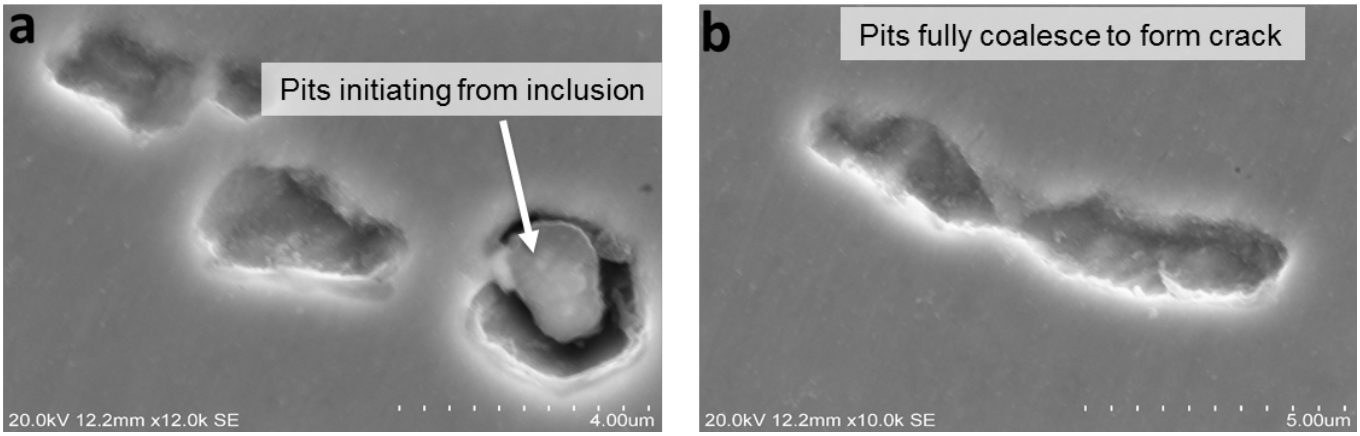

Fig. 4.28 (a) development of pit from inclusion (b) coalescence of pits to form micro-crack.

Figure 4.29(a-b) show typical cases of small propagating cracks initiating from surrounding pits for the 24 hour charged specimen. The direction of the cracks appears to be perpendicular to the polished surface. It well known that HIC cracks can nucleate from non-metallic inclusion and structural defects, However, many cracks did not contain any identifiable inclusions, this may be due to the fact that some of the inclusions may have fallen off during ultrasonic cleaning of specimen or it may well be concluded that some of the initiation sites for pits may have been facilitated by many voids developed due to welding strain and morphology of the ferrite grains.

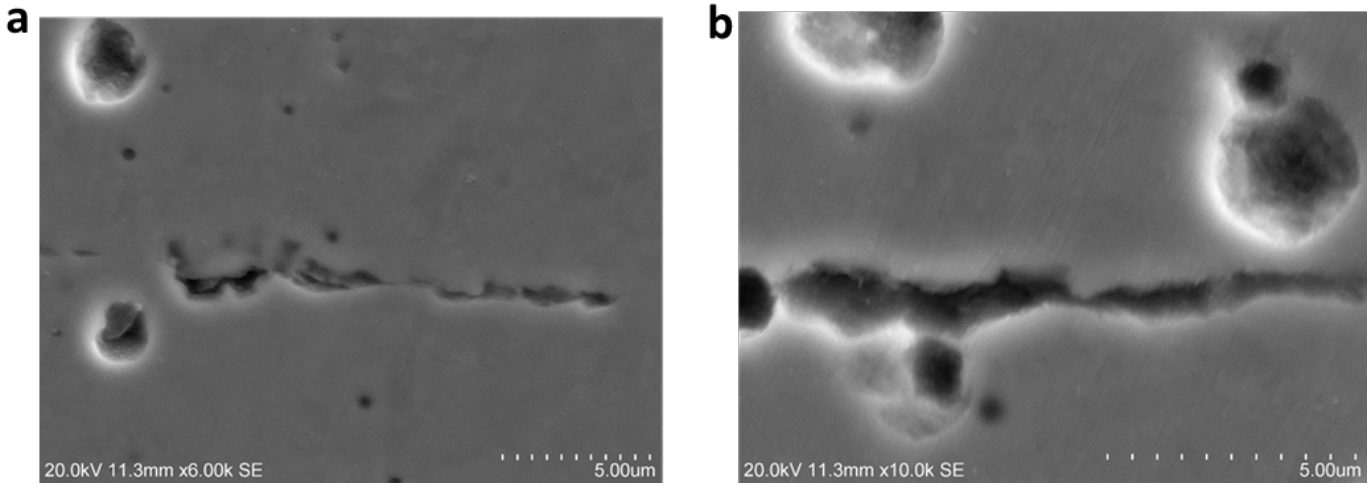

Figure 4.29. SEM images of crack propagation in the 24 hour charged specimen.

4.5.1.2 EBSD investigation on HIC crack region

Figure 4.30(a-b) show the band contrast image with imposed grain boundary angle and EBSD map. In figure 4.30(a) we see that the grains in the WM have high angle grain boundaries while the HAZ have predominantly low angle boundaries. Fig. 4.30(b) show that the grains in the heat affected zone is larger due to welding heat. The weld metal region comprise mainly of acicular ferrite in packets or colonies where each packets have small grains with similar crystallographic orientation. The band contrast image and the EBSD map show that the grains in the region of pitting appears to be elongated in shape. The map shows that the aligned pitting were observed in this region of elongated grain. It is known that grain size, shaped and morphology have influence on hydrogen diffusion and as a result have a pronounced effect on HIC cracks in pipeline steel. We can conclude that the small grain size resulted in many grain boundaries leading to high diffusion of hydrogen. The presence of elongated grains suggest that the localised pitting may have been facilitated by the size and morphology of the grains within this region.

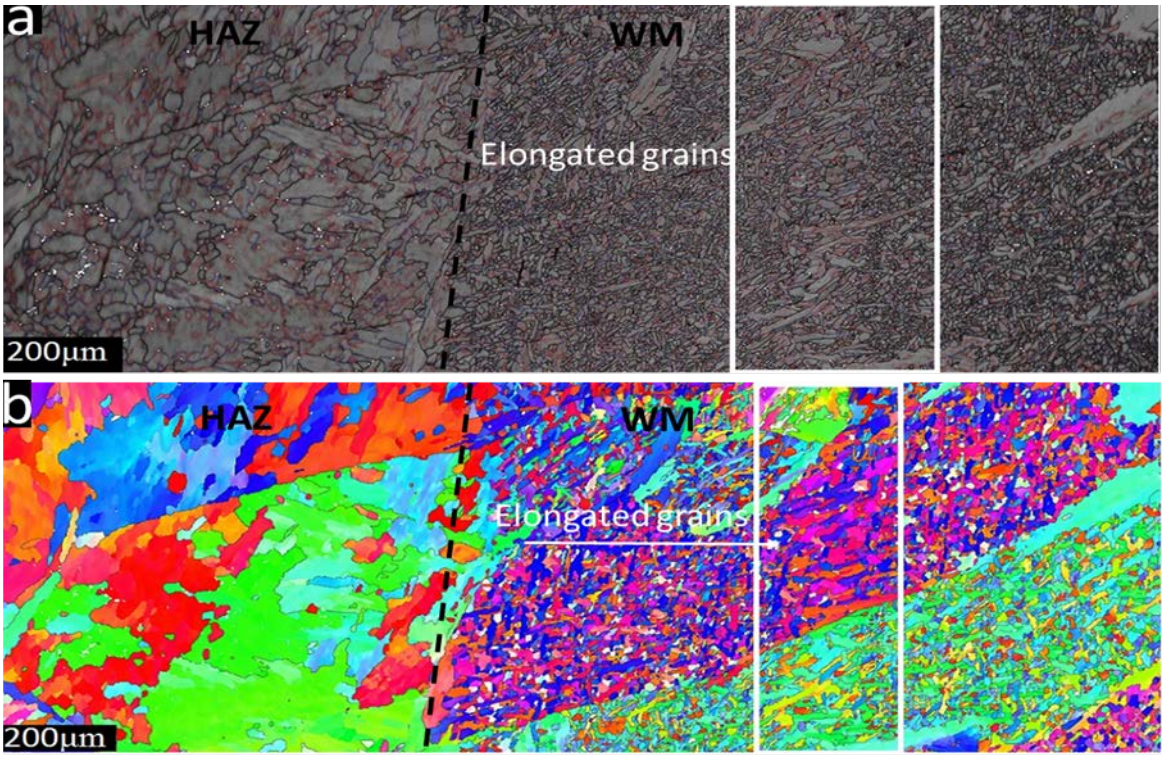

Figure 4.30. (a) band contrast image and (b) EBSD map of pitting region.

Fig. 4.31 shows the kernel average misorientation (KAM) over the region of aligned hydrogen attack in the HIC tested weld specimens. KAM is used to represent the average misorientation between a given point and its nearest neighbors which belongs to the same grain [186]. It is an indirect measure of dislocation density and, as a result, can be used to assess the local plastic strain developed in the pipeline due to welding operation. The map shows an inhomogeneous distribution of dislocation in this region however, it can be seen that the dislocation accumulation is more pronounced in the area of HIC with elongated grain. It is therefore likely the dislocations can increase the HIC susceptibility by trapping of hydrogen atoms at their interfaces with metal matrix. These trappings sites could facilitate crack propagation. The high KAM values in the region of hydrogen attack in the specimen, allows to make a conclusion that the dislocation density is higher in these region. Therefore, we can say that the HIC occurrence has been majorly driven by the

presence of higher dislocation density in this region. This result is consistent with the observations of other researchers [121].

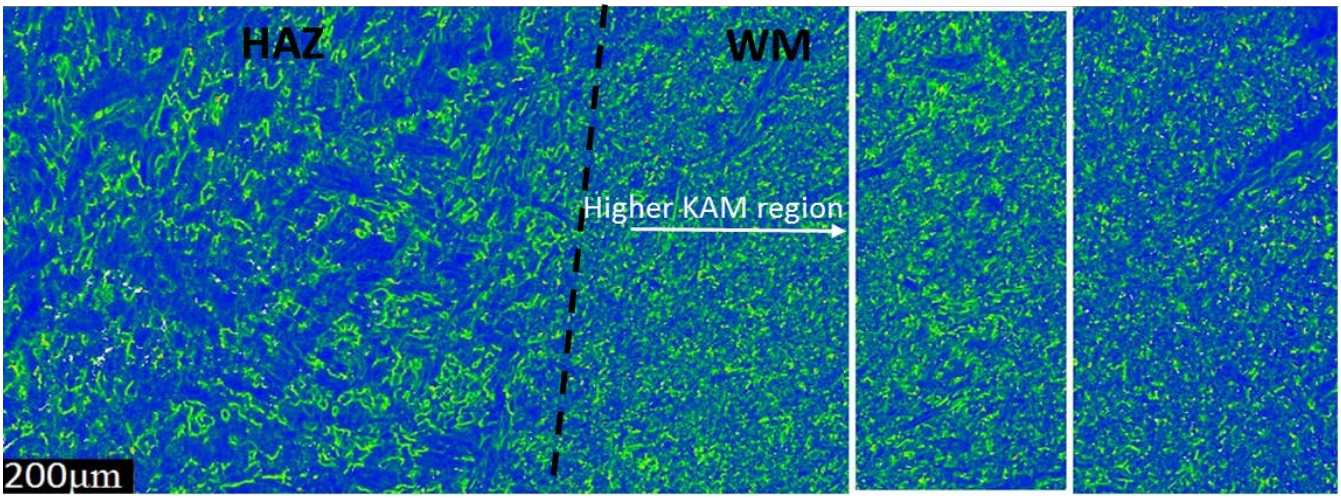

Figure 4.31. Kernel average misorientation (KAM) map of the pitting region.

Fig. 4.32(a)-(b) shows the EBSD and phase map of the EBSD scan on the crack part observed at the HAZ. Fig. 4.31(a) shows that the HIC crack propagation was predominantly transgranular through grains with {123} plane orientation, although few intergranular cracks along boundaries of grains with {110}, {111} and {112} planes were observed. Fig. 4.32(b) show the phase composition map. The BCC phase is marked with blue while red represent FCC phase. It can be clearly seen that the crack propagation path is entirely through the BCC phase. The crack appears to change it path by going around the FCC phase. However, there is no sufficient evident to explain this observation as not much FCC phase was observed in the microstructure in our present study.

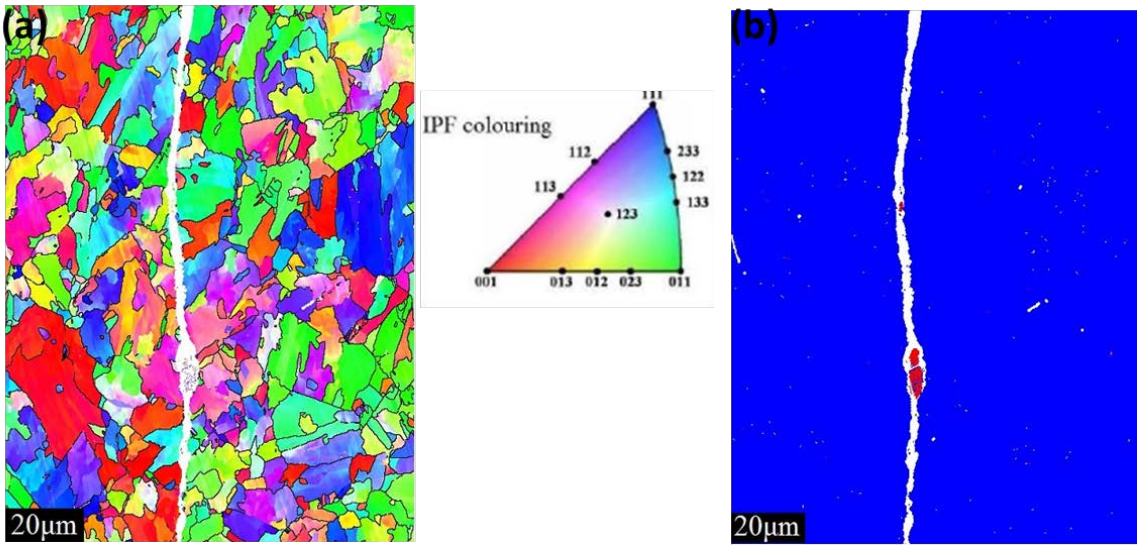

Fig. 4.32. (a) EBSD orientation map and (b) phase maps from the HIC crack in the HAZ.

4.5.2 Effect of hydrogen-charging on stress-strain behavior of the steel welds

4.6.2.1 Tensile experiments

Hydrogen charging produces appreciable changes in local stress, dislocation density and generated HIC cracks. In order to evaluate the effect of these changes on mechanical properties, a tensile test in a direction perpendicular to the weld weas performed. Fig. 4.33 shows the effect of hydrogen-charging on stress-strain behavior of the steel for hydrogen-charged X70 steel. As shown in this figure, there is no difference between curves at lower strains. However, a large difference is observed with the increase of the tensile load. The as received sample showed a considerable level of elongation before fracture while the specimens charged in hydrogen environment fracture way early without considerable elongation. The figure showed that samples charged in the hydrogen environment at different charging times fractured at different strain. From the figure, we can see that the deformation response of the samples charged in hydrogen environment to tensile load reduces with charging time. The 10 hour charged specimen showed the lowest elongation at failure compared to other charging times. Necking of the specimens decreased significantly as charging

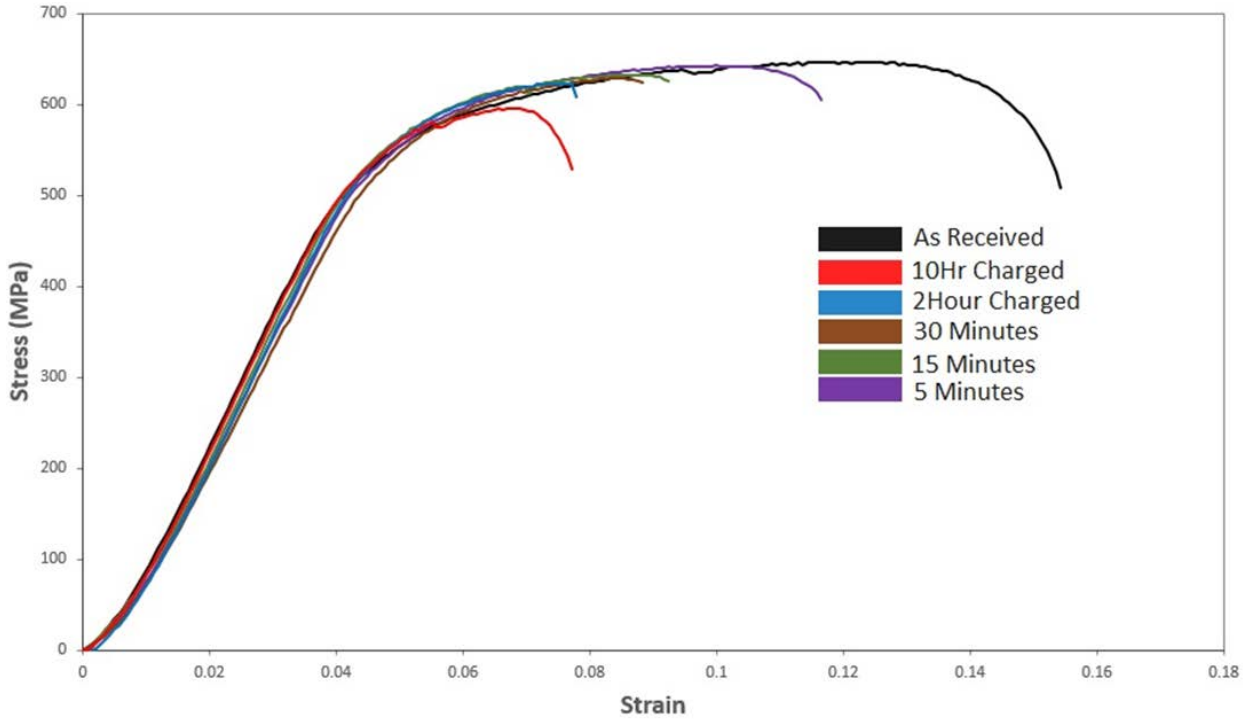

Fig. 4.33. Effect of hydrogen charging time on tensile properties of X70 weld steel.

time increased and no clear evidence of necking was observed in the 2 and 10 hour charged specimen. Based on these results, it is clear that the ductility decreased as charging time increases from 5 minutes to 10 hours. This shows that the X70 steel welds are highly susceptible to hydrogen embrittlement with increasing charging time. This result is in agreement with the work by Don [139]. It is well known that hydrogen atoms diffuse and accumulate at different structural defects such as such as inclusions, dislocations etc., and further aggregation of hydrogen at these sites results in a high internal pressure, resulting in the initiation of local micro-cracks. As demonstrated in this work, the reduction in ductility would be as a result of increase in the concentration of hydrogen with increase in charging time. The accumulated hydrogen atoms lowers the work necessary for initiation of fracture since hydrogen is capable of increasing the rate of local dissolution at the crack tip and this decrease surface of the newly formed planes [206, 207]. Normally the tensile stress facilitates the crack growth by the increase of stress concentration factor at various structural defects.

4.5.2.2 Fractured surfaces

Figs. 4.34(a-f) show the fracture surfaces of X70 steel weld specimens. The fracture surface morphology of the specimen without hydrogen charging was 100% ductile with numerous fine dimples in the fracture surface which is considered a sign of ductile fracture (Fig. 4.34(a)). Moreover, a considerable amount of necking was observed during deformation. After charging for 5 minutes, the fracture surface were still predominantly ductile and shows evidence of dimples. This specimen also show some necking during deformation (Fig. 4.33(b)). Fig. 4.34(c) shows the fracture surface for the 15 minutes hydrogen charged specimen. It shows the presence of dimples, however fine dimples are not observed as in previous images. After 30 minutes charging, the fractured surface shows mixed rupture (Fig. 4.34(d)), indicating areas of ductile and brittle rupture. The 2 hour charged specimen shows that the characteristics of failure was completely brittle. (Fig. 4.34(e)). Fig. 4.34(f) shows the fracture surface of the 10 hour charged specimen. It also shows a completely brittle transgranular fracture.

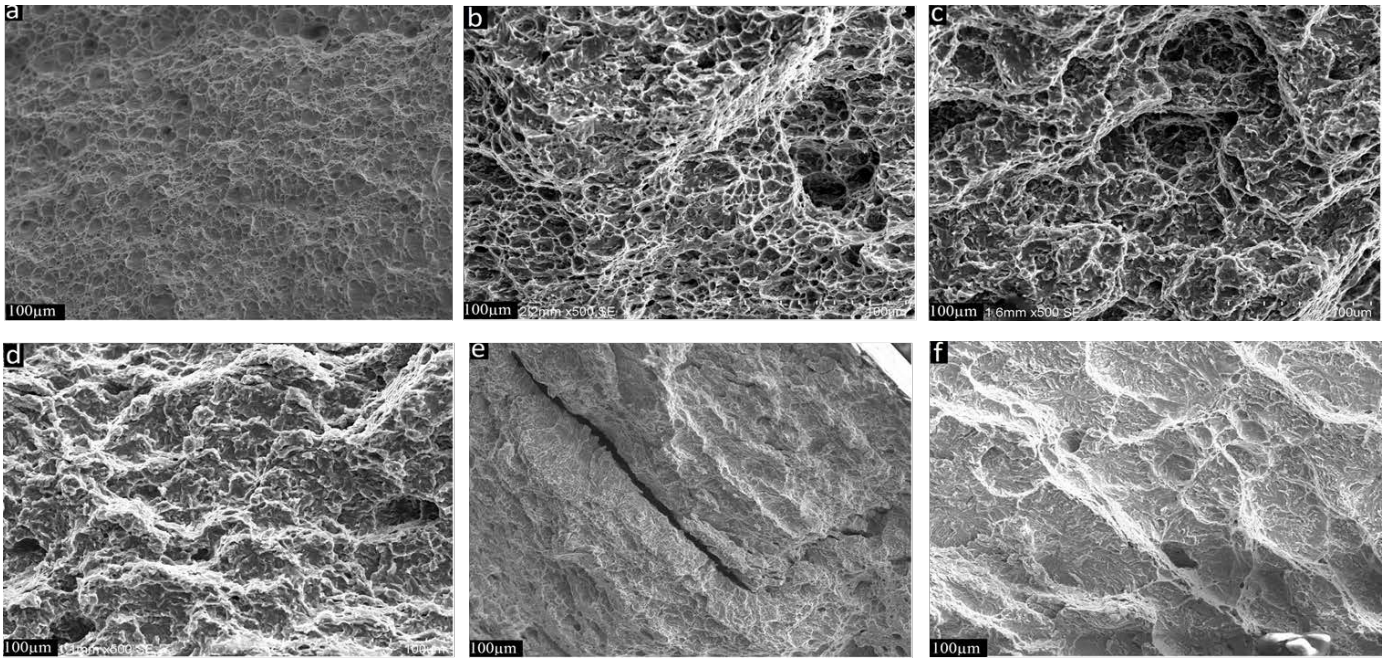

Fig. 4.34. SEM images of fracture surfaces for (a) uncharged specimen tensile-tested and hydrogen charged for (b) 5 minute (c) 15 minute (d) 30 minutes (e) 2 hour (f) 10 hour.

4.5.3 Role of microstructure in tensile deformation and failure

During the tensile test experiment, it was observed that failure occurred within the HAZ of the weld sample. This suggests that the microstructure in this region contributed to the failure. In order to clearly understand the role of microstructure on failure, EBSD scan was carried out at the weld and base metal interface. Fig 4.35(a) shows the EBSD map of the WM/BM interface. The microstructure at the WM is finer compared to the HAZ. This observation is consistent with our previous discussion in section 4.1. It is well known that grain size and morphology play an important role in HIC phenomena. It was observed that fine grains provide larger misorientation of grain boundaries, and as a result reduce the mobility of hydrogen at nodes or triple junctions and decrease the hydrogen diffusion through the bulk structure of the steel [208]. Ichimura et al [209] observed that hydrogen diffusion increases with increase in the grain size since large grains are capable of providing main free path for hydrogen. Yazdipour [210] concluded that the highest diffusion rate of hydrogen in pipeline steels is obtained at an optimum grain size. Therefore it may be concluded that large grains are directly related to hydrogen diffusion as observed by [209]. The results presented in Fig 4.35(b) shows the KAM map for the WM/HAZ interface. Again, it can be seen that the dislocation accumulation is more pronounced in the HAZ region. The effect of dislocation on HIC susceptibility has already been explained in section 4.5.1.2. The high KAM values in the region made it possible to conclude that the HAZ is more prone to HIC susceptibility than the weld due to the presence of higher dislocation density in this region. Therefore, it can be concluded that both the intense grain growth experienced in HAZ and the presence of high dislocation density jointly affected the susceptibility of the steel weld to HIC under tensile load.

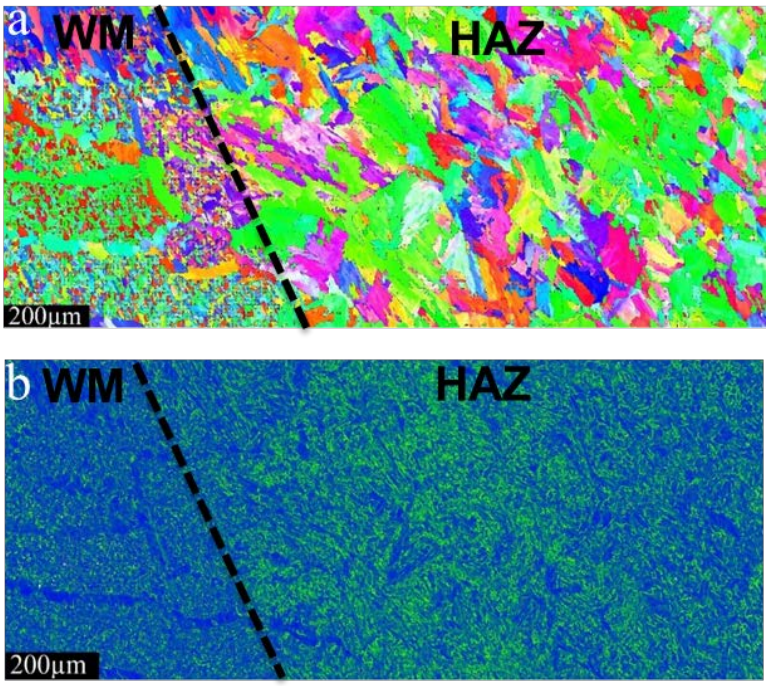

Fig. 4.35. (a) EBSD scan map and (b) Kernel average misorientation (KAM) map of the fracture region.

4.5.4. Effect of inclusions on crack initiation

Inclusions depending on their size, shape and coherency with the matrix are potential sites for initiation of failure. Fig. 4.36(a-b) show the inclusions on the fracture surface of the uncharged and 5 minutes hydrogen charged specimen. EDS analysis of the inclusion (indicated with red) is shown in Fig. 4.36(c). It indicates that the particles are Nb and Ti-rich. Suggesting that they are probably NbTi carbonitrides. It is difficult to conclude if the crack initiation can be a result of hydrogen/carbonitride interaction. However, many authors favor coarse oxide and MnS inclusions rather than fine NbTi precipitate to be an effective hydrogen trapping site [211, 212]. Ren [213] reported that carbonitrides of Nb and Ti can are less likely trap for hydrogen compared to oxide inclusions. Due to the presence of precipitates at center of dimples on fractured surfaces, we may conclude that hydrogen was trapped at the Ti,Nb)(C,N) precipitates during charging and effectively act as crack nucleation site under tensile load.

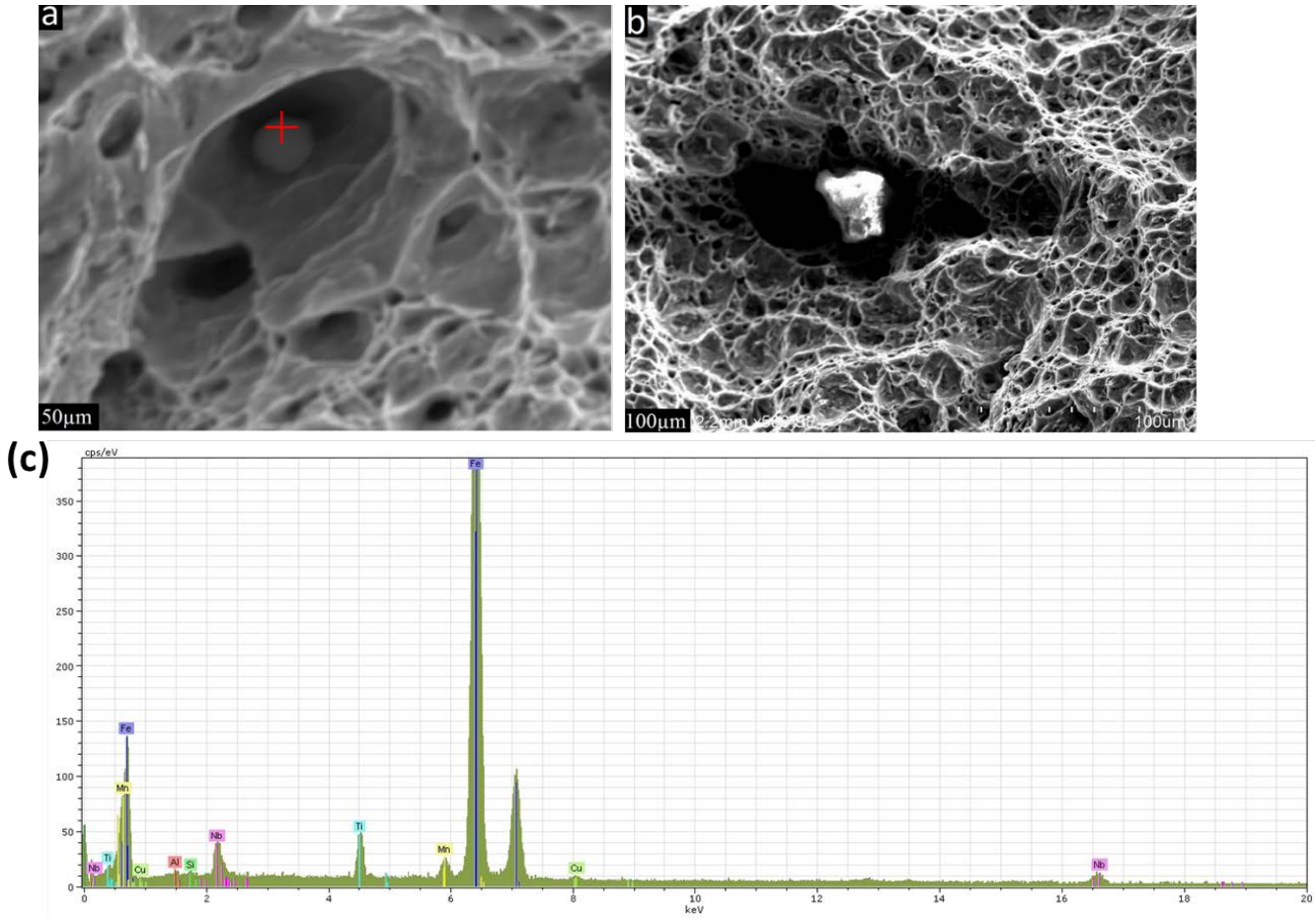

Fig. 4.36. (a) and (b) SEM image of mixed oxide inclusions observed in the fracture surfaces of tensile tested specimens and (c) EDS scan on one of the inclusions/particles showing that the type of inclusion contains Ti, Nb, C, N elements.

CHAPTER FIVE

SUMMARY, CONCLUSIONS AND RECOMMENDATIONS

5.1 Summary

The effect of submerge arc welding on microstructure and mechanical properties of weld was investigated in this work. Different characterization techniques such as optical microscope, Electron backscattered diffraction (EBSD), X-ray diffraction and Transmission electron microscope (TEM) were applied to investigate the microstructure in the weld metal and heat affected zone. Experiments were carried out to understand the effect of hydrogen on mechanical property as well as a role of microstructure on HIC susceptibility in the steel weld. It was found that the base metal consist of equiaxed ferrite grains while the weld metal consist of mainly acicular ferrite and fine bainite with Al-Si-Mn-Ti oxide particles/inclusions. The heat affected zone microstructure is coarse-grained and varied with distance from the fusion zone. It mainly consist of coarsened ferrite and martensite with NbTi(CN) precipitate/particles. EBSD and TEM analysis showed that dislocation density was higher at the weld metal cross section compare to the weld top surface and the base metal. This indicates that the amount of welding residual strain is higher at the weld metal cross section. Compressive residual stresses were formed due to welding at the weld top surface while a mixture of tensile and compressive stress were observed in the weld cross section. HIC experiment showed that grain morphology and Al-Si-Mn-Ti inclusions/particles influenced pitting formation, that we considered nucleation sites for cracks in the weld zone. The cracks observed in the heat affected zone were found to be both transgranular and intergranular. The cracks in the weld were observed to propagate by coalescence of smaller pits to form micro cracks. The tensile test demonstrated that the ductility in the steel weld decreased with increasing charging time under tensile load. The result showed that the intense grain growth in the HAZ and

the high dislocation have a synergistic effect on the susceptibility of the steel weld to HIC under tensile load.

5.2. Conclusions

Based on the characterization of structure carried out with EBSD, TEM, EDS, X-ray diffraction, optical microscopy and mechanical testing experiments simulating HIC enviroment, the following conclusions may be drawn from this research.

1. The weld metal microstructure has acicular ferrite grains formed in packets which have certain crystallographic orientation but contain submicron grains arranged in a chaotic interlocking manner. TEM and EDS observation show that most of the inclusions in the weld metal have spherical shape and containing Al, O, Si, Ti and Mn. The acicular ferrite nucleation was seen to originate from these inclusions.
2. The weld microstructure and porosity distribution at the cross section of the weld varied with depth in the weld metal cross section. The kernel average misorientation (KAM) analysis of the base metal, weld top surface and weld cross section showed that the amount of welding residual strain was higher within the weld metal cross section. The microstructure of the HAZ was found to be coarse grained and changes with distance from the fusion zone. It consists mainly of ferrites and bainite. The precipitates are of mixed composition and contains Ti, Nb, C, N elements. The HAZ microstructure also shows the presence of high density of dislocations
3. The hardness values of the base metal, weld metal and heat affected zone show a direct correlation to the microstructure and show that the grain size has an important effect of hardness.

4. The cracks initiated in the weld from hydrogen related localized pitting associated with Al-Si-Mn-Ti oxide inclusions. The crack propagation mechanism involve coalescence of smaller pits to form micro cracks. The HIC crack propagation in the HAZ was both transgranular through grains with {123} planes and intergranular crack along boundaries of {110}, {111} and {112} oriental grains.
5. The ductility in the steel weld decreased as hydrogen charging time increased. Fine dimples were observed on surfaces of uncharged tensile-tested specimen. This observation show that fracture was 100% ductile in uncharged specimen while hydrogen charged specimens showed a mixture of ductile and brittle failure and completely brittle fracture for charging time exceeding 2 hours.
6. All of the specimen fractured at the heat affected zone. This shows that the grain growth experienced in the HAZ and the presence of high dislocation density jointly affected the susceptibility of the steel weld to HIC under tensile load.

5.3. Recommendations for future work

1. The study should be done for different welding parameters in order to evaluate direct correlation with welding process.
2. Study the effect of crystallographic texture on HIC susceptibility of the weld metal should be done.

References

[1] Spiral pipe for offshore application, (2012), GIA [Online], accessed on 10th April, 2015 available from World Wide Web; http://pipabawahlaut.wordpress.com/category/spiral pipe for-offshore-application/

[2] Spiral welded pipes and tubes, (2012), a global strategic business report [Online], Accessed on 14th August, 2015, available from World Wide Web http://www.strategyr.com/Spiral_Welded_Pipes_and_Tubes_Market_Report.asp

[3] Outlook for the large OD linepipe Market, (2013), Energy Research Portfolio [Online], Accessed on 12th August, 2015 available from World Wide Web; http://www.metalbulletinresearch.com/

[4] Alberta Energy Regulator, Report 2013-B: Pipeline Performance in Alberta, 2013, Alberta

[5] Davenport, T. J. (1991). A further survey of pressure vessel failures in the UK. Reliability 91, pp84.

[6] Gu, B., Luo, J., and Mao, X. (1999). Hydrogen-facilitated anodic dissolution-type stress corrosion cracking of pipeline steels in near-neutral pH solution.Corrosion, 55(1), 96-10.

[7] Nakai, Y., Kurahashi, H., Emi, T., and Haida, O. (1979). Development of steels resistant to hydrogen induced cracking in wet hydrogen sulfide environment. Transactions ISIJ, Vol.19 No.7, 1997, pp. 401-410.

[8] Domizzi, G., Anteri, G. and Ovejero-Garcıa, J. (2001). Influence of sulphur content and inclusion distribution on the hydrogen induced blister cracking in pressure vessel and pipeline steels. Corrosion Science, 43(2), 325-339.

[9] Taira, T., Kobayashi, Y., Matsumoto, K., Matsumoto, S., Terunuma, T., and Arikata, K. (1982). Resistance of pipeline steels to wet sour gas. In current solutions to hydrogen problems in steels, Proceedings of the first international conference, ASM, Ohio pp.173-180.

[10] DenOuden, G., Verhagen, J. G., and Tichelaar, G. W. (1975). Influence of chemical composition on mild steel weld metal notch toughness. Welding Journal, 54(3), pp. 87.

[11] Widgery, D. J. (1976). Deoxidation practice for mild steel weld metal. Welding journal, 55(3), 57-68.

[12]. Houldcroft, P. T. (1989). Submerged-arc welding. Woodhead publishing.

[13] Funderburk, R. S. (1999). Key concepts in welding engineering. Welding Innovation, 16(1), 1-4.

[14] SAW or submerge arc welding, Welding information, updated Daily, www.weldguru.com/saw.html, (Accessed February, 2016).

[15] Lee, C. S., Chandel, R. S., and Seow, H. P. (2000). Effect of welding parameters on the size of heat affected zone of submerged arc welding. Materials and Manufacturing Processes, 15(5), 649-666.

[16] Bhadeshia, H. K. D. H. (1999). Some phase transformations in steels. Materials science and technology, 15(1), 22-29.

[17] Jang, J., and Indacochea, J. E. (1987). Inclusion effects on submerged-arc weld microstructure. Journal of materials science, 22(2), 689-700.

[18] Tuliani, S. S., Boniszewski, T., and Eaton, N. F. (1969). Notch toughness of commercial submerged arc weld metal. Welding and Metal Fabrication, 37(8), 327-339.

[19] Ito, Y., Nakanishi, M., and Komizo, Y. I. (1982). Effects of oxygen on low carbon steel weld metal. Metal Construction, 14, 472-8.

[20] Kayali, E. S., Corbett, J. M., and Kerr, H. W. (1983). Observations on inclusions and acicular ferrite nucleation in submerged arc HSLA welds. Journal of Materials Science Letters, 2(3), 123-128.

[21] Jackson, C. E. (1982). Submerged-arc welding, fluxes and relations among process variables. Metals Hand Book, ASM, Metals Park, OH, 73-77.

[22] Franke, G. L. (1985). Submerged arc welding of high yield strength steel. In Proc. of the Int. Conf. on welding for Challenging Environments (pp. 283-291).

[23] Grong, O., and Matlock, D. K. (1986). Microstructural development in mild and low-alloy steel weld metals. International Metals Reviews, 31(1), 27-48.

[24] Smith, N. J., McGrath, J. T., Gianetto, J. A., and Orr, R. F. (1989). Microstructure/mechanical property relationships of submerged arc welds in HSLA 80 steel. Welding Journal, 68(3), 11.

[24] James Amanie, (2011). Effect of submerged arc welding parameters on the microstructure of SA516 and A709 Steel Welds (PhD thesis, University of Saskatchewan, Saskatoon, Canada). Retrieved from http://ecommons.usask.ca/handle/10388/ETD-2011 07-42

[25] Easterling, K. (1992). Introduction to the physical metallurgy of welding. Elsevier.

[26] Lee, C. S., Chandel, R. S., and Seow, H. P. (2000). Effect of welding parameters on the size of heat affected zone of submerged arc welding. Materials and Manufacturing Processes, 15(5), 649-666.

[27] Farrar, R. A., Zhang, Z., Bannister, S. R., and Barritte, G. S. (1993). The effect of prior austenite grain size on the transformation behaviour of C-Mn-Ni weld metal. Journal of materials science, 28(5), 1385-1390.

[28] Hashemi, S. H., and Mohammadyani, D. (2012). Characterisation of weldment hardness, impact energy and microstructure in API X65 steel. International Journal of Pressure Vessels and Piping, 98, 8-15.

[29] Abson, D. J., and Pargeter, R. J. (1986). Factors influencing as-deposited strength, microstructure, and toughness of manual metal arc welds suitable for C-Mn steel fabrications. International Metals Reviews, 31(1), 141-196.

[30] Kou, S. (1987). Welding metallurgy. New York.

[31] Çalik, A. (2009). Effect of cooling rate on hardness and microstructure of AISI 1020, AISI 1040 and AISI 1060 Steels. Int. J. of Phys. Sci, 4(9), 514-518.

[32] Qiao, Z. X., Liu, Y. C., Yu, L. M., and Gao, Z. M. (2009). Effect of cooling rate on microstructural formation and hardness of 30CrNi3Mo steel. Applied Physics A, 95(3), 917-922.

[33] Li, L. C., Chai, M. Y., Li, Y. Q., Bai, W. J., and Duan, Q. (2013, August). Effect of welding heat input on grain size and microstructure of 316L stainless steel welded Joint. Applied mechanics and Materials (Vol. 331, pp. 578-582).

[34] Thornton, C. E., and Webster, D. J. (1990). Progress in the use of metal powder additions for the welding of offshore structures. In Proceeding of the Ninth International Conference on offshore mechanics and arctic Engineering (Vol. 3, pp. 399-408).

[35] Kumar, S., and Shahi, A. S. (2011). Effect of heat input on the microstructure and mechanical properties of gas tungsten arc welded AISI 304 stainless steel joints. Materials & Design, 32(6), 3617-3623.

[36] Agilan, M., Venkateswaran, T., Sivakumar, D., and Pant, B. (2014). Effect of heat input on microstructure and mechanical properties of inconel-718 EB Welds. Procedia Materials Science, 5, 656-662.

[37] Grajcar, A., Różański, M., Stano, S., Kowalski, A., and Grzegorczyk, B. (2014). Effect of heat input on microstructure and hardness distribution of laser welded Si-Al TRIP-type steel. Advances in Materials Science and Engineering, 2014.

[38] Sadeghian, M., Shamanian, M., and Shafyei, A. (2014). Effect of heat input on microstructure and mechanical properties of dissimilar joints between super duplex stainless steel and high strength low alloy steel. Materials & Design, 60, 678-684.

[39] Dong, H., Hao, X., and Deng, D. (2014). Effect of welding heat input on microstructure and mechanical properties of HSLA steel joint. Metallography, microstructure, and analysis, 3(2), 138-146.

[40] Nath, S. K., Kumar, S., and Kumar, V. (2015). Effect of single and multiple thermal cycles on microstructure and mechanical properties of simulated HAZ in low carbon bainitic steel. Materials Performance and Characterization, 4(3), 365-380.

[41] Wan, H. S., Nurul Syahida, N. M., Sarizam, M., and Saifulnizan, J. (2015, November). Effect of welding heat input on microstructure and mechanical properties at coarse grain heat affected zone of ABS Grade A Steel. ARPN Journal of Engineering and Applied Sciences, 10(20), 9487-9495.

[42] Apurv, C., and Vijaykumar, J. S. (2014). Influence of welding heat input on mechanical properties and microstructureof austenitic 202 grade stainless steel weldments. wseas transactions on applied and theoretical mechanics, 9, 222-228.

[43] Powell, G. L. F., and Herfurth, G. (1998). Charpy V-notch properties and microstructures of narrow gap ferritic welds of a quenched and tempered steel plate. Metallurgical and Materials Transactions A, 29(11), 2775-2784.

[44] Dowling, J. M., Corbett, J. M., and Kerr, H. W. (1986). Inclusion phases and the nucleation of acicular ferrite in submerged arc welds in high strength low alloy steels. Metallurgical Transactions A, 17(9), 1611-1623.

[45] Thewlis, G. (1994). Transformation kinetics of ferrous weld metals. Materials science and technology, 10(2), 110-125.

[46] Ahlblom, B. (1983). Effect of residual, impurity and microalloying elements on weldability and weld properties. In Proceedings of the International Conference in the Welding Institute, London, Paper (Vol. 27).

[47] Komanduri, R., and Hou, Z. B. (2001). Thermal analysis of the arc welding process: part II. Effect of variation of thermophysical properties with temperature. Metallurgical and Materials Transactions B, 32(3), 483-499.

[48] Poorhaydari, K., Patchett, B. M., and Ivey, D. G. (2005). Estimation of cooling rate in the welding of plates with intermediate thickness. Welding Journal, 84(10), 149s-155s.

[49] Dutta, J., and Narendranath, S. (2014). Estimation of cooling rate and its effect on temperature dependent properties in gta welded high carbon steel joints.

[50] Farrar, R. A., and Harrison, P. L. (1987). Acicular ferrite in carbon-manganese weld metals: an overview. Journal of materials science, 22(11), 3812-3820.

[51] Vitek, J. M., and David, S. A. (1988). The effect of cooling rate on ferrite in type-308 stainless-steel weld metal. Welding Journal, 67(5), S95-S102.

[52] Madariaga, I., Gutierrez, I., García de Andrés, C., and Capdevila, C. (1999). Acicular ferrite formation in a medium carbon steel with a two stage continuous cooling. . Scripta Materialia, 41(3), 229-235

[53] Dallam, C. B., Liu, S., and Olson, D. L. (1985). Flux composition dependence of microstructure and toughness of submerged arc HSLA weldments.Welding Journal, 64(5), 140-151.

[54] Fox, A. G., Eakes, M. W., and Franke, G. L. (1996). The effect of small changes in flux basicity on the acicular ferrite content and mechanical properties of submerged arc weld metal of Navy HY-100 steel. Welding Journal-Including Welding Research Supplement, 75(10), 330.

[55] Krishnadev, M. R., Zhang, W. L., Vaidya, V., Gendron, A., Bowker, J. T., and Rene, R. (1999). Extra low carbon welding consumables for HSLA 80 and HSLA 100 steels and improving HAZ toughness at high heat inputs. International Symposium on Metal Welding and Applications as held at the 38th Annual Conference of Metallurgists of CIM (pp. 55-70).

[56] R. F. Arnoldy. (1967). Bulk Welding in 1966, 46 (2), 117–122.

[57] Barbangelo, A. (1990). Influence of alloying elements and heat treatment on impact toughness of chromium steel surface deposits. Journal of Materials Science, 25(6), 2975-2984.

[58] Thornton, C. E., and Webster, D. J. (1990). Progress in the use of metal powder additions for the welding of offshore structures. In Proceeding of the Ninth International Conference on Offshore Mechanics and Arctic Engineering (Vol. 3, pp. 399-408).

[59] P. E. McDonald, (1985), Factors influencing the microstructure and mechanical properties of ultra-low carbon bainitic 100 tungsten inert gas multipass weldments", Ph.D. Thesis, University of Utah, USA.

[60] Poulalion, A., and Botte, R. (1988). Nitrogen addition in steel making using nitriding ferroalloys. High Nitrogen Steels--HNS 88, 49-52.

[61] Farrar, R. A., and Harrison, P. L. (1987). Acicular ferrite in carbon-manganese weld metals: an overview. Journal of materials science, 22(11), 3812-3820.

[62] Evans, G. M. (1998). Effect of nitrogen on C-Mn steel welds containing titanium and boron. Welding Journal-New York, 77, 239-s.

[63] Ilman, M. N., Cochrane, R. C., and Evans, G. M. (2014). Effect of titanium and nitrogen on the transformation characteristics of acicular ferrite in reheated C–Mn steel weld metals. Welding in the World, 58(1), 1-10.

[64] Bang KS, Kim WY and Park C (2007). Effects of nitrogen on weld metal microstructure and toughness in submerged arc welding. Materials Science Forum 539–543:3906–3911.

[65] Thewlis G, Whiteman JA, and Senogles D (1997). Dynamics of austenite to ferrite phase transformation in ferrous weld metals. Materials Science and Technology 13(3):257–274.

[66] DenOuden, G., Verhagen, J. G., and Tichelaar, G. W. (1975). Influence of chemical composition on mild steel weld metal notch toughness. Welding Journal, 54(3), 87.

[67] Evans, G. M. (1983). The effect of carbon on the microstructure and properties of C- Mn all weld metal deposits. Weld. Res. Abroad, 19(1), 13-24.

[68] Chang, C. M., Lin, C. M., Hsieh, C. C., Chen, J. H., Fan, C. M., and Wu, W. (2009). Effect of carbon content on microstructural characteristics of the hypereutectic Fe–Cr–C claddings. Materials Chemistry and Physics, 117(1), 257-261.

[69] Chang, C. M., Hsieh, C. C., Lin, C. M., Chen, J. H., Fan, C. M., and Wu, W. (2010). Effect of carbon content on microstructure and corrosion behavior of hypereutectic Fe–Cr–C claddings. Materials Chemistry and Physics, 123(1), 241-246.

[70] Abson, D. J., and Pargeter, R. J. (1986). Factors influencing as-deposited strength, microstructure, and toughness of manual metal arc welds suitable for C-Mn steel fabrications. International Metals Reviews, 31(1), 141-196.

[71] Moll, R. A., and Stout, R. D. (1967). Composition effects in iron-base weld metal. Weld J, 46(12).

[72] Bailey, n., and welding institute. (1983). titanium flux additions during submerged-arc welding of ferritic steels. Welding Institute Report No. 221, pp. 1-22.

[73] Oldland, P. T., Ramsay, C. W., Matlock, D. K., and Olson, D. L. (1989). Significant features of high-strength steel weld metal microstructures. Welding Journal, 68(4), 158s-168s.

[74] St-Laurent, S., and L'Espérance, G. (1992). Effects of chemistry, density and size distribution of inclusions on the nucleation of acicular ferrite of C-Mn steel shielded-metal-arc-welding weldments. Materials Science and Engineering: A, 149(2), 203-216.

[75] Bhole, S. D., Nemade, J. B., Collins, L., and Liu, C. (2006). Effect of nickel and molybdenum additions on weld metal toughness in a submerged arc welded HSLA line-pipe steel. Journal of Materials Processing Technology, 173(1), 92-100.

[76] Jorge, J. C. F., Souza, L. F. G., and Rebello, J. M. A. (2001). The effect of chromium on the microstructure/toughness relationship of C–Mn weld metal deposits. Materials Characterization, 47(3), 195-205.

[77] Surian, E., Trotti, J., Cassanelli, A., and De Vedia, L. (1994). Influence of chromium on the mechanical properties and microstructure of weld metal from a high-strength SMA electrode. Welding journal-new York-, 73, 45-s.

[78] Surian, E., De Rissone, M. R., and De Vedia, L. (2005). Influence of molybdenum on ferritic high-strength SMAW All-Weld-Metal properties.Welding Journal, USA, 84(4), 53s-62s.

[79] Rampaul, H. (2003). Pipe welding procedures. Industrial Press.

[80] Widgery, D. J. (1976). Deoxidation practice for mild steel weld metal. Welding journal, 55(3), 57-68.

[81] Evans, G. M. (1996). Microstructure and properties of ferritic steel welds containing Ti and B. Welding Journal, 75(8).

[82] Chaveriat, P. F., Kim, G. S., Shah, S., and Indacochea, J. E. (1987). Low carbon steel weld metal microstructures: the role of oxygen and manganese. Journal of materials engineering, 9(3), 253-267.

[83] Svensson, L. E. (1999). Consumables for welding high strength steels. Svetsaren, Sweden, 54(1-2), 29-33.

[84] Svensson, L. E., and Gretoft, B. (1990). Microstructure and impact toughness of C--Mn weld metals. Welding Journal, 69(12), 454.

[85] Zhao, M. C., Yang, K., Xiao, F. R., and Shan, Y. Y. (2003). Continuous cooling transformation of undeformed and deformed low carbon pipeline steels.Materials Science and Engineering: A, 355(1), 126-136.

[86] Belato Rosado, D., De Waele, W., Vanderschueren, D., and Hertelé, S. (2013). Latest developments in mechanical properties and metallurgical features of high strength line pipe

steels. In 5th International Conference on Sustainable Construction and Design (Vol. 4, No. 1). Ghent University, Laboratory Soete.

[87] Taylor, D. S., and Evans, G. M. (1983). Development of MMA electrodes for offshore fabrication. Metal Constr. 15. 438.

[88] Harrison, P. L. (1983). Acicular ferrite in carbon-manganese weld metals (Doctoral dissertation, PhD Thesis, University of Southampton, 1983.

[89] Eagar, T. W. (1978). Sources of weld metal oxygen contamination during submerged arc welding. Welding Journal, 57(3).

[90] Burck, P. A., Indacochea, J. E., and Olson, D. L. (1990). Effects of welding flux additions on 4340 steel weld metal composition. Welding Journal, 3, 115-122.

[91] Indacochea, J. E., Blander, M., Christensen, N., and Olson, D. L. (1985). Chemical reactions during submerged arc welding with FeO-MnO-SiO2 fluxes. Metallurgical Transactions B, 16(2), 237-245.

[92] Davis, M. L. E., and Bailey, N. (1980). How submerged-arc flux composition influences element transfer. Weld Pool Chemistry and Metallurgy, 289-310.

[93] Dallam, C. B., Liu, S., and Olson, D. L. (1985). Flux composition dependence of microstructure and toughness of submerged arc HSLA weldments.Welding Journal, 64(5), 140-151.

[94] Kayali, E. S., Corbett, J. M., and Kerr, H. W. (1983). Observations on inclusions and acicular ferrite nucleation in submerged arc HSLA welds.Journal of Materials Science Letters, 2(3), 123-128.

[95] North, T. H., Bell, H. B., Koukabi, A., and Craig, I. (1979). Notcht toughness of low Oxygen-content submerged arc deposits. Welding journal, 58(12), s343-s354.

[96] Abson, D. J., Dolby, R. E., and Hart, P. H. M. (1978). The role of non-metallic inclusions in ferrite nucleation in carbon steel weld metals. Trends in Steel and Consumables for Welding, 1, 75-101.

[97] Harrison, P. L. and Farrar, R. A. (1981). Influence of oxygen-rich inclusions on the $\gamma \rightarrow \alpha$ phase transformation in high-strength low-alloy (HSLA) steel weld metals. Journal of Materials Science, 16(8), 2218-2226.

[98] Francis, R. E., Jones, J. E., and Olson, D. L. (1990). Effect of shielding gas oxygen activity on weld metal microstructure of GMA welded microalloyed HSLA steel. Welding journal, 69(11), 408.

[99] Sun, D., Zhou, Z., Wang, W., and Liu, L. (2002). Effect of Si, Mn and Al on the microstructure and mechanical properties of ADI weld metal. Cailiao Kexue Yu Jishu (Journal of Materials Science & Technology) (China)(USA), 18, 271-274.

[100] Dorschu, K. E. and Stout, R. D. (1961) "Some Factors Affecting the Notch Toughness of Steel Weld Metal," Weld. Jour. 40 (3), Res. Suppl., 97s.

[101] Tuliani, S. S., and Farrar, R. (1975). Effects of Si in submerged-arc weld metals at low concentrations. Welding and Metal Fabrication, 43(7), 553-558.

[102] Trindade, V. B., da Cruz Payão, J., Souza, L. F. G., and da Rocha Paranhos, R. (2007). The role of addition of Ni on the microstructure and mechanical behaviour of C-Mn weld metals. Exacta, 5(1), 177-183.

[103] Beidokhti, B., Koukabi, A. H., and Dolati, A. (2009). Influences of titanium and manganese on high strength low alloy SAW weld metal properties. Materials Characterization, 60(3), 225-233.

[104] Lee, H. W., Kim, Y. H., Lee, S. H., Lee, K. H., Park, J. U., and Sung, J. H. (2007). Effect of boron contents on weldability in high strength steel. Journal of mechanical science and technology, 21(5), 771-777.

[105] Oh, D. W., Olson, D. L. and Frost, R. H. (1990). The influence of boron and titanium on low-carbon steel weld metal. Welding Journal, 69(4), 151s-158s.

[106] Shim, J. H., Oh, Y. J., Suh, J. Y., Cho, Y. W., Shim, J. D., Byun, J. S. and Lee, D. N. (2001). Ferrite nucleation potency of non-metallic inclusions in medium carbon steels. Acta Materialia, 49(12), 2115-2122.

[107] Shim, J. H., Cho, Y. W., Chung, S. H., Shim, J. D., and Lee, D. N. (1999). Nucleation of intragranular ferrite at Ti_2O_3 particle in low carbon steel. Acta Materialia, 47(9), 2751-2760.

[108] Gregg, J. M., and Bhadeshia, H. K. D. H. (1997). Solid-state nucleation of acicular ferrite on minerals added to molten steel. Acta Materialia, 45(2), 739-748.

[109] Zhao, M. C., Shan, Y. Y., Xiao, F. R., Yang, K., and Li, Y. H. (2002). Investigation on the H_2S-resistant behaviors of acicular ferrite and ultrafine ferrite. Materials Letters, 57(1), 141-145.

[110] Kim, Y. M., Kim, S. K., Lim, Y. J., and Kim, N. J. (2002). Effect of microstructure on the yield ratio and low temperature toughness of linepipe steels. ISIJ international, 42(12), 1571-1577.

[111] Ricks, R. A., Howell, P. R., and Barritte, G. S. (1982). The nature of acicular ferrite in HSLA steel weld metals. Journal of Materials Science, 17(3), 732-740.

[112] Babu, S. S., and Bhadeshia, H. K. D. H. (1992). Stress and the acicular ferrite transformation. Materials Science and Engineering: A, 156(1), 1-9.

[113] Wu, K. M. (2006). Three-dimensional analysis of acicular ferrite in a low-carbon steel containing titanium. Scripta materialia, 54(4), 569-574.

[114] Mizuno, M., Tanaka, I., and Adachi, H. (1998). Chemical bonding at the Fe/TiX (X= C, N or O) interfaces. Acta materialia, 46(5), 1637-1645.

[115] Zhang, Z., and Farrar, R. A. (1996). Role of non-metallic inclusions in formation of acicular ferrite in low alloy weld metals. Materials Science and Technology, 12(3), 237-260.

[116] Wan, X. L., Wang, H. H., Cheng, L., and Wu, K. M. (2012). The formation mechanisms of interlocked microstructures in low-carbon high-strength steel weld metals. Materials Characterization, 67, 41-51.

[117] Fattahi, M., Nabhani, N., Hosseini, M., Arabian, N., and Rahimi, E. (2013). Effect of Ti containing inclusions on the nucleation of acicular ferrite and mechanical properties of multipass weld metals. Micron, 45, 107-114.

[118] Ramírez, J. A., and González, J. L. (2003, January). Hydrogen induced cracking of welds in steel pipelines. In ASME 2003 Pressure Vessels and Piping Conference (pp. 35-44). American Society of Mechanical Engineers.

[119] Cheng, Y. F. (2007). Analysis of electrochemical hydrogen permeation through X-65 pipeline steel and its implications on pipeline stress corrosion cracking. International Journal of Hydrogen Energy, 32(9), 1269-1276.

[120] Koh, S. U., Jung, H. G., Kang, K. B., Park, G. T., and Kim, K. Y. (2008). Effect of microstructure on hydrogen-induced cracking of linepipe steels. Corrosion, 64(7), 574-585.

[121] Mohtadi-Bonab, M. A., Eskandari, M., and Szpunar, J. A. (2015). Texture, local misorientation, grain boundary and recrystallization fraction in pipeline steels related to hydrogen induced cracking. Materials Science and Engineering: A, 620, 97-106.

[122] Lucio-Garcia, M. A., Gonzalez-Rodriguez, J. G., Casales, M., Martinez, L., Chacon-Nava, J. G., Neri-Flores, M. A., and Martinez-Villafañe, A. (2009). Effect of heat treatment on H 2S corrosion of a micro-alloyed C–Mn steel.Corrosion Science, 51(10), 2380-2386.

[123] Tetelman, A. S., and Robertson, W. D. (1961). The mechanism of hydrogen embrittlement observed in iron-silicon single crystals (No. TR3). yale univ new haven ct hammond lab.

[124] Zapffe, C. A., and Sims, C. E. (1941). Hydrogen embrittlement, internal stress and defects in steel. Trans. AIME, 145(1941), 225-271.

[125] Ohkita, S., and Horii, Y. (1995). Recent development in controlling the microstructure and properties of low alloy steel weld metals. ISIJ international, 35(10), 1170-1182.

[126] Elboujdaini M, Shehata MT, Revie RW (1998) Performance of pipeline steels in sour service. Proc. 37th Int Symp Materials for Resource Recovery and Transport, Conf of Metallurgists, CIM, Calgary, August.

[127] Kittel, J., Smanio, V., Fregonese, M., Garnier, L., and Lefebvre, X. (2010). Hydrogen induced cracking (HIC) testing of low alloy steel in sour environment: Impact of time of exposure on the extent of damage. Corrosion Science, 52(4), 1386-1392.

[128] Mohtadi-Bonab, M. A., Szpunar, J. A., Collins, L., and Stankievech, R. (2014). Evaluation of hydrogen induced cracking behavior of API X70 pipeline steel at different heat treatments. International journal of hydrogen energy, 39(11), 6076-6088.

[129] Carneiro, R. A., Ratnapuli, R. C., and Lins, V. D. F. C. (2003). The influence of chemical composition and microstructure of API linepipe steels on hydrogen induced cracking and sulfide stress corrosion cracking. Materials Science and Engineering: A, 357(1), 104-110.

[130] Tsuru, T., and Latanision, R. M. (1982). Grain boundary transport of hydrogen in nickel. Scripta Metallurgica, 16(5), 575-578.

[131] Choo WY, Lee JY, Cho CG. (1981). Effect of grain Size. Materials science; 16: 1285–93.

[132] Kimura, A., and Birnbaum, H. K. (1988). Hydrogen induced grain boundary fracture in high purity nickel and its alloys—enhanced hydrogen diffusion along grain boundaries. Acta Metallurgica, 36(3), 757-766.

[133] Calder, R. D., Elleman, T. S., and Verghese, K. (1973). Grain boundary diffusion of tritium in 304-and 316-stainless steels. Journal of Nuclear Materials, 46(1), 46-52.

[134] Brass, A. M., and Chanfreau, A. (1990). Electrochemical permeation of hydrogen in high purity nickel at 100° C. Scripta Metallurgica et Materialia, 24(3), 499-504.

[135] Huang, F., Liu, J., Deng, Z. J., Cheng, J. H., Lu, Z. H., and Li, X. G. (2010). Effect of microstructure and inclusions on hydrogen induced cracking susceptibility and hydrogen trapping efficiency of X120 pipeline steel. Materials Science and Engineering: A, 527(26), 6997-7001.

[136] Xue, H. B., and Cheng, Y. F. (2011). Characterization of inclusions of X80 pipeline steel and its correlation with hydrogen-induced cracking. Corrosion science, 53(4), 1201-1208.

[137] Lee, S. M., and Lee, J. Y. (1987). The effect of the interface character of TiC particles on hydrogen trapping in steel. Acta Metallurgica, 35(11), 2695-2700.

[138] Ren, X. C., Zhou, Q. J., Shan, G. B., Chu, W. Y., Li, J. X., Su, Y. J., and Qiao, L. J. (2008). A nucleation mechanism of hydrogen blister in metals and alloys. Metallurgical and Materials Transactions A, 39(1), 87-97.

[139] Dong, C. F., Liu, Z. Y., Li, X. G., and Cheng, Y. F. (2009). Effects of hydrogen-charging on the susceptibility of X100 pipeline steel to hydrogen-induced cracking. International journal of hydrogen energy, 34(24), 9879-9884.

[140] Nanninga, N., Grochowsi, J., Heldt, L., and Rundman, K. (2010). Role of microstructure, composition and hardness in resisting hydrogen embrittlement of fastener grade steels. Corrosion Science, 52(4), 1237-1246.

[141] Nanninga, N., Grochowsi, J., Heldt, L., and Rundman, K. (2010). Role of microstructure, composition and hardness in resisting hydrogen embrittlement of fastener grade steels. Corrosion Science, 52(4), 1237-1246.

[142] Perez, T. E., Funes, A., and Ovejero Garcia, (1982). J. Proceedings of the Third International Congress on Hydrogen and Materials, Paris, p. 923

[143] K. Ohnishi, R. Watanabe, R. Chiba, M. Murai, (1977) in: Proceedings of the Second International Congress on Hydrogen in Metals, Pergamon Press.

[144] Hejazi, D., Saleh, A. A., Haq, A., Dunne, D., Calka, A., Gazder, A. A., and Pereloma, E. V. (2014, May). Role of microstructure in susceptibility to hydrogen embrittlement of X70 microalloyed steel. In Materials Science Forum (Vol. 783, pp. 961-966).

[145] Venegas, V., Caleyo, F., Baudin, T., Espina-Hernandez, J. H., and Hallen, J. M. (2011). On the role of crystallographic texture in mitigating hydrogen-induced cracking in pipeline steels. Corrosion Science, 53(12), 4204-4212.

[146] Mohtadi-Bonab, M. A., Szpunar, J. A., Basu, R., and Eskandari, M. (2015). The mechanism of failure by hydrogen induced cracking in an acidic environment for API 5L X70 pipeline steel. International Journal of Hydrogen Energy, 40(2), 1096-1107.

[147] Oriani, R. A. (1978). Hydrogen embrittlement of steels. Annual review of materials science, 8(1), 327-357.

[148] Bechtle, S., Kumar, M., Somerday, B. P., Launey, M. E., and Ritchie, R. O. (2009). Grain boundary engineering markedly reduces susceptibility to intergranular hydrogen embrittlement in metallic materials. Acta materialia, 57(14), 4148-4157.

[149] McCright, R.D., (1973). Effect of environmental species and metallurgical structure on hydrogen entry into steel, in stress corrosion cracking and hydrogen embrittlement of Iron base alloys. NACE, p.306-325.

[150] Rozenak, P. (2007). Hemispherical bubbles growth on electrochemically charged aluminum with hydrogen. International Journal of Hydrogen Energy, 32(14), 2816-2823.

[151] Abraham, D. P., and Altstetter, C. J. (1995). Hydrogen-enhanced localization of plasticity in an austenitic stainless steel. Metallurgical and Materials transactions A, 26(11), 2859-2871.

[152] Pan, C., Chu, W. Y., Li, Z. B., Liang, D. T., Su, Y. J., Gao, K. W., and Qiao, L. J. (2003). Hydrogen embrittlement induced by atomic hydrogen and hydrogen-induced martensites in type 304L stainless steel. Materials Science and Engineering: A, 351(1), 293-298.

[153] Nelson, H. G. (1983). Hydrogen embrittlement. Treatise on materials science and technology, 25, 275-359.

[154] Liu, H. W., and Ficalora, P. J. (1972). Catalytic dissociation, hydrogen embrittlement, and stress corrosion cracking. International Journal of Fracture, 8(2), 223-226.

[155] Bhattacharya, D. K. (1997). Failures of welded joints. 212-220

[156] Shankar, V., Gill, T. P. S., Mannan, S. L., and Rodriguez, P. (1991). A review of hot cracking in austenitic stainless steel weldments. Indira Gandhi Centre for Atomic Research.

[157] E. Bayaraktar, D. Kaplan, L. Devillers and J. P. Chevalier, (2007). Grain growth mechanism during the welding of Inter-stitial Free (IF) Steels. Journal of Materials Processing Technology, Vol. 189, No.1-3, 2007, pp. 114-125.

[158] Boumerzoug, Z., Derfouf, C., and Baudin, T. (2010). Effect of welding on microstructure and mechanical properties of an industrial low carbon steel.Engineering, 2(07), 502.

[159] Tawfik, D., Kirstein, O., Mutton, P. J., and Chiu, W. K. (2006). Verification of residual stresses in flash-butt-weld rails using neutron diffraction. Physica B: Condensed Matter, 385, 894-896.

[160] Pearce, S. V., Linton, V. M., and Oliver, E. C. (2008). Residual stress in a thick section high strength T-butt weld. Materials Science and Engineering: A, 480(1), 411-418.

[161] Mirzaee-Sisan, A., Fookes, A. J., Truman, C. E., Smith, D. J., Brown, T. B., and Dauda, T. A. (2007). Residual stress measurement in a repair welded header in the as-welded condition and after advanced post weld treatment.International journal of pressure vessels and piping, 84(5), 265-273.

[162] Min, Y., Hong, M., Xi, Z., and Jian, L. (2006). Determination of residual stress by use of phase shifting moiré interferometry and hole-drilling method. Optics and Lasers in Engineering, 44(1), 68-79.

[163] Paradowska, A., Finlayson, T. R., Price, J. W. H., Ibrahim, R., Steuwer, A., and Ripley, M. (2006). Investigation of reference samples for residual strain measurements in a welded specimen by neutron and synchrotron X-ray diffraction. Physica B: Condensed Matter, 385, 904-907.

[164] Pearce, S. V., and Linton, V. M. (2006). Neutron diffraction measurement of residual stress in high strength, highly restrained, thick section steel welds. Physica B: Condensed Matter, 385, 590-593.

[165] Mochizuki, M. (2007). Control of welding residual stress for ensuring integrity against fatigue and stress–corrosion cracking. Nuclear Engineering and Design, 237(2), 107-123.

[166] Cheng, X., Fisher, J. W., Prask, H. J., Gnäupel-Herold, T., Yen, B. T., and Roy, S. (2003). Residual stress modification by post-weld treatment and its beneficial effect on fatigue strength of welded structures. International Journal of Fatigue, 25(9), 1259-1269.

[167] Kang, H. T., Lee, Y. L., and Sun, X. J. (2008). Effects of residual stress and heat treatment on fatigue strength of weldments. Materials Science and Engineering: A, 497(1), 37-43.

[168] Romanova, V., Balokhonov, R., and Schmauder, S. (2011). Three-dimensional analysis of mesoscale deformation phenomena in welded low-carbon steel. Materials Science and Engineering: A, 528(15), 5271-5277.

[169] Lin, M. B., Gao, K., Wang, C. J., and Volinsky, A. A. (2012). Failure analysis of the oil transport spiral welded pipe. Engineering Failure Analysis, 25, 169-174.

[170] Zeinoddini, M., Arnavaz, S., Zandi, A. P., and Vaghasloo, Y. A. (2013). Repair welding influence on offshore pipelines residual stress fields: An experimental study. Journal of Constructional Steel Research, 86, 31-41.

[171] Dewan, M., Liang, J., Wahab, M., and Okeil, A. (2013). Post-weld residual stresses and heat treatments of gas tungsten arc welded aluminum alloy AA6061-T651. World Journal of Engineering, 10(1), 11-22.

[172] Kang, H. T., Lee, Y. L., and Sun, X. J. (2008). Effects of residual stress and heat treatment on fatigue strength of weldments. Materials Science and Engineering: A, 497(1), 37-43.

[173] Bernasovský, P. (2013). Case studies of welded steel structure failures. In Acta Metallurgica Slovaca-Conference (Vol. 3, pp. 159-170).

[174] Verlinden, B., Driver, J., Samajdar, I., and Doherty, R. D. (2007). Thermo-mechanical processing of metallic materials (Vol. 11). Elsevier.

[175] Colegrove, P., Ikeagu, C., Thistlethwaite, A., Williams, S., Nagy, T., Suder, W., and Pirling,T. (2009). Welding process impact on residual stress and distortion. Science and Technology of Welding and Joining, 14(8), 717-725.

[176] Diaz-Fuentes, M., Iza-Mendia, A., and Gutierrez, I. (2003). Analysis of different acicular ferrite microstructures in low-carbon steels by electron backscattered diffraction. Study of their toughness behavior. Metallurgical and Materials Transactions A, 34(11), 2505-2516.

[177] Garcia-Mateo, C., Peet, M., Caballero, F. G., and Bhadeshia, H. K. D. H. (2004). Tempering of hard mixture of bainitic ferrite and austenite. Materials Science and Technology, 20(7), 814-818.

[178] Hwang, B., Kim, Y. G., Lee, S., Kim, Y. M., Kim, N. J., and Yoo, J. Y. (2005). Effective grain size and Charpy impact properties of high-toughness X70 pipeline steels. Metallurgical and materials transactions A, 36(8), 2107-2114.

[179] Gharibshahiyan, E., Raouf, A. H., Parvin, N., and Rahimian, M. (2011). The effect of microstructure on hardness and toughness of low carbon welded steel using inert gas welding. Materials & Design, 32(4), 2042-2048.

[180] Kaçar, R., and Kökemli, K. (2005). Effect of controlled atmosphere on the mig-mag arc weldment properties. Materials & design, 26(6), 508-516.

[181] Xuemin, M. C. S. C. W., and Subramanian, Z. L. M. (2010). Microstructure and toughness of HAZ in X80 pipeline steel with high Nb content. Acta Metall Sin, 46(5), 541-546.

[182] Lambert-Perlade, A., Gourgues, A. F., Besson, J., Sturel, T., and Pineau, A. (2004). Mechanisms and modeling of cleavage fracture in simulated heat-affected zone microstructures of a high-strength low alloy steel. Metallurgical and Materials Transactions A, 35(13), 1039-1053.

[183] Yang, J. R., and Bhadeshia, H. K. D. H. (1989). Orientation relationships between adjacent plates of acicular ferrite in steel weld deposits. Materials Science and Technology, 5(1), 93-97.

[184] Flower, H. M., and Lindley, T. C. (2000). Electron backscattering diffraction study of acicular ferrite, bainite, and martensite steel microstructures.Materials Science and Technology, 16(1), 26-40.

[185] Gurao, N. P., Adesola, A. O., Odeshi, A. G., and Szpunar, J. A. (2013). On the evolution of heterogeneous microstructure and microtexture in impacted aluminum–lithium alloy. Journal of Alloys and Compounds, 578, 183-187.

[186] Badji, R., Chauveau, T., and Bacroix, B. (2013). Texture, misorientation and mechanical anisotropy in a deformed dual phase stainless steel weld joint. Materials Science and Engineering: A, 575, 94-103.

[187] Wang, B., Liu, Z., Wang, B., Zhao, S., and Sun, J. (2014). Microstructural evolution in adiabatic shear band in the ultrafine-grained austenitic stainless steel processed by multi-axial compression. Materials Science and Engineering: A, 611, 100-107.

[188] Gerber, P., Tarasiuk, J., Chauveau, T., and Bacroix, B. (2003). A quantitative analysis of the evolution of texture and stored energy during annealing of cold rolled copper. Acta materialia, 51(20), 6359-6371.

[189] Pessoa, E. C. P., Bracarense, A. Q., Zica, E. M., Liu, S., and Perez-Guerrero, F. (2006). Porosity variation along multipass underwater wet welds and its influence on mechanical properties. Journal of Materials Processing Technology, 179(1), 239-243.

[190] Ibarra, S., Grubbs, C. E., and Liu, S. (1994, December). State of the art and practice of underwater wet welding of steel. In International workshop on underwater welding of marine structures. New Orleans, USA.

[191] Lee, T. K., Kim, H. J., Kang, B. Y., and Hwang, S. K. (2000). Effect of inclusion size on the nucleation of acicular ferrite in Welds. ISIJ international, 40(12), 1260-1268.

[192] Bhatti, A. R., Saggese, M. E., Hawkins, D. N., Whiteman, J. A., and Golding, M. S. (1984). Analysis of inclusions in submerged arc welds in micro alloyed steels. Welding journal, 63(7), S224-S230.

[193] Dowling, J. M., Corbett, J. M., and Kerr, H. W. (1986). Inclusion phases and the nucleation of acicular ferrite in submerged arc welds in high strength low alloy steels. Metallurgical Transactions A, 17(9), 1611-1623.

[194] Yamamoto, K., Matsuda, S., Haze, T., Chijiiwa, R., and Mimura, H. (1989). Residual and unspecified elements in steel. ASTM STP, 1042, 266-284.

[195] Rak, I., Gliha, V., and Koçak, M. (1997). Weldability and toughness assessment of Ti micro alloyed offshore steel. Metallurgical and materials transactions A, 28(1), 199-206.

[196] Joseph, A., Sanjai K. Rai, T. Jayakumar, and N. Murugan. "Evaluation of residual stresses in dissimilar weld joints." International Journal of Pressure Vessels and Piping 82, no. 9 (2005): 700-705.

[197] Loureiro, A. J. (2002). Effect of heat input on plastic deformation of undermatched welds. Journal of materials processing technology, 128(1), 240-249.

[198] Frankel, J., Abbate, A., and Scholz, W. (1993). The effect of residual stresses on hardness measurements. Experimental mechanics, 33(2), 164-168.

[199] Hashemi, S. H. (2011). Strength–hardness statistical correlation in API X65 steel. Materials Science and Engineering: A, 528(3), 1648-1655.

[200] Lee, J. S., Ju, J. B., Jang, J. I., Kim, W. S., and Kwon, D. (2004). Weld crack assessments in API X65 pipeline: failure assessment diagrams with variations in representative mechanical properties. Materials Science and Engineering: A, 373(1), 122-130.

[201] Hejazi, D., Haq, A. J., Yazdipour, N., Dunne, D. P., Calka, A., Barbaro, F., and Pereloma, E. V. (2012). Effect of manganese content and microstructure on the susceptibility of X70 pipeline steel to hydrogen cracking. Materials Science and Engineering: A, 551, 40-49.

[202] Standard Test Method TM-0284 – (1996), Test method evaluation of pipeline steels for resistance to stepwise cracking – NACE International, Houston, TX.

[203] Elboujdaini, M., and Revie, R. W. (2009). Metallurgical factors in stress corrosion cracking (SCC) and hydrogen-induced cracking (HIC). Journal of solid state electrochemistry, 13(7), 1091-1099.

[204] Elboujdaini, M., Li, J., Gertsman, V., Gu, G., Revie, W., Gao, M., and Katz, D. C. (2004, March). Stress Corrosion Cracking: Microstructural and Materials Properties for Crack Initiation of 16"X-52 Line Pipe Steel. In Presentation at the NACE International Conference. CORROSION/2004. Paper (Vol. 4554).

[205] Elboujdaini, M., Wang, Y. Z., Revie, R. W., Shehata, M., de Silveira, G., and Parkins, R. N. (2001). Initiation of stress corrosion cracking in pipeline steel. GRI report no. GRI, 05-0005.

[206] Oriani, R. (1985). Hydrogen degradation of ferrous alloys. Noyes Publications, Mill Rd. at Grand Ave, Park Ridge, New Jersey 7656, USA, 1985. 886.

[207] Zhang, G. A., and Cheng, Y. F. (2009). Micro-electrochemical characterization of corrosion of welded X70 pipeline steel in near-neutral pH solution.Corrosion Science, 51(8), 1714-1724.

[208] Ayesha J. Haq, K. Muzaka, D.P. Dunne, A. Calka, and E.V. Pereloma. (2011). Effect of microstructure and composition on hydrogen-permeation in X70 pipeline steels, Int. J. hydrogen energy 38 (2013) 2544–2556.

[209] Ichimura, M., Sasajima, Y., and Imabayashi, M. (1991). Grain boundary effect on diffusion of hydrogen in pure aluminum. Materials Transactions, JIM,32(12), 1109-1114.

[210] Yazdipour, N., Haq, A. J., Muzaka, K., and Pereloma, E. V. (2012). 2D modelling of the effect of grain size on hydrogen diffusion in X70 steel. Computational Materials Science, 56, 49-57.

[211] Dong, C. F., Li, X. G., Liu, Z. Y., and Zhang, Y. R. (2009). Hydrogen-induced cracking and healing behaviour of X70 steel. Journal of alloys and compounds, 484(1), 966-972.

[212] Pressouyre, G. M., and Bernstein, I. M. (1978). An electrical analog model of hydrogen trapping in iron alloys. Corrosion Science, 18(9), 819-833.

[213] Ren, X., Chu, W., Li, J., Su, Y., and Qiao, L. (2008). The effects of inclusions and second phase particles on hydrogen-induced blistering in iron. Materials Chemistry and Physics, 107(2), 231-235.